# Macroscopic Order of Helical Biomolecules and Crystal Phases Induced by Patterned Substrates and by Gravity

Inaugural–Dissertation
zur
Erlangung des Doktorgrades der
Mathematisch-Naturwissenschaftlichen Fakultät
der Heinrich-Heine-Universität Düsseldorf

vorgelegt von

HOLGER M. HARREIS

aus Siegen

Düsseldorf, 29. Oktober 2002

Gedruckt mit Genehmigung der
Mathematisch-Naturwissenschaftlichen Fakultät
der Heinrich-Heine-Universität Düsseldorf

| | |
|---|---|
| Referent: | Prof. Dr. H. Löwen |
| Koreferent: | HSDoz. C. N. Likos, PhD |
| | Prof. Dr. G. Gompper |

Tag der mündlichen Prüfung: im Dezember 2002

This thesis is based on the following original papers:

**Chapter 1:**

H. M. Harreis, A. A. Kornyshev C. N. Likos, H. Löwen and G. Sutmann
*Phase behavior of columnar DNA assemblies*,
Physical Review Letters **89**, 018303 (2002).

H. M. Harreis, C. N. Likos and H. Löwen
*Azimuthal frustration and bundling in columnar DNA aggregates*,
submitted to Biophysical Journal (2002).

**Chapter 2:**

H. M. Harreis, M. Schmidt and H. Löwen
*Decoration lattices of colloids adsorbed on stripe-patterned substrates*,
Physical Review E **65**, 041602 (2002).

**Chapter 3:**

J. Dzubiella, H. M. Harreis, C. N. Likos and H. Löwen
*Sedimentation profiles of systems with reentrant melting behavior*,
Physical Review E **64**, 011405 (2001).

**Chapter 4:**

H. M. Harreis, C. N. Likos and M. Ballauff
*Can dendrimers be viewed as compact colloids? A simulation study of the fluctuations of a dendrimer of fourth generation*,
to appear in the Journal of Chemical Physics (2002).

**Abstract**

In this thesis we present recent results obtained for four different soft condensed matter systems, each of which is discussed in a self-contained chapter. In the first chapter *columnar DNA assemblies* are investigated. The interaction between two stiff parallel DNA molecules is discussed using linear Debye-Hückel screening theory with and without including the dielectric jump at the DNA surface, taking into account the helical symmetry of DNA. The interaction depends on the interaxial separation of two DNA molecules, their azimuthal orientation, as well as on the amount and distribution of counterions adsorbed on the DNA surface. The optimal azimuthal angle is a function of the interaxial separation, which leads to azimuthal frustrations in an aggregate. On the basis of the pair potential, the positional and orientational order in columnar B-DNA assemblies in solution is investigated. Phase diagrams are calculated using lattice sums supplemented with the entropic contributions of the counterions in solution. A variety of positionally and azimuthally ordered phases and bundling transitions, strongly depending on the counterion adsorption patterns, is predicted. In the second chapter the equilibrium structure of *colloidal particles adsorbed on stripe-patterned substrates* is calculated as a function of the stripe width and separation as well as for different interparticle interactions. Due to a competition of length scales, a wealth of stable decoration lattices occurs such as triangular, quadratic, rhombic, kite-like and sheared honeycomb lattices, triangular slices as well as triangle superlattices. This is of relevance for constructing templates that enforce crystal growth of unusual solid structures. The third chapter is devoted to *sedimentation density profiles of star polymer solutions* as example of colloidal systems in sedimentation equilibrium which exhibit reentrant melting in their bulk phase diagram. Phase transitions between a fluid and a fluid with an intercalated solid are observed below a critical gravitational strength. Characteristics of the two fluid-solid interfaces in the density profiles occurring in Monte Carlo (MC) simulations are in agreement with scaling laws put forth in the framework of a phenomenological theory. Furthermore we detect density oscillations at the fluid-gas interface at high altitudes for high gravitational fields, which are verified with density functional theory and should be observable in surface scattering experiments. The fourth chapter presents work on the question whether *dendrimers* can *be viewed as compact colloids*. The specific system considered are *dendrimers of fourth generation* (G4). By employing monomer-resolved MC simulations, the conformations, density distributions, correlation functions and the form factor of G4 model dendrimers are analyzed. We find that these objects are hybrids between polymer chains and compact colloids, with the fluctuations of the monomers correlated at length scales of the order of the bond length but practically uncorrelated for lengths exceeding this scale. We discuss the implications of this finding on the possibility of regarding dendrimers as 'soft colloids', on the detection of these fluctuations in scattering experiments and on the inversion of intensity profiles obtained in small-angle neutron scattering (SANS) measurements.

**Zusammenfassung**

Die vorliegende Arbeit untersucht vier verschiedene Systeme aus dem Gebiet der weichen Materie, welche in eigenständigen Kapiteln vorgestellt werden. Das erste Kapitel beschäftigt sich mit *kolumnaren DNA Aggregaten*. Die Wechselwirkung zwischen zwei parallelen, steifen DNA Molekülen wird mithilfe der linearen Debye-Hückel Abschirmtheorie sowohl unter Berücksichtigung als auch unter Vernachlässigung des dielektrischen Sprunges an der DNA Oberfläche diskutiert. Die Wechselwirkung hängt vom Abstand, von der azimuthalen Orientierung der DNA Moleküle, als auch von der Anzahl und Verteilung der kondensierten Gegenionen ab. Der optimale azimuthale Winkel ist eine Funktion des interaxialen Abstandes der DNA Moleküle, was zu azimuthalen Frustrationen im DNA Aggregat führt. Auf der Basis des Potentials wird die Positions- und Orientierungsordnung der kolumnaren B-DNA Aggregate mithilfe von Gittersummen und den entropischen Beiträgen der in Lösung befindlichen Gegenionen untersucht. Die Theorie sagt eine Vielzahl an verschiedenen, geordneten Gitter- und Orientierungsphasen sowie stark von der Lokalisierung der adsorbierten Gegenionen abhängige Bündelübergänge der DNA voraus. Das zweite Kapitel untersucht die *Dekorationsgitter von Kolloiden auf in Streifen strukturierten Substraten* als Funktion der Streifenbreite und des Streifenabstandes, als auch für verschiedene Teilchenwechselwirkungen. Durch den Wettstreit verschiedener Längenskalen bilden sich verschiedene stabile Dekorationsgitter, wie Dreiecks-, Quadrat-, rhombische, Drachen-, verscherte Honigwabengitter, Dreieckstreifen- und Dreieck-Supergitter aus. Im dritten Kapitel werden *Sedimentationsdichteprofile von Sternpolymeren* als Repräsentant von Systemen mit wiedereintretendem Schmelzen im Bulk-Phasendiagramm behandelt. Unterhalb einer kritischen Gravitation tritt ein, zwischen zwei flüssigen Regionen befindlicher kristalliner Bereich auf. Eigenschaften der zwei flüssig-fest Grenzflächen in den Dichteprofilen der Monte-Carlo Simulationen sind in Übereinstimmung mit Skalengesetzen, die im Rahmen einer phänomenologischen Theorie berechnet wurden. Des weiteren treten im Falle starker Gravitation an der flüssig-gas Grenzfläche in großer Höhe Dichteoszillationen auf, welche mit Dichtefunktionaltheorie reproduzierbar sind und in Oberflächenstreu-Experimenten nachweisbar sein sollten. Im vierten Kapitel wird am Beispiel von *vierte Generation (G4) Dendrimeren* die Frage untersucht, ob Dendrimere als kompakte Kolloide betrachtet werden können. Vermittels Monomer-aufgelöster Monte-Carlo Simulationen werden die Konformationen, Dichterverteilungen, Korrelationsfunktionen und der Form-Faktor dieser G4 Modell-Dendrimere berechnet. Die Analyse zeigt, dass diese Moleküle Hybride zwischen Polymer-Ketten und kompakten Kolloiden darstellen, wobei die Monomer-Fluktuationen nur auf Längenskalen der Bindungslänge korreliert, für größere Abstände aber praktisch unkorreliert sind. Wir diskutieren die gewonnenen Erkenntnisse im Hinblick auf die Möglichkeit, Dendrimere als 'weiche' Kolloide zu betrachten als auch hinsichtlich der Inversion von Kleinwinkel-Neutronenstreungs Dichteprofilen.

# Table of Contents

# Introduction

The range of topics dealt with in this thesis is rather broad and, seemingly, no link relating the different issues discussed can be discerned. There are, however, embracing concepts crosslinking the four subject areas contained in the present work. The most obvious and most unspecific common feature is the fact that all systems pertain to equilibrium situations. It is always assumed that the systems at hand have had enough time to pass through a dynamical phase to be in a well equilibrated situation. A more specific, albeit still very general characteristic linking the four topics, is the fact that they all belong to the field of *soft condensed matter physics*. Soft condensed matter physics [1, 2, 3, 4] is a field of physics set in between the classic disciplines of condensed matter physics and the physics of the fluid state. By definition, according to the International Union of Pure and Applied Chemistry (IUPAC), soft matter systems consist of supramolecular entities, which, in at *least* one spatial dimension, fall in the range of 1 nm to 1 $\mu$m. These *mesoscopically* sized particles, termed *colloids*, are typically dispersed in a solvent whose constituents' size is found to be on the atomic dimension, so that in most cases it can be approximatively described as continuum. Often, a typical soft matter system's composition is complemented by further particle types with sizes in between the macroscopic and the mesoscopic scale, e.g., ions or smaller supramolecular aggregates. Soft matter systems are synonymously referred to as *colloidal suspensions*, *colloidal dispersions* or *complex fluids*, engendering emphasis on different aspects of the substance. Owing to the broad definition, a great number of different materials is included, stemming from different areas of research and application. In fact, linear polymers, micelles of surfactants, microemulsions, more elaborately architectured polymeric macromolecules such as dendrimers or star polymers, membranes, as well as biological macromolecules all belong to the family of soft matter systems. Correspondingly, soft matter is found in a vast range of technical, food technological, pharmaceutical and biological applications, including paint, ink, detergents, adhesives, drilling fluids, lubricants, self-assembling 'intelligent' novel materials, milk, mayonnaise, blood, urine, viruses, drug delivery into cells, trans-cell-membrane transport, protein crystallization and DNA recognition [5, 6]. A distinctive characteristic of soft matter materials as compared to their atomic or molecular counterparts is their strikingly low shear modulus. The shear modulus scales with the typical energy involved and the inverse volume of the elementary crystal unit cell, it thus turns out to be 9–12 orders lower in soft matter systems than in atomic or molecular crystals, hence the name *soft* matter. One of the features that has to a major degree stim-

ulated the interest in soft matter research is the fact that the interactions between colloidal particles can, in a wide range, be tailored according to the individual needs. While in an atomic or molecular condensed matter system the interactions are essentially dictated by the electronic structure, the interaction potential between colloidal particles can be almost chosen at will, ranging from short ranged attractions to long ranged repulsions. Generally speaking, external perturbations typically show effects on length and time scales of the particle structures. Since the length scales in soft matter are found in the mesoscopic regime, real-space analysis of physical phenomena becomes a viable tool, building a direct bridge between computer simulations and experiment. This is another strong support for research in soft matter physics, allowing for a very direct check of physical models. Furthermore insights gained for soft matter systems can often be directly transferred to 'hard' condensed matter. Additionally, many phenomena occurring in soft matter are *independent* of the molecular details and therefore offer universal understanding of physical problems. Soft matter systems are thus predetermined to be an ideal model system for experimentalists and theorists alike. Nonetheless, as we already noted above, one never has to go far to be back in the real world: the systems investigated in this thesis have direct relevance in the biotechnological industry, such as DNA for gene therapy purposes and dendrimers as carriers for drug delivery, as well as in nanotechnological applications, as applies to the colloidal adsorption on patterned substrates, which is relevant for developing photonic crystals and can also be of importance for the assembly of other devices on the nanoscale.

The intriguing challenge in soft matter physics is to understand and/or predict the macroscopic behavior from the microscopic interactions. Since a colloidal dispersion is separated by some orders of magnitude in length scales from the microscopic level, it is a non-feasible task with present methods and devices to carry out such a calculation building on 'ab initio' methods. In order to assess, e.g., the phase behavior of a given soft matter system with mesoscopic constituents as a function of the densities of the species involved, one therefore has to come up with methods which help to bridge the length scale gap from the microscopic interactions to the macroscopic phase behavior. The most convenient approach is to build two bridges: first to step over from the microscopic realm to the mesoscopic regime and then to employ a second step to reach the macroscopic world. A very powerful concept for building the first bridge is the concept of the *effective interaction* [7] between the mesoscopic constituents. It is derived by integrating out the microscopic degrees of freedom and yields an interaction working on the level of the mesoscopically sized particles only, yet incorporating the effects due to the presence of the microscopic constituents. The effective interaction being known, statistical mechanical methods can be applied to determine the collective behavior of the assembly of the mesoscopic particles, thus attaining the macroscopic scale.

In this thesis different foci lie on the investigation of the different systems. They can be grouped according to two aspects: the first being the study of *macroscopic* behavior, the second being the study of phenomena on the *mesoscopic* scale. The systems presented in

chapter 1 (columnar DNA assemblies), chapter 2 (colloids on stripe-patterned substrates) and chapter 3 (star polymers under gravitation) fall into the first category. In the case of DNA, we take advantage of the two length-scale bridges, first calculating the pair interaction between two DNA molecules in order to then explore the resulting macroscopic behavior of a DNA assembly. The effective interaction could be calculated by assuming linear screening by the counterions, which eliminates the microscopic degrees of freedom and by knowing the *internal* structure of the mesoscopic constituents, the DNA molecules, from experimental structural data. As for the colloidal adsorption on patterned substrates, the internal structure of the colloids is the simplest possible: they are modeled as hard spheres. This allows for stepping in at the mesoscopic level and for bridging over to the collective phenomena of the many particle problem. The star polymers are treated in the same way: for our purposes here, we start at the mesoscopic description only. This, however, is only possible, since we can take advantage of previous work [8, 9] having elucidated the structure of one isolated star polymer and having established the effective star polymer interactions by integrating out the microscopic degrees of freedom. This level of knowledge has not yet been attained for dendrimers, which gives the reason for the second category to be represented by the dendrimer study of chapter 4. There, we stop rather than start at the mesoscopic level: the interest is on the structural properties of one such molecule and its distinctive features alone (One may however note that this is nothing but investigating the collective behavior of the monomers as statistical ensemble). As we discuss in the outlook in Chapter 5, the final goal remains to build the second path bridging over to the effective interaction of two dendrimers to eventually be able to calculate dendrimer phase diagrams.

For the first category, in which we investigate the macroscopic behavior of the soft matter systems, a further point of view under which these substances can be considered is which mechanism is responsible for inducing the *macroscopic order* evidenced in all these systems. For the DNA, the answer lies in the internal structure: Due to the helical symmetry of the DNA phosphate backbone, a particular macroscopic order is yielded. As for the colloids on stripe-patterned substrates as well as the star polymers, the driving force for macroscopic ordering is rather an external potential which is applied. In the case of the colloids on the patterned substrate, this external potential is the patterned substrate itself: It imposes packing and energetical constraints to which the system has to react. The star polymers are exposed to the influence of the external gravitational potential, inducing a density gradient, which, in turn, gives rise to crystalline order in some parts of the star polymer solution.

Moreover, in addition to the different questions pursued in the investigations of the various problems, the soft matter systems in this thesis appear in quite different realizations: the DNA treated in chapter 1 is a polyelectrolyte (PE) molecule, a complex helical polymeric molecule with charged monomers as building blocks. In chapter 2 we consider 'hard' colloids, modeled as hard spheres (HS), which are experimentally realized as, e.g. polystyrene, poly (methylmethacrylate) (PMMA) or silica spheres. The spherical shape of the particles very much simplifies their study since they exhibit the highest degree of symmetry possi-

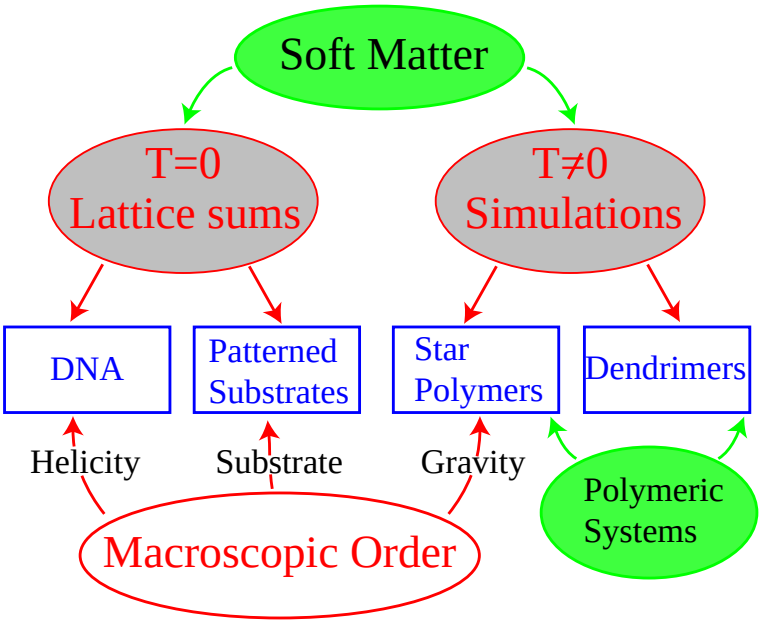


**Figure 1:** Schematic illustration of the systems under consideration in the present thesis, together with methods employed and mechanisms inducing macroscopic order.

ble, implying that the interparticle interactions solely depend on the interparticle distance. Chapters 3 and 4 deal with an intermediate case in which the molecules, star polymers or dendrimers, respectively, do not display spherical symmetry in each instantaneous configuration, yet, on average can be described as spherically symmetric entities. In both cases, the supermolecular aggregates (dendrimers and star polymers) are polymerized from a high number of monomers, which, in our modeling are described by Lennard-Jones (LJ) particles (in the case of the star polymers, however, this level is not included in the present work, since, as noted above, we hereby rely on previous calculations).

A further system of classification on a more specific level is provided by discriminating the investigations according to the methods employed. The first class to mention are ground state calculations for the DNA assemblies as well as for the colloidal adsorption on stripe-patterned substrates. In both cases thermal fluctuations are neglected since the interaction energies govern the game, rendering the neglect of the thermal energies a sensible approximation, thereby guaranteeing that $T = 0$ lattice sum calculations provide the representative thermodynamic state. The second class is comprised of the dendrimer and the star polymers study. Here, Monte Carlo simulations (MC) are employed to sample the configuration space of the ensemble, which in principle provide an exact solution to the statistical physics problem [10, 11].

The above considerations concerning the interrelation of the topics contained in the present thesis are schematically summarized in Fig. 1.

The outline of the thesis is as follows. In chapter 1 we report on phase behavior of columnar DNA assemblies. Chapter 2 is devoted to the adsorption structures colloids form on stripe-patterned substrates. In the following two chapters, Monte Carlo simulations are applied to the density profiles of star polymers exposed to a gravitational field (chapter 3) and to the equilibrium properties of an isolated dendrimer (chapter 4). Each chapter of the thesis is self-contained, preceded by a short introduction to the problem dealt with and ended by a conclusion. Chapter 5 gives a brief summary of the main accomplishments and discusses possible extensions of this work for future attention.

# Chapter 1

# Phase Behavior of Columnar DNA Assemblies

*Relatively short fragments of deoxyribonucleic acid (DNA), with lengths ranging from one to about* 100 *persistence lengths* $L_p$*, where* $L_p = 500\,\text{Å}$*, form columnar assemblies in salt solution, with all DNA molecules aligned in parallel. DNA being a* helical *molecule, two degrees of freedom govern the behavior of such assemblies: The torsional as well as the translational degree of freedom. The aim of this chapter is first to elucidate the pair interaction present between DNA molecules in the state of parallel alignment. The second aim is to predict the translational and orientational structures that appear in a columnar assembly as a function of the relevant parameters. These are the DNA packing fraction, the salt concentration in the aggregate as well as the sort and amount of counterions present in the solution.*

## 1.1 Introduction

Many biological systems contain densely packed DNA assemblies, as, for example viral phage heads and sperm. For the proper functioning of these biological systems, including humans, it is of extreme importance that the mechanisms carrying out the packaging of DNA in the cell work in a robust manner, since, for example, it is believed that DNA packing in chromatin plays an important role in gene regulation [12]. In light of the rapidly growing field of gene therapy it is of great interest to understand the mechanisms actually responsible in living organisms for condensing DNA into densely packaged assemblies. The first step to this end is a model of DNA which is able to capture its most significant characteristics, with the second step consisting of devising a theory for DNA assemblies. In the last few years, many efforts have been made on the theoretical side to understand the interaction of two DNA molecules and DNA condensation [13, 14, 15, 16, 17, 18, 19, 20, 21]. The matter is complicated by the fact that due to its chemical structure DNA is a helical molecule, rendering solutions for the DNA-DNA interaction considerably complicated. Moreover, the overall electroneutrality condition dictates that counterions be present in the solution, and

the latter screen the electrostatic repulsion between the DNA-rods. Only far from their axes can DNA molecules be apprehended as uniformly charged cylinders: this is the simplest approximation possible in an investigation of the DNA-DNA interaction and one that neglects the helical symmetry completely, see, e.g., [13, 22, 23, 24, 25, 26, 27, 28, 29, 30] and references therein. It has to be expected that such an approximation works well for distances much larger than the scale of the helical symmetry of the DNA molecule, $R \gg H$, where $H \approx 3.4$ nm is the DNA pitch length. This approach amounts to calculating the interaction of two homogeneously charged cylinders, whereby the continuously smeared charges along the cylinders create an electrostatic repulsion of two DNA molecules (exponentially screened by the electrolyte). Indeed, predictions for force-distance curves on the grounds of a traditional Derjaguin-Landau-Verwey-Overbeek (DLVO) theory for homogeneously charged cylinders turned out to be accurate for separations larger than several nanometers, while significant deviations in the biologically more relevant range of smaller separations [14] emerged. It can be concluded that apart from investigations where only the far-field behavior is of importance, it is crucial to consider the helical symmetry of DNA molecules, since the interaction potential in the relevant regime of intermediate distances is dramatically changed by the presence of a highly inhomogeneous charge distribution. An additional effect is provided by the fact that DNA is a polyelectrolyte molecule: in an aqueous solution, its cations dissolve into the solution, leaving behind a negatively charged DNA phosphate backbone. A major fraction of the cations condenses in the Bjerrum layer [29] around the molecular surface. With cations specifically adsorbing onto the DNA surface present in the solution, however, the scenario changes: the DNA molecules can be fully neutralized [31, 32, 33] or even overcharged [34]. The interaction potential is thus additionally influenced by the amount and type of counterions present in the solution.

In order to condense DNA in an aggregate, either osmotic stress [35] or counterions specifically adsorbing on DNA have to be applied as condensing agents [5]. The latter can be, e.g., salts with $Mn^{2+}$, $Cd^{2+}$, spermidin, protamine or cobalt hexammine [5] cations, which are known to preferentially adsorb in the DNA grooves [36, 37, 38, 39]. The sensitivity to the type of counterion for DNA aggregation [5] is manifest in the fact that other counterions, such as, e.g., $Ca^{2+}$ or $Mg^{2+}$, which are known to exhibit a high affinity to phosphates and thus predominantly adsorb on the strands, do not induce DNA aggregation. A model should thus incorporate/reproduce these subtle effects and be able to explain the mesomorphism [40] of DNA aggregates stemming from the presence of different types of counterions.

Once the interaction of DNA molecules is derived by means of some theory, one can turn to the next step and calculate the properties of DNA assemblies. The structural organization and properties of such condensates *in vivo* are largely unknown but has been, in the last several years, under investigation in *in vitro* experiments, [41, 42, 43, 44, 45, 46, 47, 48]. Simple model systems able to predict the spatial as well as the orientational structure of these condensates are highly desirable for a better elucidation of the mechanisms occurring *in vivo*. Previous work has shown [49] that it is a reasonable approximation/simplification to

focus on columnar assemblies, neglecting possible tilting effects, as we will explain later. Most of the work relied on approximating DNA as homogeneously charged rods [13, 15, 16, 17, 19]. Only when taking into account, however, the helicity of DNA molecules, a relevant feature for the properties of such a columnar DNA assembly emerges: a non-trivial interplay between the torsional and translational degrees of freedom.

A mean-field calculation of this problem was presented in [50], while the full statistical mechanical problem of columnar DNA assemblies was recently solved in [51] using a pair potential for the DNA-DNA interaction devised in [14]. The motivation for the present chapter is two-fold: First, we give more details and background for the calculations already published in [51]. In this work, it was found that the dependence of the optimal azimuthal orientation angle of two DNA molecules on their interaxial separation gives rise to azimuthal frustrations in an aggregate, thereby inducing phase transitions between different ordered orientational structures. Furthermore, depending on the type and amount of counterions condensed on the DNA surface, strong attractions were found, resulting in DNA bundling transitions. More importantly, the second motivation for the present work is to discuss the effect of discretized charges along the DNA strands and the effect of the dielectric jump at the DNA surface on the phase behavior. We find that although the phase boundaries shift quantitatively, especially at high densities, the global topology of the phase diagrams remains unaffected. This gives evidence for the fact that the topology of the phase diagram itself is generic, i.e. will be stable also with respect to further changes in the interaction, including, e.g., hydration forces that are sometimes modeled through a distance-dependent dielectric constant $\epsilon(\vec{r})$ [52].

The rest of the chapter is organized as follows: In Sec. 4.3.1 we present the way DNA molecules are modeled in the present work. Sec. 1.3 is devoted to a discussion of the pair interaction potential of DNA molecules and its dependence on different approximations, i.e., continuous line charge distributions or neglect of the dielectric jump. In Sec. 4.2 the theory for columnar DNA assemblies is explained and used to calculate the phase diagrams. We summarize and conclude in Sec. 4.5.

## 1.2 The Model

DNA is a helical bio-molecule with two charged phosphate strands helically winding around a core region consisting of nucleotide base-pairs. The two strands are not symmetrically distributed around the molecules core region, but rather are separated by an azimuthal angle of $2\tilde{\phi}_s \approx 0.8\,\pi$, see Fig. 1.1 for an illustration. Under physiological conditions, DNA is present in the B-DNA conformation, a right-handed helical molecule [53]. In B-DNA, there are $N = 10$ nucleotides per helical turn with a helical pitch length of $H \approx 34$ Å. Each nucleotide contains a negatively charged phosphate group, giving rise to a total charge of $q = -10\,e$ per helical pitch, which translates into a surface charge density of $\sigma = 16.8\,\mu\mathrm{C/cm}^2$. To model the interaction, we envision the molecules as long, rigid cylinders with a hard-core radius

of $a = 9\,\text{Å}$. Strictly speaking, this approximation is only appropriate for DNA fragments of contour lengths up to the persistence length $L_p$, which is typically found to be $500\text{Å} - 1000\text{Å}$ (depending on the ionic strength) [54]. Samples of parallel packed arrays have however been prepared for contour lengths of up to 100 $L_p$ [35, 55]. In our model the phosphate backbone is accounted for by continuous helical line charges located on the surface of the DNA hardcore cylinder. We also calculated pair interactions for discrete charge patterns on the DNA surface, as we will discuss in detail later. Each DNA duplex furthermore carries a compensating positive charge stemming from the adsorbed counterions, which are modeled in the same way as the phosphate backbone as continuous line charges. The degree of charge compensation will be referred to as $0 < \theta < 1$, while the fractions of condensed counterions in the minor and major grooves, and on the two strands, are accounted for by $f_1$, $f_2$, and $f_3$ respectively, where $f_1 + f_2 + f_3 = 1$ holds. The non-adsorbed, mobile counterions in solution screen the Coulomb interactions between the helices, causing at large separations an exponential decay of the latter with the Debye screening length $\kappa^{-1}$.

In our model, we study formally the two extreme cases of dielectric constants $\epsilon_1$ and $\epsilon$ in the DNA core and in the solvent, respectively. The first case is that we assume no dielectric jump at all, $\epsilon/\epsilon_1 = 1$, while the other limit is $\epsilon/\epsilon_1 = \infty$. In the first case, it is more convenient to formulate the interaction in terms of a Yukawa-segment model, while the second case has been elaborated in a practical form by Kornyshev and Leikin [18]. The motivation to study different $\epsilon/\epsilon_1$ is to check effects of the discontinuity formally. In reality one would expect $\epsilon/\epsilon_1 \approx \infty$ since the dielectric constant of bulk water is very high. Close to the DNA surfaces, however, it is not at all clear whether the effect of a dielectric discontinuity as described by macroscopic electrostatics is justified. More realistic dielectric effects were taken into account by a space-dependent dielectric constant $\epsilon(\vec{r})$ [56]. One could surmise that if the resulting interaction and phase behavior is similar for the two limiting cases $\epsilon/\epsilon_1 = 1$ and $\epsilon/\epsilon_1 = \infty$ actually dielectric effects on this molecular scale are not very important at all. This in turn gives evidence for at least qualitative stability of our results under application of more realistic interactions stemming from more refined molecular calculations.

The main characteristics of the model DNA molecules are illustrated in Fig. 1.1. For clarity, possible condensed counterion strands have been omitted in the illustration. The azimuthal orientation of molecule $i$ is referred to by its azimuthal angle $\phi_i$, which is defined in the following way. A plane (gray-shaded in Fig. 1.1) perpendicular to the parallel axes of the two DNA molecules hits the dark colored $5' - 3'$ strand [57] of each molecule at the point indicated by the vector originating from molecule's $i$ axis, which we may formally call 'spin'. The angle $\phi_i$ formed by this vector and some arbitrary reference direction on the plane, taken, for clarity to be the vector connecting the two molecules' axes is the azimuthal orientation angle of molecule $i$. We assume that the DNA molecules are parallel, as depicted in Fig. 1.1, which is justified by reasons given in Sec. 4.2. If we furthermore assume the molecules to be infinitely long and their charge distributions to be described by helical line charges as illustrated in Fig. 1.1, their mutual state can be described by two parameters:

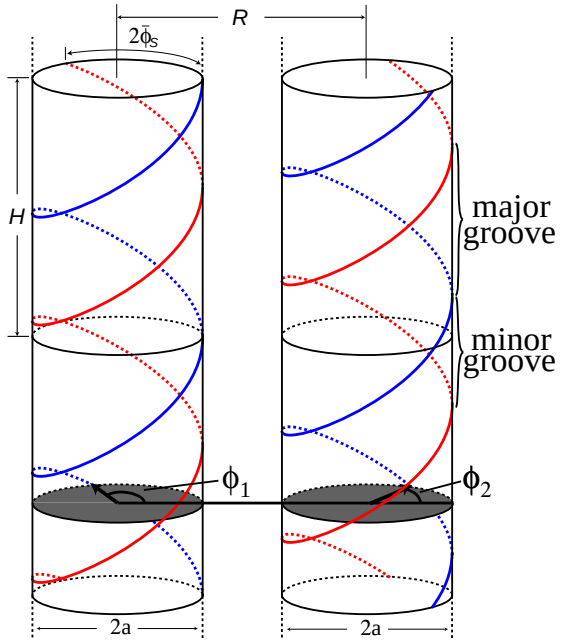


**Figure 1.1:** Illustration of two model DNA molecules at an interaxial separation $R$. The molecules are assumed to be rigid, long cylinders of radius $a$ with a helical pitch length of $H \approx 34$ Å. In between the two DNA helices a major and a minor groove are formed, due to the asymmetry in the azimuthal angle between the two helices, $2\phi_s \approx 0.8$. See text and Fig. 1.2 for an explanation of the angles $\phi_1$ and $\phi_2$.

their interaxial separation $R$ as well as their mutual azimuthal orientation, $\phi = \phi_1 - \phi_2$. The problem thus reduces to an effective two dimensional problem of 'XY-spins' interacting via a potential $U(R, \phi)$. We further illustrate this point in Fig. 1.2, which depicts the gray-shaded plane included in Fig. 1.1 in more detail. It has to be noted that the problem may only be viewed as effectively spatially two-dimensional under the assumption of continuous line charges. For discrete charge patterns, the orientations $\phi_1$ and $\phi_2$ both enter the pair potential. Let us assume discrete charges to illustrate the validity of this statement. The two molecules shall be separated by a vector $\mathbf{R}$, as shown in Fig. 1.2, with molecule 1 at an angle $\phi_1$ and molecule 2 at an angle $\phi_2$ relative to $\mathbf{R}$ in a given plane $P$ that perpendicularly cuts the molecular axes. The points where the $5' - 3'$ strands of molecules 1 and 2 hit the plane $P$ shall be denoted by $\mathbf{p}_1$ and $\mathbf{p}_2$, respectively. Both in $\mathbf{p}_1$ and $\mathbf{p}_2$ discrete charges are located as is the case in Fig. 1.2. Were the interaction only to depend on the mutual azimuthal orientation, $\phi = \phi_1 - \phi_2$, a configuration with both molecules turned by $\Delta\phi$ should yield the same interaction. Obviously, after turning both molecules the $5' - 3'$ strands will hit $P$ in new locations $\mathbf{p}_1^n$ and $\mathbf{p}_2^n$. This means altered charge distances in the contribution of plane $P$ to the total DNA-DNA interaction. Since the total interaction is the sum of the contributions of all charges (planes), the interaction might still be conserved if another plane along the molecule contributed the same value after the rotation as $P$ did before the rotation

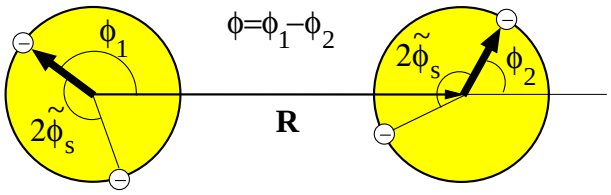


**Figure 1.2:** A plane perpendicular to the parallel axes of two DNA molecules separated by vector **R** hits the DNA strands denoted by the white circles with a minus inside; $2\tilde{\phi}_s$ is the azimuthal width of the minor groove. The vectors joining the axes with the points where the $5' - 3'$ strand [57] hits the plane may be formally called 'spins'. The angle $\phi$ between the two 'spins' characterizes mutual azimuthal orientation of the molecules.

and vice versa. The only plane capable to switch configuration with $P$ through a rotation by $\Delta\phi$ is a plane $P'$ shifted by $\Delta z = H\ \Delta\phi/2\pi$ relative to $P$ along the molecular axes. The $5' - 3'$ strands will then cut through $P'$ in $\mathbf{p}'_1 = \mathbf{p}_1$ and $\mathbf{p}'_2 = \mathbf{p}_2$. With a discrete charge pattern, however, charges will only be located in $\mathbf{p}'_1$ and $\mathbf{p}'_2$ if $\Delta z$ is commensurate with the rise of the charge pattern along the molecular axes, or in other words, if $\Delta\phi = n\ 2\pi/N$ holds, with $n \in \mathbb{N}$ and $N$ the number of DNA charges per helical pitch and strand. If on the other hand, continuous line charges are used, the original plane $P$ and $P'$ are equivalent without any further condition and contribute the same amount to the interaction. The only requirement to be met is that the molecules be at least one helical pitch long, so that the existence of $P'$ is guaranteed. The mutual azimuthal angle $\phi$ can, for continuous line charges under the additional condition of infinitely long molecules, equivalently be thought of as a relative vertical shift $z = H\phi/2\pi$ of the two molecules. We will come back to a more detailed discussion on discrete charge patterns versus continuous line charges at a later point in Sec. 1.3.

## 1.3 The Pair Potential

As already sketched in the Introduction of Sec. 4.1, the pair potential will be considered under different assumptions concerning dielectric jump and charge distributions. The approach is, on a general level, based on the linear screening theory picture, yielding a Yukawa like, screened Coulomb interaction for any pair of charges on the two molecules [58, 59, 60]. We will first resort to considering the case of no dielectric jump and refer to this situation as the *Yukawa-Segment-Model* potential. The Yukawa-Segment idea has been tested against micro-ion resolved simulations in [61, 62] and has been used for calculating dynamical correlations in Tobacco-Mosaic Virus suspensions and phase diagram calculations of the latter in [63] and [64] respectively. Here, the Yukawa-segment approach furthermore allows for testing the influence of a discrete charge pattern as opposed to continuous line charges. The

second case includes the dielectric jump at the DNA surface, yet necessitates continuous line charges. We will refer to it in the following as *Kornyshev-Leikin* Potential.

### 1.3.1 Yukawa-Segment-Model Potential

The canonical starting point for the Yukawa-segment-model is to exactly mimic the discrete number of charges present in real DNA molecules. The second generic case, opposed to the former, is to assume the charge distributions to be continuous line charges. Although the first approach might, at first sight, seem superior to the latter, it has to be kept in mind that the 'real' charge distribution will definitely be not point like, but rather smeared on the whole phosphate group, two of which are closely neighbored, so that a modulated continuous line charge distribution should be the most realistic way of modeling the DNA charge distribution. Such an approach, however, requires an input from quantum chemical calculations and is therefore beyond the scope of the present study. We will now first illustrate the general approach to the calculation of the pair potential and then come back to a discussion of the differences between the discrete and the continuous charge distribution version.

We assume linear screening to act between any two charge elements $q_i$ and $q_j$ on the continuous helical line charges of the DNA molecules, yielding a Yukawa interaction [58, 59, 60],

$$V(r) = \frac{q_i q_j}{\epsilon r} \exp(-\kappa r). \tag{1.1}$$

Here, $\kappa = \lambda_D^{-1}$ is the inverse Debye screening length and $\epsilon = 81$ is the dielectric constant of the solvent (water). In order to access the total pair interaction of two DNA molecules, we have to integrate along each pair of interacting helical line charges (strands) (or sum in the case of discrete charge patterns).

Let molecule 1 be at the origin of the coordinate system and molecule 2 at $\mathbf{R} = R\ \mathbf{x}$, see Fig. 1.2. In its most general form, a helix, parametrized by its helical angle $\varphi$, furthermore depends on a set $\{\mathcal{P}\}$ of additional parameters. This set of parameters $\{\mathcal{P}\} = (a, \lambda, (r_x, r_y), \Delta\varphi)$ consists of the helix radius $a$, the helical rise $\lambda = H/2\pi$, the position $(r_x, r_y)$ of the helix axis in the $x-y$-plane and the angular offset $\Delta\varphi$ of the helix, indicating where the helix starts to rise from the $x-y$-plane. Making use of the special conditions present in our case, namely that we only consider molecules residing on the $x$-axis and that all helices exhibit the same radius as well as the same helical rise, $\{\mathcal{P}\}$ can be reduced to only consist of $r_x$ and $\Delta\varphi$, $\{\mathcal{P}\} = (r_x, \Delta\varphi)$. The corresponding helix parametrization for one single helix reads as

$$\mathbf{H}(\varphi; \{\mathcal{P}\}) = (2a\cos\varphi - r_x, 2a\sin\varphi, \lambda(\varphi - \Delta\varphi)). \tag{1.2}$$

The angular offset $\Delta\varphi$ is set to $\phi_1$ for the 'first' strand on the first molecule. Thereby the angular offsets of all other strands involved are uniquely determined by the DNA geometry, e.g., the second DNA phosphate strand on molecule 1 has $\Delta\varphi = 2\tilde{\phi}_s + \phi_1$, the counterion

strand in the minor groove is characterized by $\Delta\varphi = \tilde{\phi}_\mathrm{s} + \phi_1$ and the counterion strand in the major groove has $\Delta\varphi = \pi - \tilde{\phi}_\mathrm{s} + \phi_1$ as angular offset. The charge strands on molecule 2 follow the same logic, except that their respective offsets have a term of $\phi_2$ instead of $\phi_1$, since the rotation of molecule 2 has to be accounted for, see again Fig. 1.2 for an illustration. The interaction between one strand on molecule 1 and another strand on molecule 2 is given by

$$\begin{aligned} U_{1,2}(R,\phi) = \int d^3r\ d^3r'\ d\varphi_1 d\varphi_2\ V\big(|\mathbf{r}-\mathbf{r}'|\big) \\ \delta\big(\mathbf{r} - \mathbf{H}(\varphi_1;\{\mathcal{P}\}_1)\big)\delta\big(\mathbf{r}' - \mathbf{H}(\varphi_2;\{\mathcal{P}\}_2)\big), \end{aligned} \tag{1.3}$$

which is a diverging quantity, since the integral in Eq. (1.3) includes the two infinitely long strands. What we are interested in for our purpose is the interaction that segments of a given length $L$ experience. As the Yukawa type interaction between all charge segments decays exponentially and since, due to the periodicity, all helical pitches are the same, we may to this end, proceed in the following way. On molecule 1 one pitch length $H$ serves as integration interval, whereas on molecule 2 we integrate from $-\infty$ to $\infty$. Practically, due to the exponential decay in the potential, convergence of the integral is obtained after a maximum of 10 pitch lengths $H$ has been integrated. The result is the interaction energy of one pitch on strand 1 with the total length of molecule 2. Multiplication of this quantity with the number of pitches $L/H$ to be taken into account for a length $L$ yields the interaction of a segment of length $L$ on strand 1 with a segment of length $L$ on strand 2, whereby endpoint effects are ignored via the integration from $-\infty$ to $\infty$.

The total interaction of a segment of length $L$ on molecule 1 with one on molecule 2 then is the sum over the interactions of all strands on molecule 1 with all strands on molecule 2, including the DNA phosphate strands as well as the condensed counterion strands:

$$U(R,\phi) = \sum_{i\neq j} U_{i,j}(R,\phi), \tag{1.4}$$

where the symbolic notation above implicitly assumes $i$ to be taken from the set of all strands on molecule 1 and $j$ correspondingly from molecule 2. Inserting the Yukawa-segment interaction, Eq. (1.1) in Eq. 1.4 and carrying out the $r$ and $r'$ integrations in Eq. (1.3), together with the above consideration on the integration intervals, yields the expression

$$\begin{aligned} U(R,\phi) = \frac{L}{H}\sum_{i\neq j}\int_0^{2\pi}\int_{-\infty}^{\infty} d\varphi_1 d\varphi_2 \\ \frac{f_i f_j (\theta N e)^2}{\epsilon\big|\mathbf{H}(\varphi_1;\{\mathcal{P}\}_i) - \mathbf{H}(\varphi_2;\{\mathcal{P}\}_j)\big|} \\ \exp\Big(-\kappa\big|\mathbf{H}(\varphi_1;\{\mathcal{P}\}_i) - \mathbf{H}(\varphi_2;\{\mathcal{P}\}_j)\big|\Big). \end{aligned} \tag{1.5}$$

Here and in Eq. (1.4), the index $i$ is taken from the set $i \in \{s_1^{(1)}, s_2^{(1)}, c_1^{(1)}, c_2^{(1)}\}$ and $j$ covers $j \in \{s_1^{(2)}, s_2^{(2)}, c_1^{(2)}, c_2^{(2)}\}$, while $\{\mathcal{P}\}_i$ shows the dependence of the given strand on the specific

geometrical parameters determining its parametrization. By $s_k^{(l)}$ the $k$-th phosphate strand on the $l$-th molecule is denoted, while $c_k^{(l)}$ describes the corresponding counterion strand. In $s_k^{(l)}$ the counterion strands which are condensed *on* the phosphate strands are included, since they only trivially renormalize the charge carried by the phosphate strands. This enters into the charge fraction parameters $f_i$ and $f_j$ in the following way:

$$f_{s_1,s_2}^{(1),(2)} = (1 - f_3) \tag{1.6}$$

$$f_{c_1}^{(1),(2)} = f_1 \tag{1.7}$$

$$f_{c_2}^{(1),(2)} = f_2, \tag{1.8}$$

where $f_1$, $f_2$, and $f_3$ are the fractions of counterions condensed in the minor and major grooves, and on the two strands, respectively, satisfying $f_1 + f_2 + f_3 = 1$.

The differences of a discrete charge potential to a continuous line charge potential can be estimated by tuning the number of charges per pitch length, $N$. As we discussed in Sec. 4.3.1, for discrete charges the interaction does depend on both molecules' orientations $\phi_1$ and $\phi_2$ and not only on the difference $\phi = \phi_1 - \phi_2$ as it is the case for continuous line charge distributions. For discrete charge patterns, this opens up two different routes: The first and simpler is to set $\phi_1 = 0$ and look at $U(R, \phi_1 = 0, \phi_2)$, while the second and more refined one is to vary $\phi_1$ and $\phi_2$ to then consider $U(R, \phi)$ at $\phi = \phi_1' - \phi_2'$, where $\phi_1'$ and $\phi_2'$ have been obtained as energetically optimal combination for a given *mutual* azimuthal orientation $\phi$ of the two DNA molecules.

The first approach is taken in Fig. 1.3, where the pair interaction per persistence length $L_p$, $U(R, \phi_1 = 0, \phi_2)$, is displayed as a function of the azimuthal orientation angle $\phi_2$ with $\phi_1 = 0$ fixed, at two fixed interaxial separations, $R = 2.1$ nm and $R = 2.5$ nm, for $N = 10$ and $N = 20$ charges, as well as for a continuous line charge. The counterion condensation parameters are $f_1 = 0.3$, $f_2 = 0.7$ and $f_3 = 0$. It can be seen that already for $N = 20$ the obtained potential curve is indistinguishable from that for the continuous line charge potential at both interaxial separations. For $N = 10$ charges on the other hand, deviations exist predominantly for $R = 2.1$ nm, but have decreased to a minuscule level for $R = 2.5$ nm. A more detailed structure of the pair potential as a function of the azimuthal orientation is apparent for the smaller separation. The differences mainly pertain to the region around the maximum and the two minima. The position of the global minimum, however, the most important parameter for the behavior in an assembly, is practically unchanged. This assertion is only based on the observation of the potential at two fixed interaxial separations. Its main point however is sustained by the data shown in the inset of Fig. 1.4, where we show the optimal azimuthal orientation angle $\phi_{2,\mathrm{opt}}$, again at $f_1 = 0$ fixed, as a function of the DNA-DNA interaxial separation $R$. The corresponding potential is shown in the main graph of Fig. 1.4. The detailed behavior of the optimal azimuthal alignment angle is different for $N = 10$ charges from that for $N = 20$ charges and continuous line charges, whereas the latter are indistinguishable from one another. The key points for the behavior in an aggregate, however, remain unchanged for all cases: First the optimal angle is nonzero

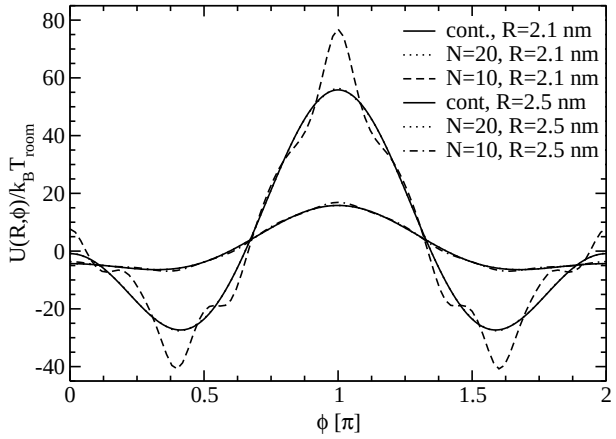


**Figure 1.3:** Yukawa-segment pair potential per length $L_p$ as a function of the azimuthal orientation angle $\phi_2$ with $\phi_1 = 0$ fixed, at interaxial separations $R = 2.1$ nm and $R = 2.5$ nm, for $\theta = 0.9$ and $f_1 = 0.3$, $f_2 = 0.7$, $f_3 = 0$. At both interaxial separations the potential is displayed for $N = 10$, $N = 20$ charges as well as for continuous line charges.

for all interaxial separations smaller than $R_* \approx 30$Å and second for very small intersurface separations the optimal angle is approximately $0.42\ \pi$.

The second approach to discrete charge patterns is to calculate the interaction for all combinations of $\phi_1$ and $\phi_2$ and then to minimize the obtained potential energy on curves of constant $\phi = \phi_1 - \phi_2$. This is the more realistic version of the approach shown above, yet it is still an approximation for an aggregate since there optimized combinations of $\phi_1$ and $\phi_2$ for a given $\phi$ will not be possible with respect to all neighbors of a given DNA molecule. In Fig. 1.5 we compare this approach for $N = 10$ discrete charges at an interaxial separation $R = 2.1$ nm with the one presented above and with the continuous line charge version. We again have $\theta = 0.9$, $f_1 = 0.3$, $f_2 = 0.7$ and $f_3 = 0$ for the counterion condensation parameters. The resulting potential curve is the lowest in energy as one should expect from the procedure applied. The structure is close to the one induced by continuous line charge distributions and the minima are found at exactly the same loci as when keeping $\phi_1$ fixed at $\phi_1 = 0$, they are thus practically at the same positions as for the continuous line charge version. Again, from the analysis of one single interaxial separation we thus conjecture that the overall behavior of the pair potential will not present significant deviations from the reference continuous charge case. This statement is confirmed by analyzing the inset of Fig. 1.6, where we show the optimal azimuthal angles as a function of the interaxial separation $R$ for the three different approaches to the charge distributions. Again, the dependence of the optimal azimuthal angle on the interaxial distance is very similar for the three cases studied, which will induce similar angular frustration behavior in an assembly. In detail, the optimal angle curve is closer to the one for a continuous charge distribution in the case

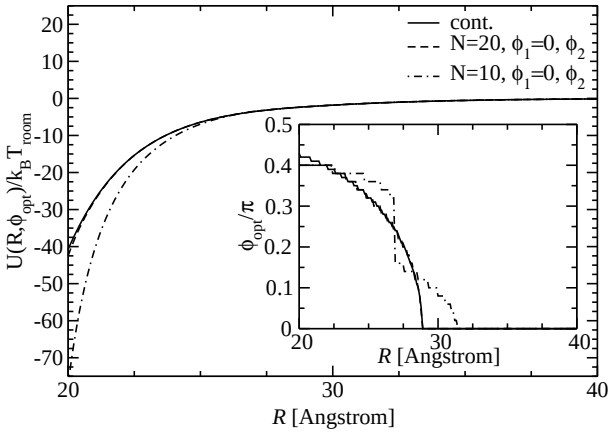


**Figure 1.4:** Yukawa-segment pair potential per length $L_p$ as a function of the interaxial separation $R$ of two DNA molecules, at the optimal angle $\phi_{2,\mathrm{opt}}(R)$, depicted for $N = 10$, $N = 20$ charges as well as for continuous line charges. The dependence of the optimal angle on the interaxial separation $R$ is shown in the inset.

where both angles $\phi_1$ and $\phi_2$ are free to rotate and the energetically optimal combination yielding the desired mutual azimuthal orientation $\phi = \ f_1 - \phi_2$ is chosen, as compared to the case where $\phi_1$ is set to zero. As far as the behavior of the pair interaction at optimal azimuthal angle, shown in the main graph of Fig. 1.6, is concerned, both discrete charge versions fall on the same line, which shows a deviating course from the continuous version's behavior in the close-interaxial separation regime, while it approaches the continuous case's curve fast for larger $R$ and both lines agree for $R > 25$ Å. We repeated the analysis of Figs. 1.5 and 1.6 for $N = 20$ charges. Here, no difference to the continuous charge distribution results could be discerned.

We can thus conclude that first the behavior of a DNA assembly will most probably not qualitatively differ for a discrete charge model with the real DNA charge number $N = 10$ and a continuous line charge model. The results will however, in a quantitative manner depend on the underlying pair potential, especially for high concentrations, since, in Figs. 1.4 and 1.6 we found that for very close intersurface separations the pair interactions differed for a discrete and a continuous charge pattern on the DNA surface. Second, since already for $N = 20$ the results are indistinguishable from the ones for continuous line charges, we can furthermore surmise that a modulated continuous line charge distribution, as briefly discussed above to be the most realistic model, would not significantly differ even on the level of the pair potential. According to this reasoning, we will henceforth focus on continuous line charges, thereby avoiding the problem that for discrete charge patterns the potential depends on both molecules' azimuthal orientations $\phi_1$ and $\phi_2$ which significantly complicates matter for the strict analysis of an assembly.

Let us now investigate the effect of different amounts and types of counterions adsorbed on the DNA molecular surface. The type of counterion is herein modeled by the ratio of

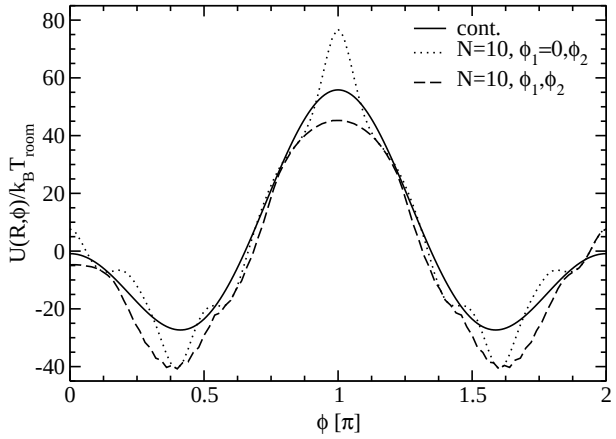


**Figure 1.5:** Yukawa-segment pair potential per length $L_p$ as a function of the azimuthal orientation angle $\phi$ (solid line, continuous line charge distribution), as a function of $\phi = \phi_1 - \phi_2$ with the optimal combination of $\phi_1$ and $\phi_2$ as described in the text (dashed line, $N = 10$ discrete charges) and as function of $\phi_2$ with $\phi_1 = 0$ fixed (dotted line, $N = 10$ discrete charges). All interactions are at an interaxial separation $R = 2.1$ nm, for $\theta = 0.9$ and $f_1 = 0.3$, $f_2 = 0.7$, $f_3 = 0$.

adsorbed charges in the minor and major grooves, as well as on the strands to the DNA phosphate backbone charge. We restrict our analysis to the most relevant cases: We will investigate $\theta = 0.9$ (meaning that 90% of the DNA charge is compensated by adsorbed counterions) with counterions adsorbing predominantly in the major groove, represented by charge fractions $f_1 = 0.3$, $f_2 = 0.7$ and $f_3 = 0$, as well as with counterions exhibiting a high affinity to phosphates and thus condensing on the strands: $f_1 = 0$, $f_2 = 0$ and $f_3 = 1$. A charge compensation value of $\theta = 0.9$ is known to be typical for DNA condensation [18, 5]. Furthermore we calculate the potential for $\theta = 0.7$, which is a lower bound still occurring in DNA aggregation phenomena. Here, we also assume $f_1 = 0.3$, $f_2 = 0.7$ and $f_3 = 0$. In Fig. 1.7 the potential is displayed as a function of the azimuthal angle $\phi$ for two fixed interaxial separations, $R = 2.5$ nm and $R = 3.0$ nm, for $f_1 = 0.3$, $f_2 = 0.7$, $f_3 = 0$ and $\theta = 0.9$ and $q = 0.7$. For both amounts of adsorbed counterions, the potential curves qualitatively agree. Due to the higher degree of charge compensation, however, the $\theta = 0.9$ potential values are smaller. In a subsequent step we minimize the potential with respect to the azimuthal alignment angle $\phi$, obtaining $U(R, \phi_{\text{opt}})$. The result is displayed in Fig. 1.8. Both potentials being induced by situations where the majority of counterions condenses in the major groove, are strongly attractive, with the one for $\theta = 0.9$ exceeding the one for $\theta = 0.7$. The potential stemming from a situation with all counterions condensed on strands, on the other hand is purely repulsive.

What is the origin of this qualitative difference? The mechanism can be thought of as a 'zipper' [18]. Having a high charge compensation in the major groove creates a big charge

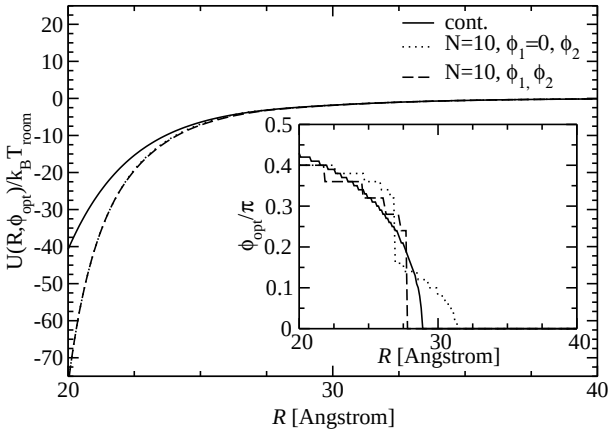


**Figure 1.6:** Yukawa-segment pair potential per length $L_p$ as a function of the interaxial separation $R$ of two DNA molecules, at the optimal azimuthal orientation angle $\phi_{\rm opt}$ (solid line, continuous line charge distribution), at the optimal angle $\phi_{\rm opt} = (\phi_1 - \phi_2)_{\rm opt}$ with the optimal combination of $\phi_1$ and $\phi_2$, as described in the text (dashed line, $N = 10$ discrete charges) and as function of $\phi_2$ with $\phi_1 = 0$ fixed (dotted line, $N = 10$ discrete charges). All interactions are counterion condensation parameters $\theta = 0.9$ and $f_1 = 0.3$, $f_2 = 0.7$, $f_3 = 0$. The dependence of the optimal angle on the interaxial separation $R$ is shown in the inset.

separation: A negative helical line charge is located at the phosphate backbone position, a positive helical line charge rests in the adjacent major groove. With two opposing DNA molecules appropriately oriented, this allows for positive and negative charges to directly face each other as complementary parts in a zipper, creating a strong attraction between the two molecules. If counterion condensation solely occurs on strands, this mechanism is absent, creating a purely repulsive potential, as seen in Fig. 1.8 in the case of $\theta = 0.9$, $f_1 = 0$, $f_2 = 0$, $f_3 = 1$. In any case, the potential quickly decays towards zero for increasing interaxial separations so that in an assembly the dominant contributions to the total potential energy will stem from the nearest neighbors. The optimal angle, as a function of the interaxial separation, plotted in the inset of Fig. 1.8, is practically unaffected by this mechanism: In all three cases displayed, the optimal angle is non-zero for interaxial separations smaller than $R_* \approx 28.25$Å and zero else. Furthermore, a very similar increase from zero at $R_*$ to $\phi_{\rm opt}(R = 0) \approx 0.47\ \pi$ is observed in all cases.

Let us finally remark that the Yukawa-segment model has the advantage of being very general and flexible. Any linearized field theory necessarily ends up with an effective Yukawa-type interaction. If hydration effects are included within a field theoretical description, the leading term for the effective interaction has again a Yukawa form. The electrostatic effects are well described even at strong coupling provided the charges and screening lengths are suitably renormalized as recently demonstrated in micro-ion resolved computer simulations of two parallel DNA strands [20].

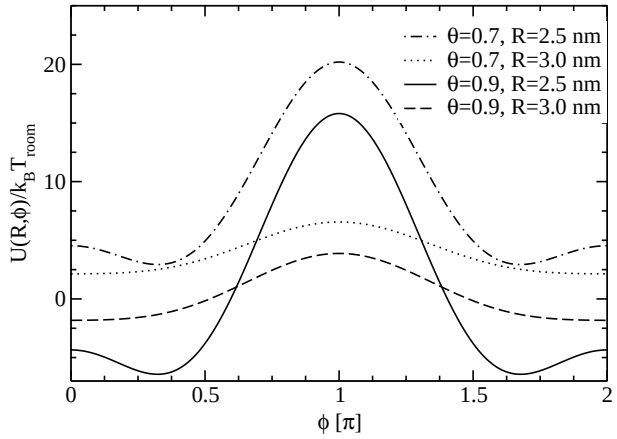


**Figure 1.7:** Yukawa-segment pair potential for two segments of length $L_p$ as a function of the mutual azimuthal orientation angle $\phi$ of two DNA molecules, at fixed interaxial separations as indicated in the legend, for $\theta = 0.9$. $\theta = 0.7$, and $f_1 = 0.3$, $f_2 = 0.7$, $f_3 = 0$ were used for the fractions of condensed counterions in the minor and major groove and on the strands, at different interaxial separations as indicated in the legend.

### 1.3.2 Kornyshev-Leikin Potential

The Kornyshev-Leikin approach rewrites the result of linear screening theory in terms of a 'helical Fourier expansion' ($\epsilon_1 \ll \epsilon$) [14, 49, 65]. The pair interaction potential per unit length features a hard-core repulsion for interaxial separations $R \leq 2a$ and for $R > 2a$ reads as:

$$\begin{aligned} \frac{u(R,\phi)}{u_0} &= \sum_{n=-\infty}^{\infty} \left[ f_1\theta + (-1)^n f_2\theta - (1 - f_3\theta)\cos(n\tilde{\phi}_s) \right]^2 \\ &\times \quad \frac{(-1)^n \cos(ng\Delta z) K_0(\kappa_n R) - \Omega_{n,n}(\kappa_n R, \kappa_n a)}{(\kappa_n/\kappa)^2 [K_n'(\kappa_n a)]^2}, \end{aligned} \tag{1.9}$$

The total interaction $U(R,\phi)$ per segment of length $L$ is simply $U(R,\phi) = L\ u(R,\phi)$. In Eq. (1.9) $\Delta z$ denotes a vertical displacement, equivalent to the azimuthal alignment angle $\phi = (2\pi/H)\Delta z$. Furthermore, $u_0 = 8\pi\sigma^2/\epsilon\kappa^2$ ($\approx 2.9\, k_B T/\text{Å}$ at physiological ionic strength), and $\kappa_n = \sqrt{\kappa^2 + n^2 g^2}$. The function $\Omega_{n,m}(x,y)$ is given by

$$\Omega_{n,m}(x,y) = \sum_{j=-\infty}^{\infty} \left[ K_{n-j}(x) K_{j-m}(y) \frac{I_j'(y)}{K_j'(y)} \right], \tag{1.10}$$

with the modified Bessel functions $K_n(x)$ and $I_j(y)$. The primes denote derivatives. As can be seen, the dependence of the pair potential on the mutual orientation angle $\phi$ is affected by the distributions $f_i$, $i = 1, 2, 3$ of the condensed counterions [18]. The dependence on the interaxial separation $R$ is exponential. Keeping only the $n = 0$-term in the sum of Eq. (1.9)

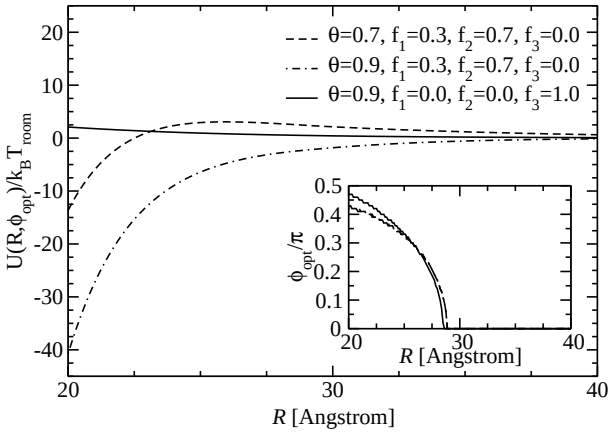


**Figure 1.8:** Yukawa-segment pair potential for two segments of length $L_p$ as a function of the interaxial separation $R$ of two DNA molecules, at the optimal angle $\phi_{\rm opt}(R)$, depicted for different values of the counterion condensation parameter and for different counterion adsorption patterns. The dependence of the optimal angle on the interaxial separation $R$ is shown in the inset.

yields a pair potential of homogeneously charged cylinders, depending on $R$ only. Summing up to $|n| = 2$ results in the approximation $u(R,\phi) \cong C(R) - A(R)\cos\phi + B(R)\cos^2\phi$. Already at this level does the interaction potential $u(R,\phi)$ show a peculiar dependence on the mutual azimuthal orientation angle, being a remarkable effect of DNA double strandedness, as discussed above in Sec. 1.3.1. Here, $A(R)$, $B(R)$, $C(R) > 0$ depend on the parameters of DNA structure as well as on the distribution of adsorbed ions, and $A(R) > B(R)$ at large interaxial separations $R$. This potential has two symmetric azimuthal minima at $\hat{\phi}_\pm \neq 0$ for distances smaller than a critical one at which $A(R) = 2B(R)$, and one minimum at $\hat{\phi} = 0$ for larger $R$. It thus already captures, to quite a good degree, the essential features of the full interaction potential as observed in the previous section in the framework of the Yukawa-Segment model.

Let us now investigate the full potential. Due to rapid convergence of the sum in Eq. (1.9), truncation after the $|n| = 5$ terms suffices for the evaluation of the fully converged pair interaction potential. In Fig. 1.9 we show the KL-potential $U(R,\phi_{\rm opt})$ at optimized azimuthal alignment angle, $\phi_{\rm opt}$, as plotted for the YS-case in Fig. 1.8. It can be seen that the results are very similar to the ones discussed above for the YS potential. Counterion condensation on strands ($f_1 = 0$, $f_2 = 0$ and $f_3 = 1$) gives rise to an exclusively repulsive potential, whereas condensation of a majority of the counterions in the major groove ($f_1 = 0.3$, $f_2 = 0.7$ and $f_3 = 0$) results, at both charge compensations $\theta = 0.7$ and $\theta = 0.9$, in an attractive pair interaction. Differences in the KL approach to the YS approach can however also be inferred from a comparison of Fig. 1.9 and Fig. 1.8. These refer to the behavior at small intersurface separations. In the case of the YS model, the interaction decays monotonically to the 'contact value' at $R = 20\,$Å. Here, for the KL potential,

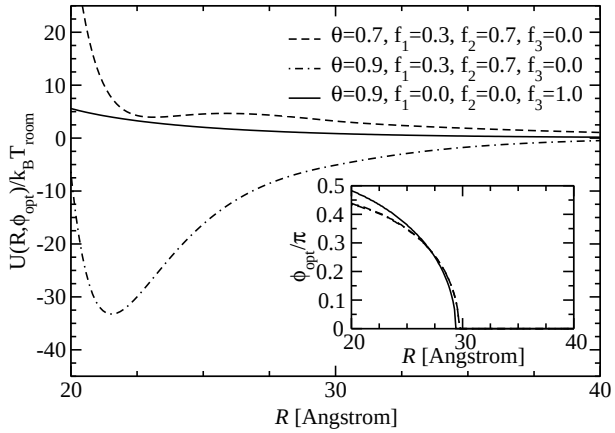


**Figure 1.9:** Kornyshev-Leikin pair potential as a function of the interaxial separation $R$ of two DNA molecules, at the optimal angle $\phi_{\rm opt}(R)$, depicted for different values of the counterion condensation parameter and for different counterion adsorption patterns. The dependence of the optimal angle on the interaxial separation $R$ is shown in the inset.

however, the potential drops to its minimum value close to surface contact, but then rises again upon further approach. Furthermore a quantitative difference can be seen for $\theta = 0.7$ and $f_1 = 0.3$, $f_2 = 0.7$, $f_3 = 0$, since in the KL case the attraction for this combination of parameters is much weaker than it was found to be for the YS model. Both observations can be attributed to the fact that in the KL case the dielectric jump is taken into account with $\epsilon/\epsilon_1 = \infty$, where $\epsilon$ is the dielectric constant of the solvent (water) and $\epsilon_1$ is the dielectric constant of the DNA core. This allows for image charges at the DNA surface, bringing about a short-ranged repulsive part in the interaction, as evidenced in the potential curves in Fig. 1.9. Nonetheless this short-range repulsion does not affect the behavior of the optimal angle as a function of the interaxial separation as compared to the one found in the YS case. We show the corresponding data in the inset of Fig. 1.9. The same functional form as for the YS potential is obtained, except for the fact that $R_*^{\rm KL} \approx 29.5\,\text{Å}$ is found to be slightly larger than $R_*^{\rm YS} \approx 28.25\,\text{Å}$ in the YS case.

We now have two realizations of the linear Debye-Hückel potential for the DNA interaction at hand stemming from different levels of modeling realized in the Debye-Hückel framework, which show differences with respect to the short-range behavior. In the following section we will present a theory to investigate the statistical properties of a columnar DNA assembly. We will thereby rely on the two YS and KL potentials as discussed above. The interesting question to be pursued apart from the main objective, being the general properties of such assemblies, is, if and how the differences in the pair potentials affect the behavior of the assembly.

## 1.4 A Theory for DNA assemblies

In the previous sections we showed that under the assumption of continuous line charges and infinitely long, rigid, parallel DNA molecules, the pair interaction potential $U(R,\phi)$ of two DNA molecules only depends on the interaxial separation $R$ and the mutual azimuthal orientation angle, $\phi$. The problem of statistical properties of columnar aggregates of long rigid DNA molecules may thus be mapped on a 2d-problem of particles that we may formally refer to as 'XY-spins', interacting via this unusual potential $U(R,\phi)$, (see Fig. 1.2), [14]. We repeat from Sec. 1.3.1 and 1.3.2 that the dominant contributions to the potential $U(R,\phi)$ arise from the nearest neighbor interactions, as the $R$-dependent parts of the potential exponentially decrease with $R$. Before going into more detail on the theory for DNA assemblies we can, on the basis of the knowledge of the pair potential, already surmise a general trend in the behavior: We know that the potential has two symmetric azimuthal minima at $\hat{\phi}_{\pm} \neq 0$ for distances smaller than a critical one and one minimum at $\hat{\phi} = 0$ for larger $R$. While the $\hat{\phi} = 0$-case is compatible with any lattice, $\hat{\phi} \neq 0$ results into *frustrations* of positional and orientational order [66]. Due to the '$R - \phi$ coupling' in the interaction potential, one may expect peculiar positional and orientational structures in the aggregate, a feature known as the mesomorphism of DNA assemblies [40]. Carrying the formal analogy to spin systems further, we may refer to the orientational structure in the assembly also as 'spin' or 'magnetic' structures.

### 1.4.1 Lattice Sums

For all cases studied in this chapter, the pair interaction $U(R,\phi)$ is greater than $k_BT$, so that the energy needed to destroy the translational or orientational order in an assembly must be more than several $k_BT$ at room temperature. Hence focusing on the ground state-analysis of the basic structures of the assembly provides the representative thermodynamic states. This reasoning is further sustained by evidence from polymer crystallization, stating that upon compression the effective persistence length of polymers increases, bringing them into columnar alignment at high packing fractions [67, 68]. Since, as we already argued above, the problem is effectively two-dimensional, we consider the five two-dimensional Bravais lattices, i.e., the hexagonal ($HEX$), square ($SQ$), rectangular ($REC$), rhombic ($RHO$) and oblique ($OBL$) lattices in order to assess the representative thermodynamic states. As for the exploration of the *ordered* spin structures, we are, in principle, facing infinitely many degrees of freedom: Every DNA molecule in the lattice has a continuous spectrum of possible orientations. We can, however, make use of a pair potential property that we noted in Sec. 1.3, namely that the pair interaction drops exponentially as a function of the interaxial separation $R$. Assuming that its range would solely encompass interactions contained in a fundamental unit cell (elementary plaquette), the approach could be much simplified in the following way. We restrict our analysis to finding the minimal energy state of this fundamental unit cell *alone*. This is achieved by minimizing the energy of the plaquette

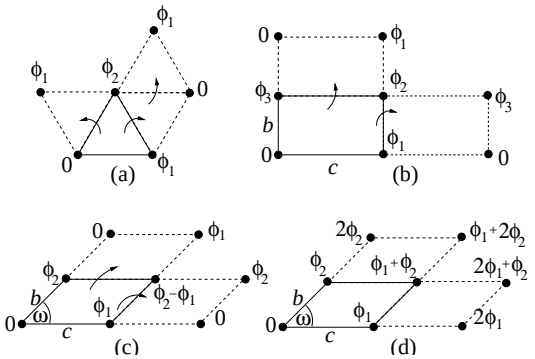


**Figure 1.10:** A schematic view of generating candidate ordered spin phases of the system. (a): for the *HEX*-lattice; (b): for the *REC*- and *SQ*-lattices; (c) and (d): for the *RHO*- and *OBL*-lattices.

with respect to all spin angles residing on the elementary plaquette. Since no interactions beyond unit cells are assumed to be present, periodical repetition of this 'minimized' unit cell along the lattice directions guarantees to give the ground state of the *whole* lattice. Due to the exponential decay of the $R$-dependent factors in the pair interaction potential this already presents an amazingly good approximation for our purposes. Since strictly speaking the range of the potential may extend beyond nearest neighbor interactions in some cases, we adopt a perturbation approach in the following way: The whole lattice is generated by periodical repetition of the elementary plaquette structure, involving two or three degrees of freedom depending on the lattice type under exploration, but interactions of higher-order-neighbors are nonetheless included in the calculation of the lattice sums.

The algorithms employed for generating the ordered spin structures on the whole lattice building on the fundamental unit cell differ depending on the lattice type. They are schematically illustrated in Fig. 1.10. One of the spins in the elementary plaquette is chosen as reference ($\phi = 0$). This leaves two degrees of freedom ($\phi_1$, $\phi_2$) in the case of the *HEX* lattice and three degrees of freedom ($\phi_1$, $\phi_2$, $\phi_3$) for the *REC*- and *SQ*-lattices. The *HEX* lattice can be build up by periodically reflecting the unit cell across its edges, as is shown in Fig. 1.10(a). The same holds for the *REC* lattice with three free orientations per plaquette, see Fig. 1.10(b). In the case of the *RHO*- and *OBL*-lattice, however, employing the same procedure as for the *REC*-lattice with three free spin angles per plaquette does not produce identical plaquettes: Due to the fact that the geometrical symmetry of the unit cell is broken (a short and a long diagonal exist), mirror reflections across the edges generate different plaquettes on the whole lattice. The lattice may nonetheless be filled with identical plaquettes by employing two algorithms which are depicted in Fig. 1.10(c) and 1.10(d). In the first, spins of orientation $\phi_1$ and $\phi_2$ are placed along the edges, while the third free orientation angle is chosen to be $\phi_3 = \phi_2 - \phi_1$. The whole lattice is then populated by successive mirror reflections making safe that pairs of spins across all diagonals have the same relative angle

of $\phi_2 - \phi_1$.

The second algorithm is illustrated in Fig. 1.10(d). Again, spin angles of values $\phi_1$ and $\phi_2$ are chosen along the edges, while $\phi_3$ is assigned a value of $\phi_1 + \phi_2$. The lattice is then build up by increasing the angular value by $\phi_2$ along the oblique direction and by $\phi_1$ along the horizontal lattice direction. The resulting lattice exhibits unit cells in which all pairs of spins across short diagonals have an angle difference of $\phi_1 - \phi_2$, whereas pairs of spins across long diagonals are separated by an angular difference of $\phi_1 + \phi_2$.

Lattice sums are then calculated and a minimization of the lattice energy with respect to the orientational degrees of freedom $\{\phi_i\}$, the geometrical degrees of freedom, being the size ratios $b/c$ for the *REC*-lattice and/or the geometrical angle $\omega$ for *RHO*- and *OBL*-lattices, see Fig. 1.10, is carried out. The result of the minimization procedure is the optimized lattice-sum energy, $U_{\rm X}(\mathbf{\Phi}, \rho)$, where X stands for the lattice type and $\mathbf{\Phi} = (\phi_1, \phi_2, \ldots, \phi_N)$ denotes the configuration of the $N$ spins in the system.

Three examples of lattice sums for fixed DNA density $\pi\rho a^2$ and fixed salt concentration $n_s$ at a charge compensation $\theta = 0.9$ and $f_1 = 0$, $f_2 = 0$, $f_3 = 1$ are displayed in Figs. 1.11(a) through(c). They depict the total energy stemming from the lattice sum as contour plots as a function of $\phi_1$ and $\phi_2$ They are representative of three different phases emerging for these parameters. The meaning of the three phases will be explained in detail in Sec. 1.5. It can be clearly discerned from the contour plots that a certain symmetry prevails in the aggregate with respect to $\phi_1$ and $\phi_2$ whereby the symmetry axis is the line $\phi_1 = \phi_2$. The location of the minima evolves from $\phi_1 = 0.21$, $\phi_2 = 0.42$ (Fig. 1.11(a)) via $\phi_1 = 0.46$, $\phi_2 = 0.46$ (Fig. 1.11(b)) to $\phi_1 = 1/3$, $\phi_2 = 2/3$ (Fig. 1.11(c)), whereby lattice sums at correspondingly symmetric angles are found to have equally low values.

The 2d DNA-concentration $\rho$ is varied within $0 \leq \rho a^2 \leq 1/(2\sqrt{3})$, the upper limit being the close-packed configuration in a *HEX*-lattice. We vary the salt concentration $n_s$ in the assembly within 0.0001mol/l $\leq n_s \leq$ 3mol/l, including strongly deionized situations and physiological salt concentrations. For the lower limit of the 2d DNA concentration the following remark is in order. The molecules remain parallel down to density $\rho a^2 \approx 0.1$, corresponding to interaxial separations $R \approx 34\,\text{Å}$, at which the cholesteric phase (CP) appears [43, 45, 69, 55]. A theory of the CP is beyond the scope of this work, thus we draw our phase diagrams down to $\rho a^2 = 0$, with the reminder that for large interaxial separations the CP is stable. Although the CP is not included in the present theory, we have, for low 2d DNA-concentration, to take into consideration the low-density 2d-fluid. We achieve this by the following scheme: For every screening parameter $\kappa$ which is associated with a given phase point $(\rho, n_s)$, we map the interaction potential for $\phi = 0$, given by Eq. (1.5) or (1.9), respectively, onto an effective hard-disc interaction potential, making use of the Barker-Henderson rule [70], providing us with the effective hardcore diameter $d(\kappa)$. Using the known result $(\pi/4)\rho_m d(\kappa)^2 = 0.691$ for the melting density $\rho_m$ of hard-disc systems [71], the melting line can be estimated.

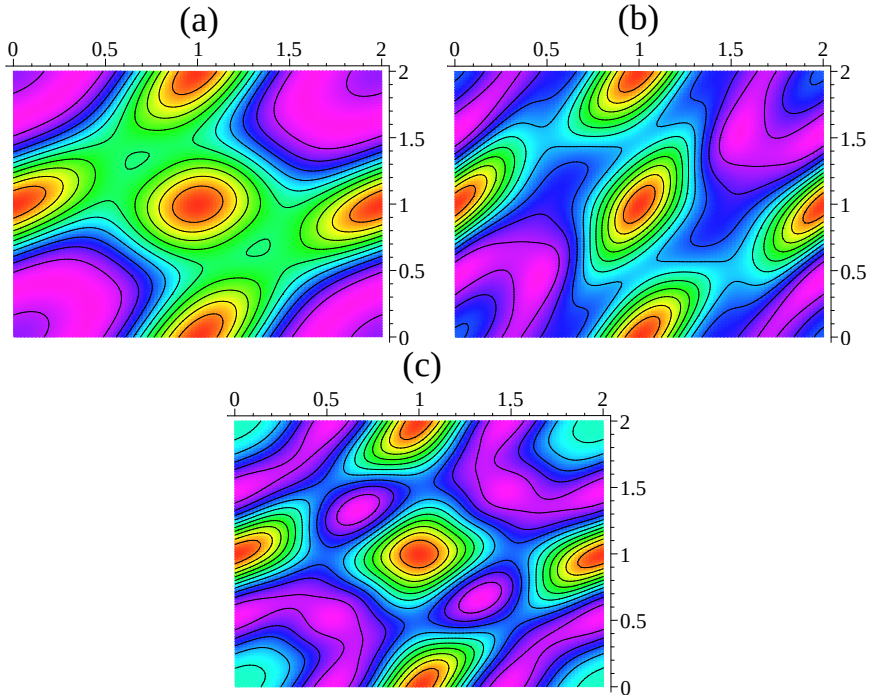


**Figure 1.11:** Lines of constant energy as stemming from lattice sum calculations of DNA-salt mixtures for the KL model as a function of the azimuthal angles $\phi_1$ and $\phi_2$, with $\theta = 0.9$ and $f_1 = f_2 = 0$, $f_3 = 1$. Pink color indicates low energies while red encodes high energy values. The lattice here is *HEX*. (a) $\pi\rho a^2 = 0.44$, $n_s = 0.2$ mol/l (b) $\pi\rho a^2 = 0.60$, $n_s = 0.2$ mol/l (c) $\pi\rho a^2 = 0.75$, $n_s = 1.7$ mol/l.

### 1.4.2 Volume and kinetic energy terms

To access the full thermodynamics of the DNA solution-salt mixture, we have to add the contributions to the free energy stemming from the counter- and co-ions, with numbers $N_\pm$ and concentrations $c_\pm$, respectively. In a simplified picture, they can be thought of as the entropic, ideal-gas-like contributions of the free, non-condensed counterions (kinetic energy terms) and the interaction of the DNA-macroions with their associated double-layer of salt-microions. These degrees of freedom contribute an extensive term, independent of particle coordinates and momenta, to the free energy of the system, with terminology footing on the volume terms' extensivity. Although the volume terms lack the dependence on the current phase point of the system, they still represent an important contribution to the total free energy of the system, as they constitute a nontrivial, non-vanishing *density-dependent* term in the Hamiltonian. They are of importance in a wide number of multi-component systems, i.e. Ashcroft and Stroud [72] noted their influence on mixtures with quantum and classical components, Rowlinson [73] pointed out their relevance in general terms, Grimson and coworkers [74, 75] analyzed their influence on charged colloids and they were calculated by Graf and Löwen [76] for charge-stabilized colloidal suspensions, see also van Roij [77]

and Denton [78, 79]. For charged cylindrical molecules Graf and Löwen calculated the contributions from volume and kinetic energy terms to be [64],

$$F_{\rm c} = F_+^0 + F_-^0 + F_{\rm coh}, \tag{1.11}$$

where $F_\pm^0 = N_\pm\, k_B T\, \left[\ln(c_\pm \Lambda_\pm^3) - 1\right]$ are the ideal-gas contributions (with $\Lambda_\pm$ being the thermal de Broglie wavelengths of the counter- and co-ions) and

$$F_{\rm coh} = -\frac{1}{2}\left[\frac{2Na(Ze)^2\kappa}{\epsilon L_p(1+\kappa a)} + \frac{k_B T\, V(c_+ - c_-)^2}{c_+ + c_-}\right], \tag{1.12}$$

is a cohesive term. In Eq. (1.12), $e$ is the electron charge, $Z|e| = 2\pi a L_p \sigma(1-\theta)$ is the uncompensated DNA-charge, $c_+ = Z\rho/L_p + n_s$ and $c_- = n_s$. Finally, $V$ is the volume of the system and $\kappa = \sqrt{4\pi(Z\rho/L_p + 2n_s)e^2/(\epsilon k_B T)}$ for monovalent salt ions.

The total Helmholtz free energy for a given lattice type X is then given as the sum of the lattice sum of the DNA assembly, $U_{\rm X}$, and the volume and kinetic energy terms of the salt solution, $F_{\rm c}$: $F = U_{\rm X} + F_{\rm c}$.

## 1.5 The phase diagram

We now apply the considerations of the previous section to the calculation of the phase diagrams of columnar DNA assemblies. Let us focus on the YS model for the moment and then turn our attention to the KL model. The first choice of parameters we investigate corresponds to the adsorbed counterions being exclusively condensed *on strands*, i.e, $f_1 = f_2 = 0$ and $f_3 = 1$. In this case the DNA-DNA interaction is purely repulsive, see, e.g., Figs. 1.8 and 1.9. Correspondingly, we find the system to crystallize into the *HEX* lattice at all DNA-densities. Hexagonal lattice structures are evidenced in sperm nuclei and a number of bacteriophages [45] and were also observed *in vitro* [80, 81, 82]. Adding to the repulsive $R$ dependent interaction, the effect of the nontrivial $R$-$\phi$-coupling is present, giving rise to a large variety of orientational ('spin', 'magnetic') structures to occur due to the azimuthal frustration of the system. The orientational structures are schematically shown in Fig. 1.12 and the phase diagram of the DNA-salt mixture is plotted in Fig. 1.13. Four different orientational phases can be discerned. The *FM*-phase is stable at low DNA-concentrations. It is ferromagnetic: all DNA-molecules have the same azimuthal orientation. The *AFP* phase has a three-state antiferromagnetic Potts [83] type of ordering, with 1/3 of the spins pointing in a reference direction $\phi = 0$, 1/3 in the angle $\phi_0$ and 1/3 in the angle $2\phi_0$, where $\phi_0$ grows with DNA concentration. The phase denoted *AFI* displays antiferromagnetic-Ising ordering, with half of the DNA-molecules having one azimuthal orientation on one of the sublattices and a different on the other. Finally, the *AFH*-phase has the orientational ordering of the two-dimensional antiferromagnetic Heisenberg model, with spins residing in the three sublattices of the hexagonal lattice having mutual orientational angles of 120 ° to one another. The *AFH* phase is thus a special case of the *AFP* phase. The transition between the *FM* and

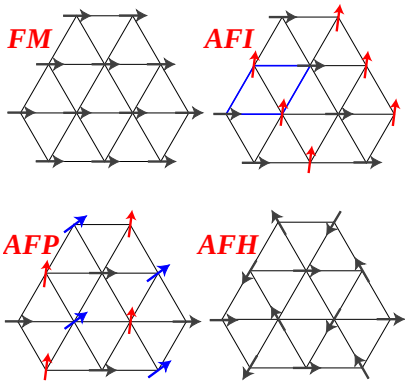


**Figure 1.12:** The four stable 'magnetic' phases. The arrows indicate the azimuthal orientations of DNA molecules. The acronyms, using magnetic terminology, stand for *ferromagnetic* (*FM*), *antiferromagnetic Ising* (*AFI*), *antiferromagnetic Potts* (*AFP*), and *antiferromagnetic Heisenberg* (*AFH*).

*AFP* phases is second-order but the $AFP \rightarrow AFI$ and $AFI \rightarrow AFH$ transitions are first order with very narrow density gaps [76]. As can be seen, for the average intermolecular separations occurring in the *FM* phase, the optimal azimuthal angle between the molecules is zero. The nontrivial phases arise at higher densities of the aggregates, as a result of the frustrated character of the $\phi$-dependence of the pair potential. Similar mesophases were found recently within the framework of a phenomenological Landau theory [50]. Representative lattice sums for the *AFP*, *AFI* and *AFH* phases are shown in Fig. 1.11. Including the 2d fluid estimate into the calculation, parts of the phase diagram at lower 2d DNA densities get preempted by the 2d fluid, as is shown in Fig. 1.14(a).

Changing the type of counterions present in the solution to counterions with a preference to adsorb into the *major groove*, i.e. choosing $f_1 = 0.3$, $f_2 = 0.7$ and $f_3 = 0$, drastically changes the picture. As we showed in Sec. 1.3, the counterion condensation in grooves provides a 'zipper' mechanism, leading to an attraction between the DNA-molecules, since the positively charged sections of one molecule can approach the negatively charged sections of the other through an appropriate mutual orientation. This attraction leads to non-convex parts in the Helmholtz free energy $F(\rho, n_s)$, causing an instability in this regime, as non-convexity means, via $P = -\partial F/\partial V$, regions of negative pressure in the system. Performing a double tangent construction removes the non-convex parts in the free-energy curve and thereby yields broad phase-coexistence tielines between dense DNA-aggregates and DNA-free solutions, connecting coexisting $(\rho, n_s)$ state points. See Appendix A for a more detailed discussion. The occurrence of a broad phase-coexistence regime can be seen in Fig. 1.14(b) for the case $f_1 = 0.3$, $f_2 = 0.7$ and $f_3 = 0$ for $\theta = 0.7$. The oblique tielines result from the requirement that the electrolyte chemical potentials be equal at both coexisting phases, as is explained in more detail in Sec. A. In the one-phase region, a rhombic phase with an *AFI* orientational structure shows up for the density regime directly adjacent to the phase

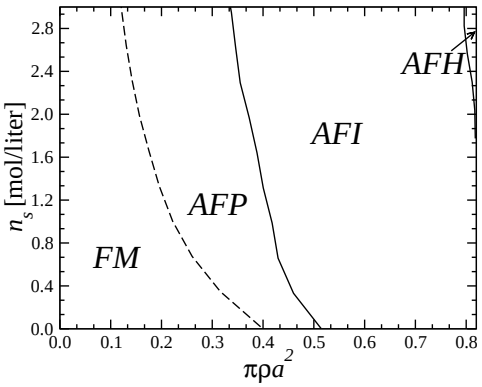


**Figure 1.13:** Phase diagram of DNA-salt mixtures for the YS model as a function of the DNA packing fraction $\pi\rho a^2$ and salt concentration $n_s$ in the aggregate: $\theta = 0.9$, $f_1 = f_2 = 0$, $f_3 = 1$, the lattice here is *HEX*. Dashed lines denote second-order magnetic transitions, solid lines first-order ones.

coexistence line and a *HEX* crystal with *AFP* 'magnetic' ordering appears at very high DNA-concentrations. One might have a priori conjectured that a *SQ*-phase with orthogonal magnetic order would win the game at high concentrations in the solely attractive YS case, since the angular part of the interaction favors $\approx \pi/2$ angular ordering for small separations and would thus be non-frustrated on a *SQ* lattice, see Fig. 1.15. It has to be kept in mind however, that although one has, for a given packing fraction, four neighbors closer in a *SQ* lattice than in a *RHO* or *HEX* lattice at the same packing fraction, which is favorable without repulsions, in a *HEX* lattice there are *six* neighbors at a slightly larger distance. The same effect is present in a *RHO* lattice although there the symmetry is broken with four nearest and four next-nearest neighbors as in the *SQ* lattice, but with another nearest neighbor distance to next-nearest neighbor distance ratio, which turns out to favor the *RHO* lattice with the potential curve that we have in the YS case. Increasing $\theta$ to 0.9 does not qualitatively affect the phase diagram. The DNA-aggregate coexistence with DNA-free solutions turns out to be slightly broader, due to stronger attractions prevailing in the pair potential. The results are depicted in Fig. 1.14(c). We thus observe a significant *qualitative* difference in the macroscopic behavior of DNA columnar assemblies depending on the type of adsorbed counterions. If they solely adsorb on strands, i.e. $f_1 = f_2 = 0$ and $f_3 = 1$, all phase transitions occur in the azimuthal variables. With counterions condensed in grooves, a DNA bundling transition into a high DNA density rhombic phase takes place. The crossover from one topology (no DNA bundling) to the other (DNA bundling) can be estimated by holding $f_1 = 0.3$ fixed and increasing $f_2$ at the cost of $f_3$. For a charge compensation parameter $\theta$ of e.g. $\theta = 0.7$ it is found to occur at $(f_2, f_3) = (0.63, 0.07)$. Here, all phase diagrams are plotted as a function of the electrolyte concentration in the aggregate. Taking into account the Donnan equilibrium [84], the phase diagrams, recalculated as a function of the salt in the reservoir, are qualitatively the same as the ones shown.

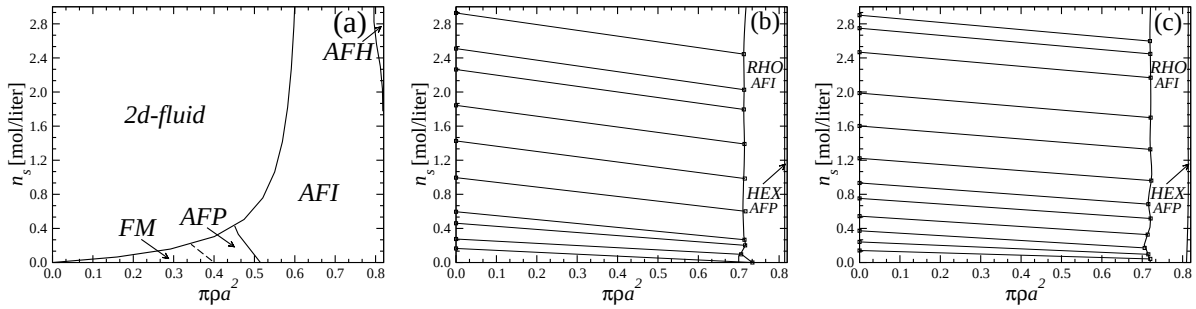


**Figure 1.14:** Phase diagrams of DNA-salt mixtures for the YS model as a function of the DNA packing fraction $\pi\rho a^2$ and salt concentration $n_s$ in the aggregate: (a) $\theta = 0.9$, $f_3 = 1$, the lattice here is *HEX*. (b) $\theta = 0.7$, $f_1 = 0.3$, $f_2 = 0.7$; (c) $\theta = 0.9$, $f_1 = 0.3$, $f_2 = 0.7$. Dashed lines denote second-order magnetic transitions, solid lines first-order ones. The geometrical transitions between different lattices in (b) and (c) are 2nd order; the straight lines are tielines between coexisting phases.

The same procedure is now applied to the KL pair potential. Again, we first investigate $\theta = 0.9$ and $f_1 = f_2 = 0$ and $f_3 = 1$. The phase diagram is shown in Fig. 1.16(a). It is apparently very similar to the corresponding phase diagram of the YS model. The orientational structures found are the same as in the latter case and even the loci of the phase transitions are practically unchanged, except for the $AFI \rightarrow AFH$ transition, which occurs for lower $\rho$ and $n_s$ values. The 2d fluid regime is smaller, being sign of the fact that the KL pair potential is steeper, i.e., stronger repulsive than the YS pair potential due to the image charge effect included in the KL model. Switching to counterion condensation in grooves, i.e. $f_1 = 0.3$, $f_2 = 0.7$, $f_3 = 0$, again broad phase coexistence regions of a high-density DNA aggregate with a DNA free salt solution are observed, see Figs. 1.16(b) and (c). For the case of the lower of the two charge compensation parameters investigated, $\theta = 0.7$, the high-density DNA assembly does not coexist with a DNA-free salt solution at all salt concentrations $n_s$, but rather coexists with a low-density *HEX* crystal with an imprinted *FM* orientational structure in the low salt concentration regime. This is, in this respect, qualitatively different from the corresponding phase diagram found in the case of the YS interaction. It is due to the much less attractive KL pair potential, as can be seen from a comparison of the curves for $\theta = 0.7$ in Figs. 1.8 and 1.9. Due to the same reason the phase coexistence region turns out to be narrower for $\theta = 0.7$ than it is for $\theta = 0.9$, see again Figs. 1.16(b) and (c). The same statement holds for a comparison of the KL phase diagrams with the YS phase diagrams. While in both cases the high-density DNA assembly exhibits a *RHO* lattice with *AFI* orientational order and then a transition to a *HEX* crystal complemented by an *AFP* 'magnetic' structure, the phase coexistence region is significantly broader in the latter case. This behavior can be traced back to the pair potential in the same manner as above: The YS interaction has a stronger attractive part and lacks the repulsive branch for close-intersurface separations, see Figs. 1.8 and 1.9, the bundling transition induced by the

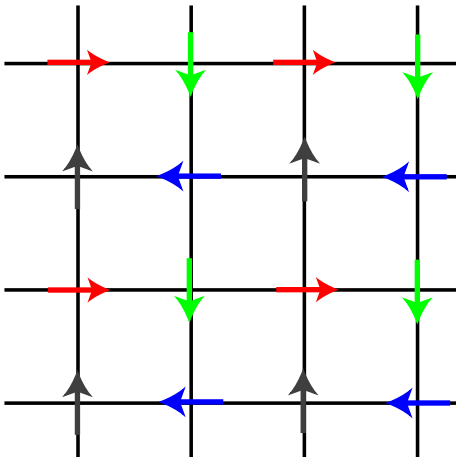

**Figure 1.15:** A possible $SQ$ phase with orthogonal 'magnetic' ordering.

strong 'zipper' attractions will thus favor smaller interaxial separations between the bundled DNA molecules.

## 1.6 Summary and concluding remarks

Summarizing, we calculated the phase diagrams for columnar DNA assemblies, building on different levels of approximation in the pair interaction potential. We found that details of the interaction as manifest by the two potentials used for calculating the phase diagrams are not destroying the topology of the phase diagrams. The resulting phase diagrams showed significant agreement for the case of repulsive interactions, induced by counterion condensation on strands. For counterion condensation in the grooves, yielding strongly attractive interactions, the phase diagrams qualitatively agreed for the high charge compensation value, $\theta = 0.9$, whereas for a lower charge compensation of $\theta = 0.7$, an additional low-density $HEX$ DNA phase was present in the KL model phase diagram which was absent in the YS case.

In conclusion we could put forward qualitatively robust predictions for the features and phase diagrams of columnar DNA assemblies. An experimental verification of the predictions of the theory would be highly desirable. Such a task however poses severe problems since the reliable experimental data available up to date pertain to highly concentrated phases [85, 86, 87], corresponding to small interaxial separations of the DNA molecules. In this regime the number of the basic assumptions inherent to the form of the pair potential may be questioned. The Debye-Bjerrum approximation becomes inadequate, as well as the independence of solvent dielectric constant on the aggregate density is questionable at high aggregate densities. Furthermore effects of nonlocal polarizability, and, more important, hydration effects come into play. The increase of experimental resolution in X-ray diffraction could open the way for the study of less dense aggregates. Particularly challenging is the predicted specific effect of cation adsorption on the phase diagram. Since the adsorption

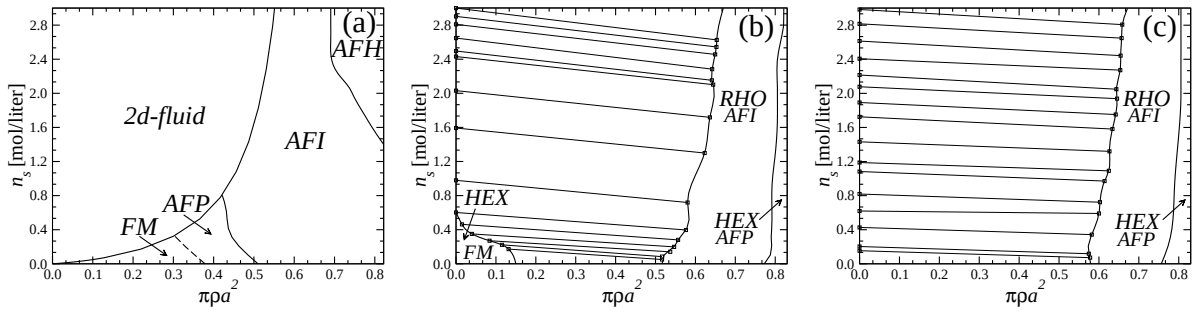


**Figure 1.16:** Phase diagrams of DNA-salt mixtures for the KL model as a function of the DNA packing fraction $\pi\rho a^2$ and salt concentration $n_s$ in the aggregate: (a) $\theta = 0.9$, $f_3 = 1$, the lattice here is *HEX*. (b) $\theta = 0.7$, $f_1 = 0.3$, $f_2 = 0.7$; (c) $\theta = 0.9$, $f_1 = 0.3$, $f_2 = 0.7$. Dashed lines denote second-order magnetic transitions, solid lines first-order ones. The geometrical transitions between different lattices in (b) and (c) are 2nd order; the straight lines are tielines between coexisting phases.

isotherms and the distributions of the adsorbed ions are poorly known, one should concentrate here on qualitative effects, i.e., the (dis)appearance of mesophases triggered by different DNA condensing counterions.

While in this work we focused on DNA as representative for helical (bio)molecules, the approach presented is, in general not at all restricted to DNA alone, rather can all types of molecules bearing helical charge patterns, such as RNA, collagen, guanosine, viral particles (e.g. tobacco mosaic virus), polysaccharide helices and alpha-helical domains of many proteins as well as microtubules be treated within the same framework. Furthermore the formalism used here is not restricted to columnar assemblies, rather may it be applied to other systems, such as bundles of $\alpha$-helices, which form domains in many proteins, interactions between transmembrane $\alpha$-helices and DNA-DNA interaction in nucleosomes, where only locally a parallel alignment of helical charge patterns may be assumed.

*In the next chapter we will apply a similar concept, namely ground state calculations, to the issue of colloidal decoration lattices on patterned substrates. The solution will, however, be rendered more simple with respect to the pair potential: we will employ hard-sphere like colloids with a spherically symmetric potential. The macroscopic order, induced in DNA assemblies by means of the molecules' helicity, can, due to the high degree of symmetry in the colloids not be generated by their internal structure, but will rather be a result of an external potential: the patterned substrate.*

# Chapter 2

# Decoration lattices of colloids adsorbed on stripe-patterned substrates

*All real world systems, except for the universe as a whole, are limited in space and are, depending on the relative system size to a lesser or higher degree non-bulk systems. For one thing, this complicates matter considerably, since physicists have good reason to prefer the study of bulk behavior. On the other hand, external influence on the system in the form of confining geometries can open up routes to completely new effects. In the realm of nanotechnology and self-assembly, influences from the confining substrate are essential. By employing appropriately patterned substrates, chemical, as well as nucleation and adsorption processes can be controlled. In this chapter we investigate the adsorption of model colloids on stripe-patterned substrates. We focus on the equilibrium ground state structures and find that by tuning the model parameters, different complex colloid structures on the substrate can be induced.*

## 2.1 Introduction

Recent advances in microfabrication have allowed to prepare chemically or topographically patterned substrates in a controlled way by using e.g. lithographic printing or other etching techniques [88, 89]. There is a profound influence of such a substrate pattern on wetting [90, 91, 92, 93, 94, 95, 96, 97], on adsorption of soft matter [98, 99] and biological macromolecules [100, 101], on crystal nucleation [102] and on bulk phase transitions such as freezing [103, 104] and fluid-fluid phase separation [105]. Patterned substrates have also been used in so-called microfluidics in order to control chemical reactions on a micro- or nano-scale [106, 107]. For this purpose, one-dimensional channels are considered that carry the reacting material. These channels can either be attractive stripes or topographical groves.

In this chapter we study the adsorption of colloidal particles on a sticky periodic stripe-

like pattern. Our motivation to do so is first coming from experiments where decorations were obtained by adsorbing colloidal spheres on a patterned substrate mask [108, 109, 110, 98, 111, 112, 113, 114, 115, 116], or in an external laser field [117], for a recent review see [118]. Such a decorated substrate may be offered as a template to other mobile colloidal particle in order to nucleate further colloidal crystalline sheets and to grow "exotic" colloidal bulk crystals [119, 120, 103]. The colloidal particles can both be sterically stabilized [121] or charge-stabilized. In the former case, the pattern can be prepared by a different chemical coating while in the latter the surface pattern is dictated by the inhomogeneous surface charge density [122, 123, 100]. Another experimental system to observe structure formation near interfaces are magnetic bubble arrays with periodic line pinning [124]. While much experience has been accumulated in how to prepare the substrate in order to realize a prescribed mask, a more systematic theoretical understanding of possible decoration structures as induced by an underlying sticky periodic pattern is missing. In this chapter we investigate this problem for a periodic stripe pattern within a simple model calculation including both attractive and repulsive effective interparticle interactions. In equilibrium, we discover a wealth of possible stable decoration lattices. Hence although the substrate pattern is relatively simple, the decoration can be fascinatingly complex so that a wide range of decoration structures can be generated in a controlled and simple way. Even for a single stripe, periodic decoration structures as buckled alternating superlattices with a unit cell involving a large triangle of particles and finite slices of a triangular bulk lattice may become stable. For a periodic stripe-pattern, there are even more stable decoration lattices, involving triangular, quadratic, rhombic, kite-like and sheared honeycomb lattices.

The chapter is organized as follows: We describe the model in Sec.4.3.1 and outline our theory in Sec.4.2. Results are presented in Sec.4.3.2, and we conclude in Sec.4.5.

## 2.2 The Model

We consider a periodically stripe-patterned smooth surface, shown schematically in Fig.2.1. The width of the sticky stripes is $d$, while the distance between neighboring stripes is $b$, so that the structure is periodic in a direction perpendicular to the stripes with periodicity length $b+d$. This patterned surface is exposed to a suspension of spherical colloidal particles with hard-core diameter $\sigma$ aggregating onto the pattern. An aggregated sphere exhibits a point contact with the substrate gaining a potential energy $-\epsilon < 0$, provided the contact point is inside a sticky stripe. We assume strongly attractive substrates, such that $\epsilon$ is much larger than the thermal energy $k_BT$. Aggregation on the inter-stripe regions is neglected. Aggregation occurs from a dilute bulk solution of colloids. Here, we do not discuss the dynamics of aggregation or deposition [125], but rather focus on the equilibrium structure present after relaxation of the adsorption process. Typical pair potentials $V(r)$ as a function of separation distance $r$ between colloids have an inner hard core and a short-ranged tail. By addition of non-adsorbing polymers or salt ions to the bulk solution, both attractive or

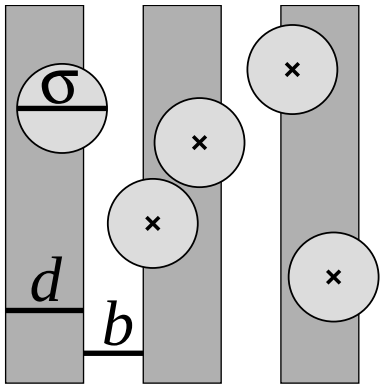


**Figure 2.1:** Model of hard spheres of diameter $\sigma$ on an attractive stripe pattern (dark gray) of width $d$ and inter-stripe distance $b$. The sphere centers (crosses) are constrained to lie inside the stripes.

repulsive tails can be realized [126]. For simplicity, we use a square-well/square-shoulder potential

$$V(r) = \begin{cases} \infty & \text{for} \quad r < \sigma \\ v_0 & \text{for} \quad \sigma \le r < \sigma(1+\delta) \\ 0 & \text{else} \end{cases} \tag{2.1}$$

with a small positive (reduced) range $\delta$. Depending on the sign of $v_0$, the tail is either repulsive ($v_0 > 0$) or attractive ($v_0 < 0$). Thermodynamics of this system in bulk has been studied in detail, see e.g. [127, 128, 129, 130] and references therein. Here, we expose the model to an inhomogeneous surface, and restrict ourselves to zero temperature, i.e. to the classical ground state [131]. Let $A$ be the area of the surface, $N$ be the number of adsorbed particles, $\rho = N/A$ denote the (two-dimensional) number density, and $\eta = \pi\rho\sigma^2/4$ the corresponding area fraction. The whole system is characterized by four reduced parameters, namely the reduced width $d/\sigma$ of the attractive stripe, the reduced interstripe width $b/\sigma$, the range of the potential $\delta$, and the ratio $v_0/\epsilon$ of colloid-colloid to substrate-colloid interaction.

## 2.3 Theory

For zero temperature the energetically most favorable configurations of the adsorbate will be attained. Technically, we need to minimize the total potential energy $U$ per area $A$. One may decompose $u \equiv U/A = u_1 + u_2$, where $u_1$ stems from substrate-particle attraction, and $u_2$ from particle-particle interactions. These contributions are

$$u_1 = -\epsilon\rho, \tag{2.2}$$

$$u_2 = A^{-1} \sum_{i=1}^{N} \sum_{j=i+1}^{N} V(|\vec{r}^{(i)} - \vec{r}^{(j)}|), \tag{2.3}$$

where $\vec{r}^{(i)}$ denote (two-dimensional) particle positions on the surface. It will prove useful to rewrite $u_2$ in terms of the *kissing numbers* $k^{(i)}$ (of particle $i$), that equal the number of touching spheres (i.e. $|\vec{r}^{(i)} - \vec{r}^{(j)}| = \sigma$) for particle $i$. If we assume absence of hard core overlap, and all particle separations $r$ being either at contact ($r = \sigma$), or outside the range of interaction ($r > \sigma(1+\delta)$), we can write

$$u_2 = \frac{v_0}{2A} \sum_{i=1}^{N} k_i \equiv v_0 \rho k/2, \tag{2.4}$$

where $k = N^{-1} \sum_{i=1}^{N} k^{(i)}$ is the (over system) averaged kissing number. Note that $u_1$ favors optimal packing of spheres, while $u_2$ couples to the number of sphere contacts. Decisive for phase behavior is the competition between optimization of packing and kissing, where the ratio $v_0/\epsilon$ is a control parameter. In practice, we start with different candidate lattices for the colloids, calculate $u$ for each one in order to find the optimal lattice that minimizes $u$. The choice of candidates is motivated by mathematical packing and includes rhombic, square, triangular, kite and other structures involving superlattices. We disregard the disordered fluid phase, as temperature is zero. We have not considered non-periodic structures as quasicrystals [132], that are expected to be unfavorable for a one-component colloidal system, but could become relevant for binary and ternary mixtures. A similar zero-temperature calculation on structured substrates can be found in Ref. [131], for quadratic substrate patterns and Lennard Jones interparticle interactions. We further remark that similar crystalline lattice structures were obtained in Ref. [133] for a different physical system, namely flux lattices in layered superconductors. In contrast to the short-range interactions employed in the present study, the interaction between flux lines is long-ranged.

## 2.4 Results

### 2.4.1 Single stripe

For $b/\sigma > 1+\delta$, the spheres adsorbed on neighboring stripes are decoupled and the problem reduces to that of adsorption onto a single stripe. For simplicity, we let $\delta \to 0$ and $v_0 \leq 0$, so that we deal with sticky hard spheres. Geometrical considerations as well as numerically checking other structures let us restrict the actually realized candidates to two $n$-layered crystals, namely i) triangular lattices ($n\Delta$), and ii) *supertriangle* structures ($n\mathcal{S}$), see Fig.2.2 for illustrations. $n\Delta$ is a portion of the triangular (bulk) lattice. The $n\mathcal{S}$ crystal consists of a buckled superlattice of alternating close-packed triangles.

The relevant properties of both candidates are the following. For $n$ close-packed layers on a stripe of width $d$, we find

$$\rho_\Delta = \frac{n}{d\sigma}, \tag{2.5}$$

$$\rho_\mathcal{S} = \frac{n(n+1)}{d\sigma[(n-1)+2\cos\alpha]}, \tag{2.6}$$

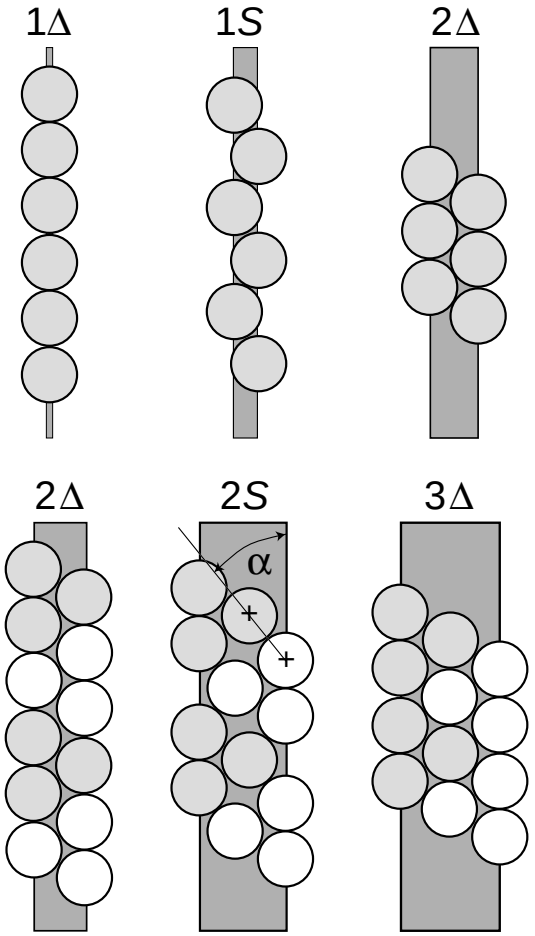


**Figure 2.2:** Crystal structures $n\Delta$ and $n\mathcal{S}$ of hard spheres sticking to a single stripe of width $d$ for $n = 1, 2, 3$. The stripe width $d$ increases from left to right. $\alpha \in [0, \pi/3)$ is the mismatch angle between adjacent supertriangles. Spheres building equilateral (super)triangles are shaded to guide the eye. For larger $d$ the sequence continues in an analogous way.

where $\alpha \in [0, \pi/3)$ is the mismatch angle between adjacent supertriangles, see Fig.2.2. For close-packed states, $\alpha$ is related to $d$ via

$$\alpha(d) = \arcsin(d - \sqrt{3}(n-1)/2). \tag{2.7}$$

Note that for $\alpha = 0$ (no mismatch), $n\Delta$ coincides with $n\mathcal{S}$, and trivially $\rho_\Delta = \rho_\mathcal{S}$. These configurations define the close-packed area fraction $\eta_{cp}$ plotted in Fig.2.3 a) as a function of stripe width $d$. For the average kissing number, we obtain via counting of sphere contacts

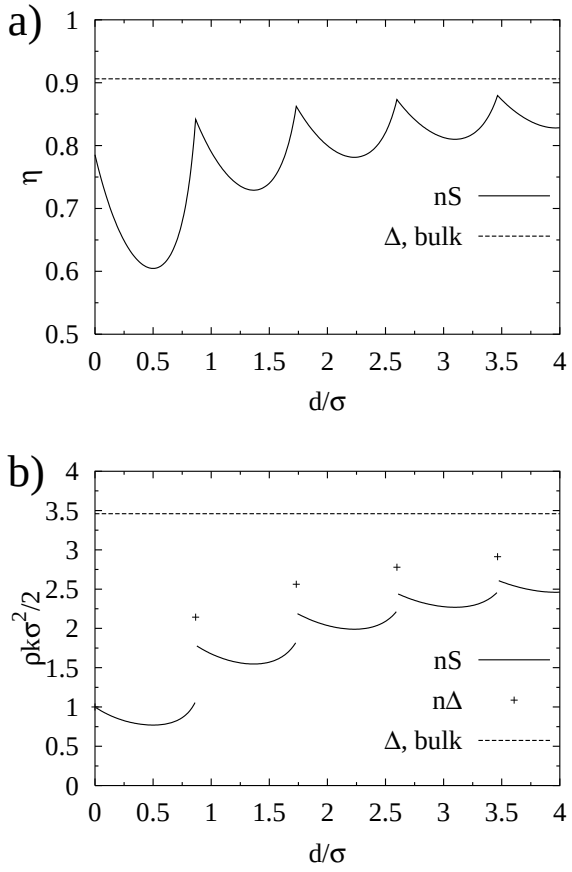


**Figure 2.3:** Relevant densities for close-packed hard spheres of diameter $\sigma$ on a stripe of width $d$ as a function of $d/\sigma$ for $n\Delta$ (symbols) and $n\mathcal{S}$ (lines) structures, as well as for the bulk triangular lattice (dashed lines). a) Area packing fraction $\eta$. b) Kissing number density per area, $\rho\sigma^2 k/2$.

$$k_\Delta = 6 - \frac{4}{n}, \tag{2.8}$$

$$k_\mathcal{S} = 6 - \frac{8}{n+1}. \tag{2.9}$$

Although in the limit $\alpha \to 0$ the structures themselves become identical, $k_\mathcal{S}$ does not approach $k_\Delta$ smoothly, but jumps at $\alpha = 0$. Relevant for the potential energy (Eq.2.4) is not the kissing number alone, but $\rho k/2$, that is plotted in Fig.2.3b as a function of stripe width $d$.

In the limit $v_0 \to -\infty$, maximal kissing *per area* determines the equilibrium structure, as the dominant contribution $\rho k/2$ (Eq.2.4) to the energy $u$ is to be maximized. Quite surprisingly, in each interval $n\sqrt{3}\sigma/2 < d < (n+1)\sqrt{3}\sigma/2$, a transition $n\Delta \to n\mathcal{S}$ exists, that is located at $d/\sigma = (n-1)\sqrt{3}/2 + \sqrt{1-[(2-n^{-1})/(3-2n^{-1})]^2}$, where large $k$ and low $\rho$ in $n\Delta$ are outperformed by low $k$ and high $\rho$ in $n\mathcal{S}$. Note that as $n \to \infty$, the transition persists, and the relative phase transition point $d/\sigma - (n-1)\sqrt{3}/2$ approaches

$\sqrt{5}/3 = 0.7454$.

Putting things together, we can turn to the full energetically driven phase diagram for arbitrary $|v_0/\epsilon|$. Asking first how additional layers $n \to n+1$ jump in, we find the simple answer: A transition $n\mathcal{S} \to (n+1)\Delta$ is located at $d = n(\sqrt{3}/2)\sigma$, *independent* of $v_0/\epsilon$. The $n\Delta \to n\mathcal{S}$ transition is less trivial. We obtain

$$d = (n-1)(\sqrt{3}/2)\sigma + \sigma\sqrt{1 - \left[\frac{(\epsilon/v_0) - 2 + n^{-1}}{(\epsilon/v_0) - 3 + 2n^{-1}}\right]^2}. \tag{2.10}$$

In the limiting cases, for $v_0/\epsilon = 0$, we recover the close-packing structure of discs between lines, and for $v_0/\epsilon \to -\infty$ the structure with maximal number of kisses. Eq. (2.10) interpolates smoothly between these limits.

The resulting phase diagram is shown in Fig.2.4 as a function of $d$ and $\exp(v_0/\epsilon)$. We

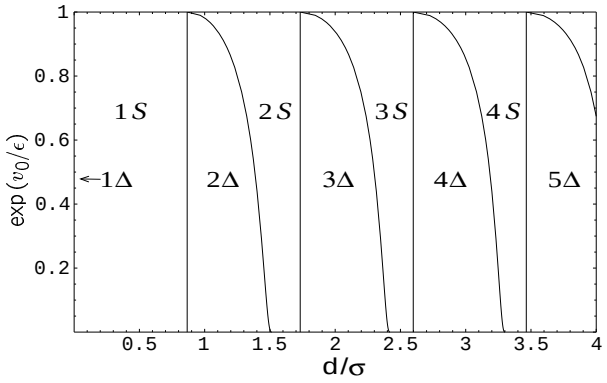


**Figure 2.4:** Phase diagram for sticky hard spheres adsorbed on a single sticky stripe as a function of reduced stripe width $d/\sigma$, and the (exponentiated) ratio $v_0/\epsilon$ of interparticle versus substrate potential. Lines are phase boundaries between $n\Delta$ and $n\mathcal{S}$ structures. The $1\Delta$ phase is a vertical line at $d/\sigma = 0$.

restrict ourselves to $n \leq 4$; the succession of $n\mathcal{S}$ and $n\Delta$ continues for larger $d$. In the limit of broad stripes ($d \to \infty$) and infinitely many layers ($n \to \infty$), we consider $d-(n-1)(\sqrt{3}/2)\sigma$, that maps $d/\sigma$ onto the $[0,1]$ interval, and obtain the universal ($n$-independent) result

$$d - (n-1)(\sqrt{3}/2)\sigma \to \sigma\sqrt{\frac{5 - 2(\epsilon/v_0)}{[(\epsilon/v_0) - 3]^2}}. \tag{2.11}$$

Narrow stripes with $0 < d < (\sqrt{3}/2)\sigma$ constitute a special case, because of dominance of a single phase $1\mathcal{S}$ ($1\Delta$ is squeezed to a vertical line at $d = 0$.) The reason for this behavior is that $1\Delta$ and $1\mathcal{S}$ possess equal kissing numbers. This is in contrast to $n > 1$, where $k_\Delta > k_\mathcal{S}$.

Two remarks are in order: First, the supertriangular phases $n\mathcal{S}$ are the two-dimensional analoga of three-dimensional prism phases [134] found for hard spheres confined between parallel hard plates. A similar cascade of phases has been found there, although this is

interrupted by other additional phases such as a rhombic structure [135, 136]. Second, in contrast to the bulk problem [137, 138], we are not aware of a strict mathematical proof for close-packed configurations, nor of any other numerical investigation of the packing problem of discs between lines. Other confining geometries such as the square [139, 140, 141], triangles [142, 143] and the circle [144, 145, 146] have been treated in a rigorous way.

### 2.4.2 Coupled Stripes

For $b/\sigma < 1 + \delta$, particles on adjacent stripes interact. We limit ourselves to the hard sphere case, $\delta = 0$, and hence deal with a packing problem. To break possible degeneracy of close-packed states, we consider $v_0/\epsilon \to 0^-$, favoring sphere contacts.

#### Triangular Lattice

We focus on the close-packed triangular lattice, of which is known that there is no denser structure in bulk. If we succeed to identify patterns that are compatible (all lattice sites lie on sticky stripes) with the triangular lattice, we have *proved* that there is no denser decoration lattice. The task is to determine the $(b, d)$ regimes in that the triangular lattice is geometrically possible. Let the lattice sites of a triangular lattice be

$$\vec{A}(j,k) = j\vec{a}_1 + k\vec{a}_2,\ j,k = 0, \pm 1, \pm 2, \ldots, \tag{2.12}$$

where $\vec{a}_1 = (\sigma, 0), \vec{a}_2 = (\sigma/2, \sqrt{3}\sigma/2)$ are basis vectors. In the following, we imagine the lattice to be fixed on the surface and attempt to determine those stripe patterns that are compatible with the particle lattice. For given $b, d$, the pattern is determined by the orientation along the stripes. This orientation may be expressed as $\vec{A}(j,k)/|\vec{A}(j,k)|$, with suitably chosen values for $j, k$. In order to find stripe patterns that fit the lattice, we calculate the distance $\xi(j,k)$ between adjacent lattice lines (the analoga to lattice *planes* in 3d), that are parallel to $\vec{A}(j,k)/|\vec{A}(j,k)|$. To this end, we introduce a vector $\vec{B}(j,k)$, that is orthogonal to $\vec{A}(j,k)/|\vec{A}(j,k)|$, as

$$\vec{B}(j,k) = -(j+2k)\vec{a}_1 + (2j+k)\vec{a}_2. \tag{2.13}$$

Projection of $(-1/k)\vec{a}_1$ onto $\vec{B}$ gives the lattice line distance

$$\xi(j,k) \;=\; -\frac{\vec{a}_1 \cdot \vec{B}}{k|\vec{B}|} = \frac{\sqrt{3}\sigma/2}{\sqrt{j^2+jk+k^2}}. \tag{2.14}$$

Upon varying $j$ and $k$, the argument $j^2+jk+k^2$ generates a (seemingly irregular when sorted) sequence of integer numbers, namely $1, 3, 4, 7, 9, 12, 13, 16, 19, 21, 25, 27, 28, 31, 36, 37, 39, 43, 48, 49, \ldots$. Expression (2.14) gives the lattice line distance for an orientation of lattice lines (parallel to the stripes) defined by $j, k$. Assuming that $b+d$ and the lattice structure $\xi(j,k)$ have the same periodicity, a triangular lattice fits, whenever the stripe width $d$ (with the

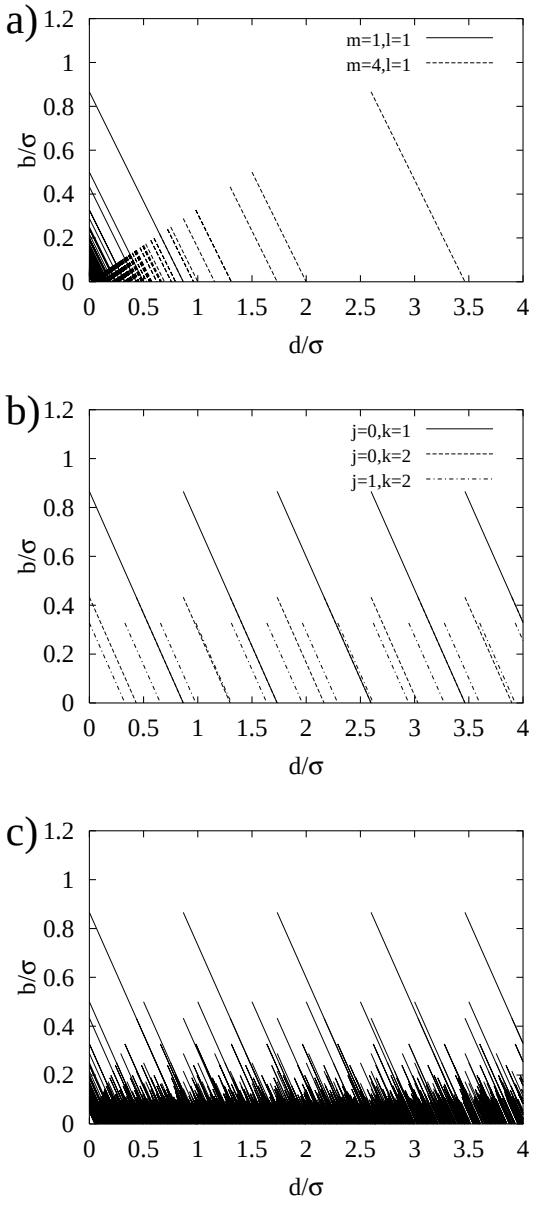


**Figure 2.5:** Regions of stability of the triangular lattice (lines). a) $m, l$ kept constant (as indicated), and $j, k$ varied. a) $i, j$ kept constant (as indicated), and $m, l$ varied. c) full range of $j, k, m, l$ (relevant for the scale of the plot).

stripe orientation given by $\vec{A}(j,k)/|\vec{A}(j,k)|$) and the interstripe distance $b$ have periodicity $\xi(j,k),\ j,k \in Z$,

$$b + d = \xi(j,k). \tag{2.15}$$

This introduces a linear relationship between stripe width $d$ and interstripe distance $b$. In the $b,d$-plane, lines joining $(\xi,0)$ and $(0,\xi)$ indicate regions where the triangular lattice fits the stripe pattern. For smaller values of $\xi$, these lines get increasingly dense and finally

converge into the origin.

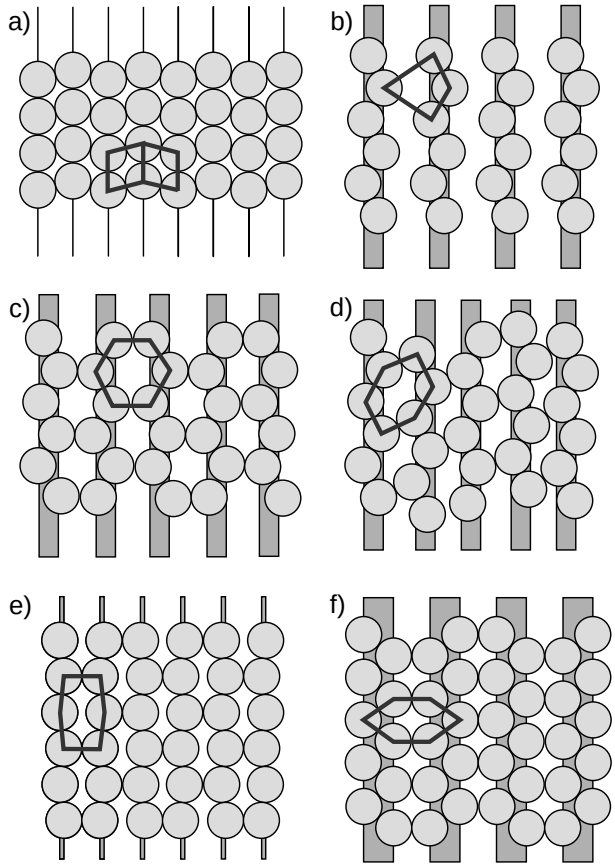


**Figure 2.6:** Crystal structures for $d/\sigma < \sqrt{3}/2$. a) Alternating rhombic for $d = 0$ and $\sqrt{3}/2 < b/\sigma < 1$; in b)-d) the situation is shown for $0 < d/\sigma < \sqrt{3}/2$ for decreasing values of the inter-stripe width $b/\sigma$: b) $1\mathcal{S}$ structures on decoupled stripes giving rise to kite-structures in a periodic stripe arrangement; c) honeycomb (1HC); d) sheared honeycomb (sheared 1HC); e) and f): squeezed 1HC for $b/\sigma = 1$, with $d/\sigma < 0.5$ and $d/\sigma > 0.5$ respectively. Solid lines indicate unit cells.

The assumption of $b+d$-periodicity is not mandatory. Rather we could let the structure be periodic after $m$ lattice spacings $\xi(j,k)$, and after $l$ stripe spacings $(b+d)$. This relation reads

$$b + d = \frac{m}{l}\xi(j,k), \tag{2.16}$$

where $m$ and $l$ must be indivisible integers, in order to avoid redundancies. The periodicity brings about a set of inequalities to be satisfied, expressing the condition that no sphere may lie outside a stripe,

$$i\xi(j,k) \leq j(b+d) \quad \vee \quad i\xi(j,k) \geq j(b+d) + b, \tag{2.17}$$

that is to be fulfilled for all $i, j$. Solving this leads to the relation

$$(m-1)b \leq d. \tag{2.18}$$

If we assume equality and use Eq.(2.16), we can solve for the minimal stripe width $d_{\min}$ and

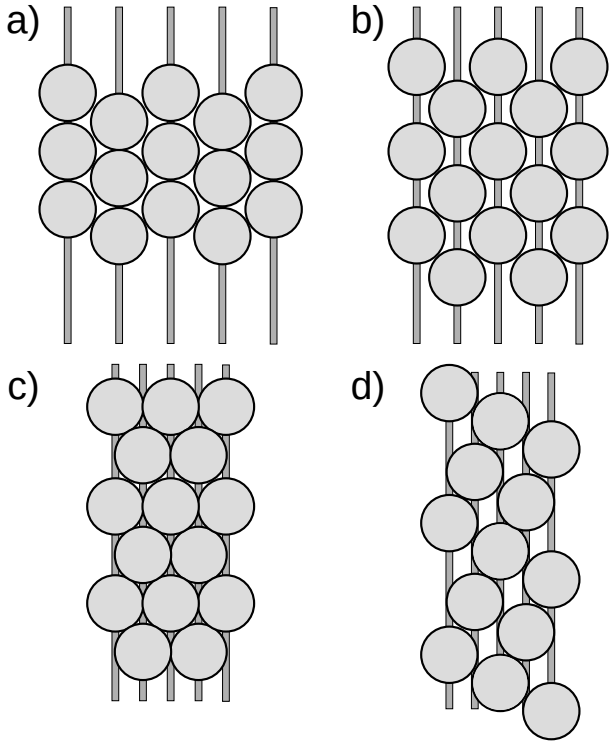


**Figure 2.7:** Crystal structures for infinitely thin stripes $d/\sigma = 0$ and decreasing values of $b/\sigma$: a) hexagonal lattice ($b/\sigma = \sqrt{3}/2$); b) centered rectangular ($0.5 < b/\sigma < \sqrt{3}/2$); c) hexagonal lattice ($b/\sigma = 0.5$); d) centered rectangular ($b/\sigma < 0.5$).

simultaneous maximal interstripe distance $b_{\max}$. These are

$$b_{\max} = \frac{1}{l}\xi(j,k), \tag{2.19}$$

$$d_{\min} = \frac{(m-1)}{l}\xi(j,k), \tag{2.20}$$

and fulfill the relation

$$(m-1)b_{\max} = d_{\min}. \tag{2.21}$$

Hence the triangular regimes are lines from $(0,\xi)$ to $(b_{\max}, d_{\min})$. The above case (lines from $(0,\xi)$ to $(\xi,0)$) is recovered for $m = l = 1$. For each combination of $m$ and $l$ we thus get a one-dimensional regime, where the triangular lattice fits. Variation of $j$ and $k$, at fixed $m$ and $l$, then gives additional lines, shifted on the $d$-axis with their length being reduced. This is illustrated in Fig. 2.5 a), where $j$ and $k$ are varied with $m = 1$ and $l = 1$ fixed (solid

lines) as well as $m = 4$ and $l = 4$ fixed (dashed lines). The shift of the lines is according to Eq.(2.21), their upper endpoints lying on a line defined by Eq.(2.20), whose slope changes with $m$. In Fig.2.5 b), the lattice line distances $\xi(j,k)$ are fixed via $j = 0, k = 1$ (solid lines), $j = 0, k = 2$ (dotted lines) and $j = 1, k = 2$ (dash-dotted lines), while $m$ and $l$ are varied. Fig.2.5 b) illustrates that $(j,k)$ for a given combination of $(m,l)$ determine the height and position of one line, with other combinations of $(m,l)$ produce replicas that are shifted on the $d$-axis. Fig.2.5 c) covers the full range (relevant for the scale of the plot) of values $j, k, m, l$. Note how the lines get denser for $b \to 0$, and ultimately approach stripe-free bulk packing. Although we cannot prove that the triangular lattice does *not* fit any other parts in the phase diagram, we find that quite likely.

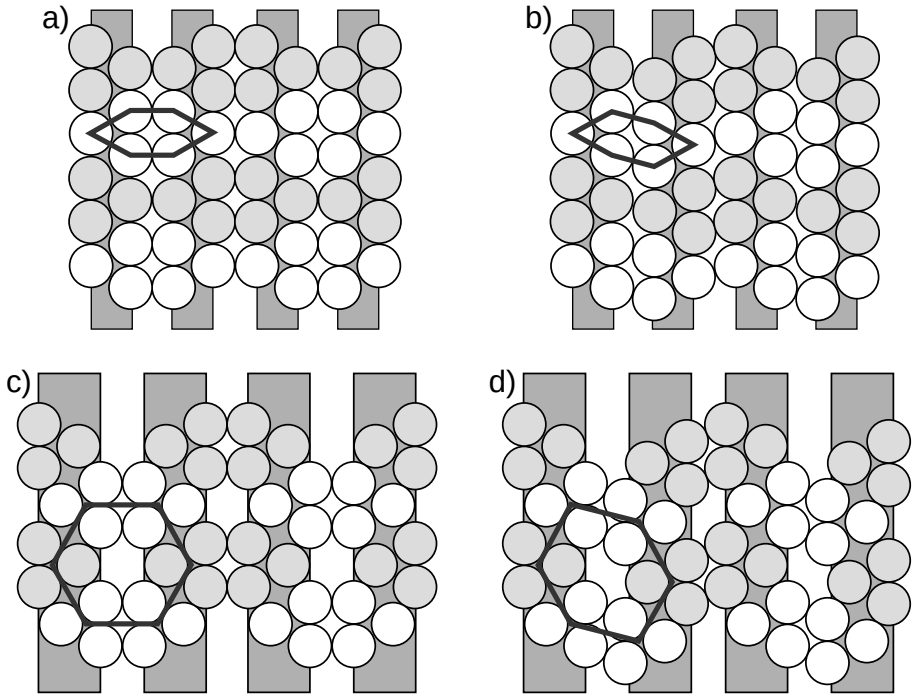


**Figure 2.8:** Crystal structures for $\sqrt{3}/2 \leq d/\sigma < \sqrt{3}$ and $b/\sigma \leq 1$: a) 2Δ-Square hybrid; b) sheared 2Δ-Square hybrid; c) 2-honeycomb structure (2HC); d) sheared 2-honeycomb (sheared 2HC). Spheres building equilateral triangles are shaded to guide the eye. Solid lines indicate unit cells.

The geometrical features of the regimes are visually quite striking, and may be unexpected from the outset. It is however known, that competition of length scales may induce fractal structures [147]. One simple tool to analyze these is box-counting [148]. In a two dimensional situation, one covers the structure under consideration with a rectangular mesh with mesh width $W$, and counts the number $B$ of boxes that touch (or are completely inside) the structure. This is performed successive times on smaller length scales $W$. For a fractal, a scaling law $B \propto W^{-\gamma}$ holds, where the dimension $\gamma$ is not an integer. We have carried out

such an analysis, and could confirm quite well power law scaling with a non-integer exponent. A precise determination of $\gamma$, however, turned out to be subtle. We have restricted ourselves to a physically reasonable lower cutoff $W > 10^{-3}\sigma$. For $m = l = 1$, we obtain a $\gamma = 1.5$. Superimposing "fence" patterns by varying $m, l$ over a broad range of values changes the dimension to $\gamma = 1.6$. Such an increase seems reasonable, as apparently, the structure gets denser. We leave a more thorough investigation to possible future research.

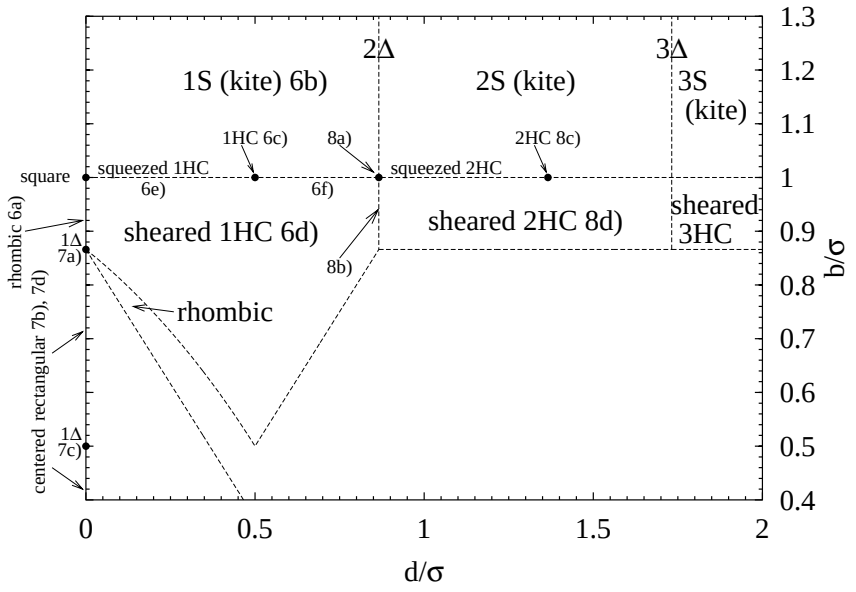


**Figure 2.9:** Phase Diagram of attractive hard spheres in a periodic arrangement of sticky stripes with stripe width $d$ and inter-stripe separation $b$. Dashed lines indicate two-phase coexistence. Various crystals are stable, as displayed in Figs. 2.6-2.8.

### More General Cases

We will approach the general case by considering interacting stripes that are itself densely packed. Results are known for $b/\sigma > 1$, periodic arrangement of the stripes will however give rise to special lattices. For $b/\sigma = 1$, the spheres from different stripes can touch and the stable phase is determined by the equilibrium structure on the stripes, together with the degeneracy breaking condition $v_0/\epsilon \to 0^-$. We thus get *quadratic* ordering in the interstripe region. A pure quadratic lattice is stable only in one point: $b/\sigma = d$ and $d = 0$. For lower $b$ and $d = 0$ it gets distorted to a lattice of alternating rhombi, as illustrated in Fig. 2.6 a). For $d < \sqrt{3}\sigma/2$ the situation is sketched in Figs. 2.6 b)-d) for decreasing values of $b$. Fig. 2.6 b) shows $1\mathcal{S}$ structures on decoupled stripes forming kite-structures in a periodic

stripe arrangement. The kite structure of Fig. 2.6 b), however, is degenerated with respect to an arbitrary relative shift of two single stripe patterns. Upon approach and coupling of the stripes a honeycomb (HC) in Fig. 2.6 c), and eventually a sheared honeycomb (sHC), shown in Fig. 2.6 d), emerge. For still smaller $b$, we expect another alternating rhombic phase, as shown in Fig.2.6 a), but with finite $d > 0$, to be stable.

For infinitely thin stripes, the situation for decreasing inter-stripe distances $b$ is sketched in Fig. 2.7. A sequence of triangular lattices and centered rectangular lattices arises. Similar structures were observed in recent experiments [116, 120].

For large $d > \sqrt{3}\sigma/2$, a squeezed honeycomb structure (Fig.2.8a) that can also be sheared (Fig.2.8b) appears. More complex crystal unit cells involving two supertriangular honeycomb structures, both sheared (Fig.2.8c) and unsheared (Fig.2.8d) occur for even larger $d$.

The resulting phase diagram of possible decoration lattices as a function of $b/\sigma$ and $d/\sigma$ is depicted in Fig.2.9. While for $b/\sigma > 1$ supertriangles are stable (compare Fig.2.4), a cascade of sheared honeycomb phases consisting of supertriangles occurs for $b/\sigma < 1$ and increasing $d$. Along coexistence lines (dashed lines in Fig.2.9), these sheared supertriangle honeycomb phases degenerate into different special cases: square lattice ($d/\sigma = 0, b/\sigma = 0$), unsheared honeycomb, squeezed honeycomb (see Fig.2.6 e) and f)) and alternating rhombic.

We combine the main results of this investigation with the regions of stability of the undistorted triangular lattice (Sec.2.4.2), and display the whole phase diagram of possible decoration lattices as a function of $b/\sigma$ and $d/\sigma$ in Fig.2.10. The states between the lines of stability of the triangular lattice are unexplored in our study. We leave those to future work.

Figs.2.9, 2.10 prove that even though our model is relatively simple, competition of different length scales leads to quite different stable decoration lattice structures. On the basis of Figs.2.9, 2.10 one can tailor the attractive stripe pattern in order to produce a given decoration lattice. This is of direct importance for further crystal growth on top of the decoration lattice used as a template. One can expect [103] that quite exotic bulk crystalline structures can be aggregated on top of such a template [119]. This is of relevance for the construction of optical band-gap materials like photonic crystals [149].

## 2.5 Conclusion

In conclusion, we have systematically investigated and predicted decoration lattices composed of colloidal particles adsorbed on an attractive stripe-patterned substrate. Our results show, that due to a competition of various length scales, a wealth of different decoration lattices can be stable. This knowledge can be exploited to generate exotic lattice structures by a tailored surface pattern that could be of relevance for fabricating photonic crystals grown on such templates. Our work can be extended into several directions: first, other periodic patterns such as alternating triangular or chessboard patterns can be studied where even more complicated decoration lattices are expected. Second, the effect of finite tem-

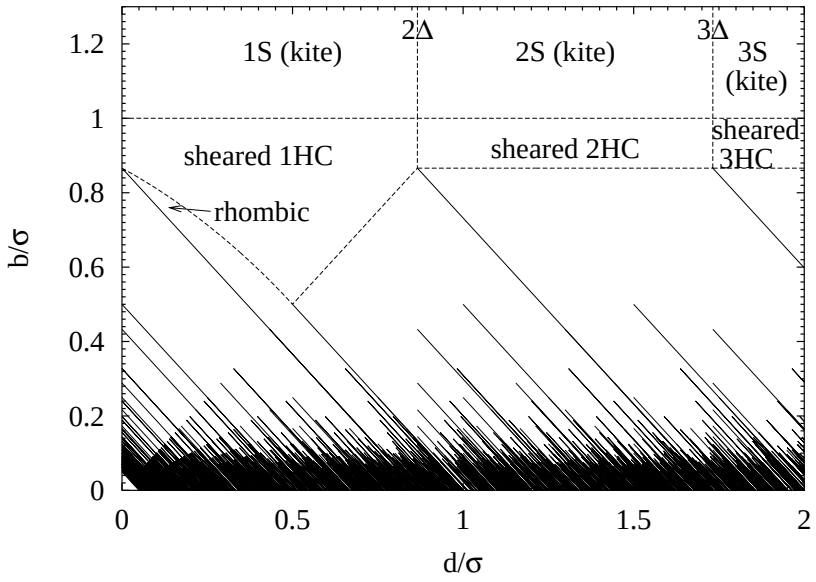


**Figure 2.10:** Phase Diagram of attractive hard spheres in a periodic arrangement of sticky stripes with stripe width $d$ and inter-stripe separation $b$. Solid lines indicate triangular regimes, dashed lines indicate two-phase coexistence.

perature and longer-ranged and more realistic particle-particle and particle-wall interaction should be investigated. Still we think that the main possibility of decoration lattices will be very similar to the results obtained for the more simplistic interactions. Also the non-equilibrium problem of particle deposition can produce even much richer non-equilibrium fractal and random-closed packing structures [150, 151, 152, 153] that have not been considered in the present equilibrium study. Finally, proving rigorously the different structures to be close-packed should be an interesting problem in mathematical geometry.

*In the two chapters to follow, we will now turn to a different method of investigation: Instead of calculating the $T = 0$ ground states of the systems under observation, we will take fluctuations into account as well. This will be done via Monte-Carlo simulations, first applied to a solution of star polymers in a gravitational field, then to an isolated dendrimer. Although the method of investigation changes, the next chapter is still linked to the present one by the fact that an external potential is essential for the formation of macroscopic order in the system, the external potential being the patterned substrate in the current chapter, and the gravitational potential in the upcoming chapter.*

# Chapter 3

# Sedimentation profiles of systems with reentrant melting behavior

*In bulk, star polymers are representative of a class of systems exhibiting reentrant melting behavior: Upon increasing the number density of particles in the solution, the system first undergoes a freezing transition, but then, upon further density increase, reenters the fluid regime. Submitted to gravitation, systems with reentrant melting in the bulk phase diagram display the same feature, now as a function of the height in the gravitational field: Going down in height, the system, being fluid at high elevations, first freezes and then melts again for even lower heights. This chapter is devoted to Monte Carlo simulations of star polymers in a gravitational field as model system for particles showing bulk reentrant melting. The simulation study is supplemented with scaling laws derived on the basis of a phenomenological theory as well as density functional theory.*

## 3.1 Introduction

Colloidal particles in a suspension under gravitational influence show spatial inhomogeneities due to the symmetry breaking induced by the gravitational field. The problem of sedimentation of particles in the presence of gravity has been of long scientific interest. The simplest approximation is the one of non-interacting particles, valid in the limit of dilute solutions. This approach leads to an exponential sedimentation density profile, which was observed by Perrin for a calculation of Boltzmann's constant in 1910 [154]. Taking into account particle interactions at higher concentrations will yield corrections to the exponential density profile. For very small gravitational strength, a local-density-approximation (LDA) of density functional theory (DFT) is justified [155, 156]. In this case, there is a one-to-one correspondence between the sedimentation density profile and the isothermal equation of state. This fact was exploited to extract the hard sphere equation of state experimentally by investigating sterically stabilized colloids [157]. Furthermore, within the LDA, a change in the height $z$ corresponds to a local change of the chemical potential $\mu$ of the bulk system. This im-

plies that, in the limit of small gravity, the phase behavior becomes visible as a function of height $z$, a feature which was also been exploited to estimate the hard sphere freezing transition [157]. Surprisingly, comparison with Monte-Carlo (MC) simulations show that the LDA is even reliable for relatively strong inhomogeneities or gravitational strengths [155]. This was further confirmed by comparing LDA against the exactly soluble hard rod model in one spatial dimension. While the LDA yields a monotonic decaying density profile $\rho(z)$, a layering shows up near the hard wall of the container bottom. Even crystallization can be induced by the bottom wall [158]. As shown recently [159], details of this surface-induced crystallization may be significantly influenced by a periodic wall pattern. Indeed, pure colloidal crystals can be grown from sedimentation on a patterned substrate [160, 161, 162]. In this case the gravitational field acts as an external force enforcing and accelerating heterogeneous nucleation and growth. Other fascinating phenomena in a gravitational field relevant for colloidal suspensions are phase transitions such as wetting [163], surface melting [164], as well as dynamical effects as shock like fronts [165], metastable phase formation [166], long-range velocity correlations [167], stratification [168], and crystal growth [169].

While the equilibrium sedimentation of hard sphere suspensions is well-understood [155, 158, 157, 170, 171], charged suspensions are much more subtle as they reveal an apparent mass which is smaller than the bare mass at least for intermediate heights [157, 172, 173, 174]. In this chapter, we study a third kind of effective interaction between colloids, namely a very soft core as realized for star polymer solutions [175]. The qualitative new feature of those solutions as compared to the traditional hard-sphere and Yukawa interactions is that their phase diagram exhibits a *reentrant melting behavior* for increasing density [176]. In fact, our analysis holds for any system with a reentrant melting behavior but we will mainly focus explicitly on star polymers. Star polymers consist of $f$ linear polymer arms attached to a central common core. The complete bulk phase diagram for star polymers in a good solvent was calculated in [176] and exhibits several unusual solid lattices as well as reentrant melting. As will be discussed in detail in the following sections, due to the reentrant melting behavior, unusual density profiles, featuring interesting effects, arise and a wealth of scaling laws can be established.

The chapter is organized as follows: In Sec. 3.2 results of computer simulations of a system of star polymers, interacting by means of an ultrasoft pair potential [8] are presented. In Sec. 3.3, we present a phenomenological theory giving account of the sedimentation profiles observed in the computer simulations. Scaling laws are put forth. Also in Sec. 3.3, density functional theory in a simplified hybrid weighted density approximation (HWDA) is used to reproduce density oscillations at the fluid-gas interface found in the simulation data. Concluding remarks are contained in Sec. 3.4.

## 3.2 Computer Simulation

We performed canonical MC computer simulations keeping particle number $N$, volume $V$, and temperature $T$ constant. We used a simulation box with squared periodic boundary conditions in $x$, $y$-direction and semi-infinite geometry in $z$-direction where the particles were confined only by the gravitational field for $z > 0$. The bottom wall at $z = 0$ was hard and interacting with the star polymers by means of an effective star polymer-wall potential which is derived from the effective star polymer-hard sphere interaction in the limit of a sphere with zero curvature. The calculation was performed in [177]. It is of the following form:

$$\begin{aligned} \beta V_{\mathrm{sw}}(z) &= \Lambda f^{3/2} \\ &\times \begin{cases} \infty & z < 0 \\ \xi_2 - \ln(\frac{2z}{\sigma}) - (\frac{4z^2}{\sigma^2} - 1)(\xi_1 - \frac{1}{2}) & z < \frac{\sigma}{2} \\ \xi_2(1 - \mathrm{erf}(2\kappa z))/(1 - \mathrm{erf}(\kappa\sigma)) & \text{else.} \end{cases} \end{aligned} \tag{3.1}$$

With $z$ we denote the distance from the center of one star polymer to the surface of the flat wall. $\sigma$ defines the so-called corona diameter of a star polymer, which is related to its diameter of gyration $\sigma_{\mathrm{g}}$ through $\sigma \simeq 0.66\sigma_{\mathrm{g}}$, see [177]. The constants are $\Lambda = 0.24$, $\kappa\sigma = 0.84$, $\xi_1 = 1/(1 + 2\kappa^2\sigma^2)$, $\xi_2 = \frac{\sqrt{\pi}\xi_1}{\kappa\sigma}\exp(\kappa^2\sigma^2)(1 - \mathrm{erf}(\kappa\sigma))$ and the inverse thermal energy $\beta = 1/k_BT$. We emphasize that the range of the star-wall interaction is of the order of one or two corona diameters, so that the behavior of the sedimentation profiles for larger distances is not influenced. The star polymer pair potential is ultrasoft and is described by the following equation [8]:

$$\beta V_{\mathrm{ss}}(r) = \frac{5}{18} f^{3/2} \begin{cases} -\ln(\frac{r}{\sigma}) + \frac{1}{1+\sqrt{f}/2} & r < \sigma \\ \frac{\sigma/r}{1+\sqrt{f}/2}\exp(-\frac{\sqrt{f}}{2\sigma}(r - \sigma)) & \text{else,} \end{cases} \tag{3.2}$$

with center-to-center distance $r$. Both interactions are purely entropic, hence they scale linearly with temperature. Previous work [176] showed that a system of star polymers interacting by means of the potential (3.2) possess a very rich and interesting bulk phase diagram, see Fig. 3.1, exhibiting reentrant melting and reentrant freezing transitions for arm numbers $f_{\mathrm{c}} \lesssim f \lesssim 54$, with the critical arm number $f_{\mathrm{c}} = 34$. As we will discuss in more detail below, it is the reentrant melting that makes this type of system appropriate for the analysis presented in this article. The suspending liquid is assumed to be incompressible. Furthermore we treat the solvent to be continuous, neglecting possible effects of the discreteness of the solvent particles. Given the size of the colloidal particles under observation, the star polymers, this is a reasonable assumption. In the simulation, the initial configuration of the system was chosen to be a body-centered cubic (bcc) solid to facilitate equilibration. Its lattice constant $a$ was determined from a bulk system with a packing fraction $\eta = \frac{\pi}{6}\rho\sigma^3 \simeq 0.5$

lying in the bcc-regime in the bulk phase diagram, see Fig. 3.1. The lateral box-dimensions were chosen to be multiples of the lattice constant $a$.

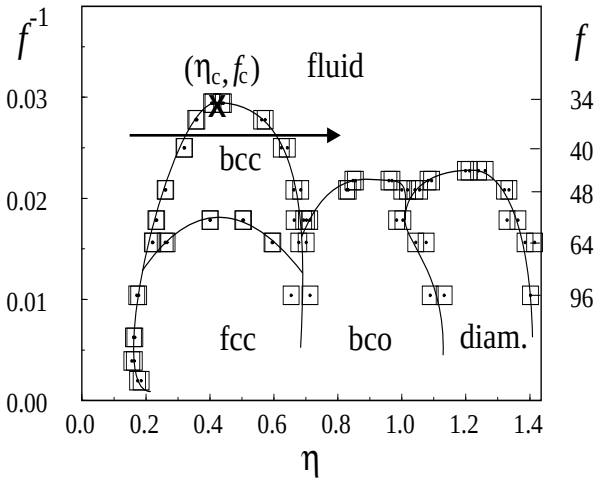


**Figure 3.1:** Bulk phase diagram of star polymers interacting with potential (3.2), calculated in [176]. Arm number $f$ is plotted versus packing fraction $\eta$. The squares indicate the phase boundaries; solid lines are guide to the eye. The black cross denotes the point with critical arm number $f_c \simeq 34$ and corresponding density $\eta_c \simeq 0.43$. The system is always fluid for arm numbers smaller than the critical arm number $f_c$ and shows reentrant melting behavior for arm numbers $f_c < f \lesssim 54$. The arrow indicates a path through the phase diagram that is equivalent with a change in the altitude $z$ within the LDA for small $\alpha$. The four observed solid phases are body-centered cubic (bcc), face-centered cubic (fcc), body-centered orthogonal (bco), and diamond (diam.).

The total number of particles was then fixed by prescribing a certain value of the thermodynamic variable $\tau$, giving the number density per unit surface. The density profile $\rho(z)$ is normalized as

$$\tau = \int_0^\infty \rho(z) dz. \tag{3.3}$$

$\tau\sigma^2$ is the number of particles piled up over the area $\sigma^2$ of the bottom wall. Typical system sizes were $N = 2000$ particles and the Monte Carlo runs were extended over $N_{\mathrm{MC}} \approx 500\,000$ cycles, each cycle comprising one trial move for each of the $N$ particles. Besides the aforementioned thermodynamic variable $\tau$, two further parameters characterize the state of the system: First, the arm number $f$ of the star polymers, being the number of polymer chains grafted on the central core. Second, the dimensionless gravitational strength (or Peclet number)

$$\alpha = \frac{mg\sigma}{k_B T}, \tag{3.4}$$

which describes the ratio of the potential energy gain to the thermal energy $k_B T$ for a particle of mass $m$, displaced by $\sigma$ in height in an external field with acceleration $g$. The

three parameters $f$, $\tau$ and $\alpha$ were varied over a broad range of values. The particles were moved by employing the standard Metropolis algorithm.

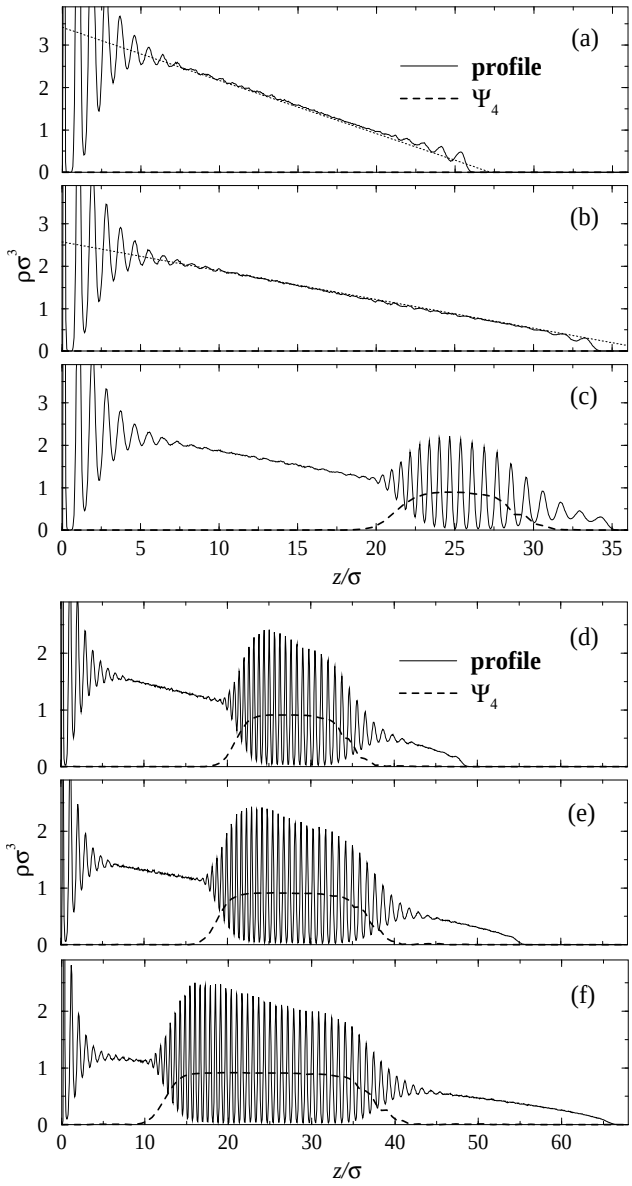


**Figure 3.2:** Sedimentation profiles of star polymers for an arm number $f = 39$ and a density $\tau\sigma^2 = 48.87$. The gravitational strength $\alpha$ is decreased from (a) to (f) with (a) $\alpha = 30.0$, (b) $\alpha = 17.0$, (c) $\alpha = 16.0$, (d) $\alpha = 8.0$, (e) $\alpha = 6.0$ and (f) $\alpha = 4.0$. In plots (c) - (f) the order parameter $\Psi_4$ is also shown (dashed line) using the same $y$-scale as the profiles. In (a) and (b) a straight line whose equation is derived within the LDA [see Eq. (3.12)] is superimposed on the plots (dotted line).

In Fig. 3.2 we show results for different gravitational strengths $\alpha$, while $\tau\sigma^2 = 48.87$ and

$f = 39$ are fixed. The $f = 39$ star polymer system displays reentrant melting in the fluid $\rightarrow$ bcc $\rightarrow$ fluid sequence, as seen along the arrow in Fig. 3.1. The gravitational field forces the local density $\sigma^3\rho(z)$ to take values that scan the range from $\sigma^3\rho(z) = 0$ up to high values, $\sigma^3\rho(z) \cong 3$. Thus, the local density 'crosses through' the range of the phase diagram where the system displays a bulk bcc phase. It it intuitively expected that the system will then feature a solid regime (for intermediate densities) intercalated between two fluid regimes, at low and high densities. We have found that this is indeed what happens but *provided* that the gravitational strength does *not* exceed a critical value $\alpha^*$, as we discuss below.

Let us start from the case where no solid phase appears. For $\alpha > \alpha^*$ [Figs. 3.2(a) and (b)], we obtain density profiles $\rho(z)$ that show three distinct features: First, there is layering on the wall due to packing effects, typically extending over several layers. As $z$ increases a fluid regime with density decaying as a linear function of altitude $z$ can be distinguished. At some height ($z \simeq 25\sigma$ in (a)) the density rapidly decays to zero. At this strong inhomogeneity oscillations in density with wavelength $\sigma$ can be distinguished in the sedimentation profile, which is smooth elsewhere in the linear regime. The linear dependence of the density profile on $z$, can be understood in terms of a local density functional mean-field theory, as will be shown in Sec. 3.3.2; the corresponding results from this theory are shown in Figs. 3.2(a) and (b) with dotted lines. The density oscillations observed in the simulations were reproducible in the framework of density functional theory using a simplified form of the HWDA, as will be discussed in further detail in Sec. 3.3.3.

By lowering the gravitational strength $\alpha$ further, a critical strength $\alpha^*$ in the range $16.0 < \alpha^* < 17.0$ is discovered. Below $\alpha^*$ the density profiles qualitatively change and exhibit a new feature. Strong density oscillations appear, a clear indication for a crystalline phase. They extend over 10 to 20 star diameters, equivalent to several crystalline layers. The length of the crystal grows, as $\alpha$ decreases. A typical simulation snapshot is shown in Fig. 3.3 next to the corresponding equilibrium density profile. Here, the well-ordered crystal phase in the middle of the simulation box ($20\sigma \lesssim z \lesssim 30\sigma$) is clearly visible.

As an additional check for crystalline order, we calculate the local order parameter, $\Psi_4$, that checks for fourfold symmetry in two dimensions around a given particle. It is defined by

$$\Psi_4(z) = \left| \left\langle \frac{1}{4N_{\rm l}} \sum_{j=1}^{N_{\rm l}} \sum_{<k>} e^{4i\phi_{jk}} \right\rangle \right|, \tag{3.5}$$

where the $k$-sum includes the four nearest neighbors of the given particle and the $j$-sum extends over $N_{\rm l}$ particles in the corresponding layer. A layer is defined by a slab of thickness $\delta \simeq 0.2\ a$, centered around the given particle at elevation $z$, which is motivated by the 'Lindemann melting rule', assuming a maximum particle displacement of approximately 10% around the equilibrium position in a possible crystal regime. The angular brackets indicate a canonical ensemble average. $\phi_{jk}$ is the polar angle of the interparticle distance vector with respect to a fixed reference frame. For ideal fourfold symmetry, i.e., for a particle contained in a bcc-solid layer, $\Psi_4 = 1$. Due to thermal motion, small defects of the perfect

crystalline symmetry arise and usually values of $\Psi_4 > 0.8$ [159] are taken to be conclusive evidence for a crystalline phase with fourfold-in-layer-symmetry. As can be seen in Figs. 3.2(c)-(f) our simulation data do indeed show values up to $\Psi_4 \approx 0.95$ in the region of the density profile $\rho(z)$ which we already identified to be solid due to the pronounced density oscillations.

Comparing the interval of the packing fraction in which crystallization occurs to the bulk phase diagram in Fig. 3.1, we may thus conclude that the intercalated solid regime is a manifestation of the reentrant melting in the bulk phase diagram, mapped onto the $z$-axis in a system under gravitational influence. The absence of freezing for strong gravitational fields ($\alpha > \alpha^*$) can now be at least qualitatively understood: for high values of $\alpha$, the density profiles grow too fast as $z$ approaches the wall, so that the mapping onto the $z$-axis results into a domain which is too narrow to sustain crystalline order. In fact, as we will show in detail in Sec. 3.3.2, a minimal, nonvanishing thickness of the crystalline layer is necessary so that the latter can be stably 'nested' between the two fluid phases.

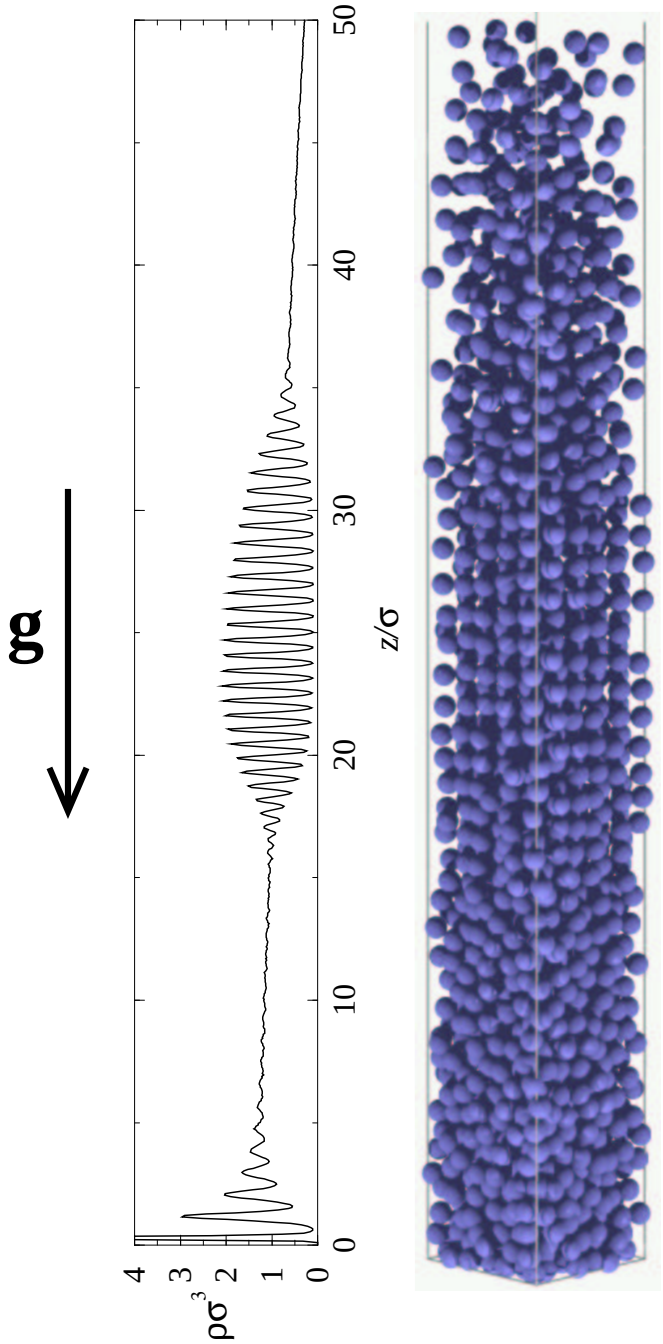


**Figure 3.3:** Snapshot from MC simulation (right) shown with the corresponding equilibrium density profile (left). The star polymers are rendered as spheres with diameter $\sigma$. The parameters are: $f = 39$, $\alpha = 5.0$, $\tau\sigma^2 = 42.1$.

## 3.3 Theory

### 3.3.1 Density Functional Theory in Local Density Approximation (LDA)

In order to predict scaling relations characterizing crystallization in sedimentation profiles of star polymer solution we apply density functional theory within the framework of the local density approximation (LDA). The latter is a reliable theoretical tool in cases where the density profile of the system varies slowly with $z$, so that it can be considered as staying essentially constant at length scales set by the microscopic natural length of the system ($\sigma$ in this case). As can be seen in Figs. 3.2(a) and (b), this is indeed the case if we discard the strong oscillations close to the wall (the layering effect). As the range of these oscillations is much shorter than the range of the density profile itself, the bulk of the free energy of the system resides in the smooth "ramp-like" part of the density profile and the use of the LDA is justified. Accordingly, we will omit the star-wall potential from our considerations in this subsection and consider only the effects of the external gravitational field $\Phi_{\rm ext}(z) = mgz$.

We work in the grand canonical ensemble and introduce the chemical potential $\mu$ and a variational grand potential per unit area, $\tilde{\Sigma}(T, \mu; [\rho(z)])$ which is a functional of the density profile. Introducing the ideal and excess per unit area contributions to the intrinsic Helmholtz free energy of the system, $F_{\rm id}[\rho(z)]$ and $F_{\rm ex}[\rho(z)]$ respectively, we find that in the LDA, the expression for $\tilde{\Sigma}(T, \mu; [\rho(z)])$ reads as:

$$\begin{aligned}\tilde{\Sigma}(T, \mu, [\rho(z)]) &= F_{\rm id}[\rho(z)] + F_{\rm ex}[\rho(z)] \\ &\quad + \int \mathrm{d}z \Phi_{\rm ext}(z)\rho(z) - \mu \int \mathrm{d}z \rho(z) \\ &= k_B T \int_0^\infty \mathrm{d}z \rho(z) \left[\ln(\rho(z)\lambda^3) - 1\right] \\ &+ \int_0^\infty \mathrm{d}z \left[f(\rho(z)) + (mgz - \mu)\rho(z)\right],\end{aligned} \tag{3.6}$$

where $\lambda = \sqrt{h^2/2\pi m k_B T}$ is the thermal de Broglie wavelength and $f(\rho(z))$ is the Helmholtz free energy per unit volume of the bulk fluid. The minimization of $\tilde{\Sigma}$ with respect to $\rho(z)$ yields the equilibrium profile $\rho_0(z)$; the value of the functional at equilibrium, $\tilde{\Sigma}(T, \mu, [\rho_0(z)])$ is then the Gibbs free energy per unit area, $\Sigma(T, \mu)$ of the system. Setting $\delta\tilde{\Sigma}(T, \mu, [\rho(z)])$ $/\delta\rho(z)|_{\rho_0(z)} = 0$ in Eq. (3.6), leads to:

$$k_B T \ln(\rho_0(z)\sigma^3) + f'(\rho_0(z)) = \mu' - mgz, \tag{3.7}$$

where $f'(x)$ denotes the derivative of $f(x)$ and $\mu' = \mu - 3\ln(\lambda/\sigma)$ is a shifted chemical potential.

Due to the ultrasoft character of the logarithmic-Yukawa star-star interaction $V_{\rm ss}(r)$, the star polymer system belongs to the class of *mean-field fluids* [178, 179, 180, 181, 182], for

which the excess free energy density is a quadratic function of $\rho$, namely:

$$f(\rho) \cong \frac{\rho^2}{2} 4\pi \int_0^\infty \mathrm{d}r\; r^2 V_{\mathrm{ss}}(r) =: \frac{\hat{V}_{\mathrm{ss}}(0)\rho^2}{2}, \tag{3.8}$$

with the Fourier transform $\hat{V}_{\mathrm{ss}}(k)$ of the pair potential. This property is valid for high density fluids provided their pair potential $V(r)$ is only slowly diverging at the origin and decays fast enough to zero as $r \to \infty$, so that it is integrable. For the more restrictive case of a nondiverging potential at $r = 0$, the stronger condition $c(r) = -\beta V(r)$ holds approximately [179, 180, 181, 182], with $c(r)$ denoting the direct correlation function of the fluid [70]. This gives again rise to Eq. (3.8) above through the compressibility equation of state [70].

Using the dimensionless variables $x \equiv z/\sigma$, $\bar{\rho}(x) \equiv \rho(z)\sigma^3$, $B \equiv \beta\hat{V}_{\mathrm{ss}}(0)/\sigma^3$ and $\bar{\mu} \equiv \beta\mu'$ and introducing Eq. (3.8) into Eq. (3.7), we obtain the equilibrium profile through the equation:

$$\ln(\bar{\rho}_0(x)) + B\bar{\rho}_0(x) = \bar{\mu} - \alpha x. \tag{3.9}$$

For star functionality $f = 39$ we obtain $B \cong 250$ and, for $f = 32$, $B \cong 204$ [see Eq. (3.2)]. Hence, the second term in the lhs of Eq. (3.9) above dominates over the logarithmic term for densities $\bar{\rho}(x) \gtrsim 0.10$. As almost the entire simulation density profile fulfills this condition, we finally omit the logarithmic term from Eq. (3.9) above and obtain thereby a *linear* density profile:

$$\bar{\rho}_0(x) = \begin{cases} 0 & \text{for } x < 0, \\ \frac{\bar{\mu}-\alpha x}{B} & \text{for } 0 < x < \bar{\mu}/\alpha, \\ 0 & \text{for } \bar{\mu}/\alpha < x. \end{cases} \tag{3.10}$$

The chemical potential $\bar{\mu}$ is now determined through the normalization condition $\int_0^{\bar{\mu}/\alpha} \mathrm{d}x \bar{\rho}_0(x) = \tau\sigma^2 \equiv \bar{\tau}$, yielding:

$$\bar{\mu} = \sqrt{2\alpha B\bar{\tau}}, \tag{3.11}$$

and from Eq. (3.10) the final expression for the density profile:

$$\bar{\rho}_0(x) = \begin{cases} 0 & \text{for } x < 0, \\ \sqrt{\frac{2\alpha\bar{\tau}}{B}} - \frac{\alpha}{B}x & \text{for } 0 < x < \sqrt{\frac{2B\bar{\tau}}{\alpha}}, \\ 0 & \text{for } \sqrt{\frac{2B\bar{\tau}}{\alpha}} < x. \end{cases} \tag{3.12}$$

The prediction (3.12) is compared against the MC simulation results in Figs. 3.2(a) and (b); theory and simulation are in excellent agreement. This linear dependence of the density profile on $z$ is the first scaling prediction we make for such systems. Moreover, by introducing Eq. (3.10) into Eq. (3.6), and once more ignoring the logarithmic term, we find that the Gibbs free energy per unit area $\Sigma(T, \mu)$ is a power-law of the chemical potential, namely:

$$\beta\sigma^2\Sigma(T, \bar{\mu}) = -\frac{\bar{\mu}^3}{6\alpha B}. \tag{3.13}$$

Accordingly, the Helmholtz free energy per unit area, $\beta\sigma^2 F(T,\bar{\tau}) = \beta\sigma^2\Sigma(T,\bar{\mu}) + \bar{\mu}\bar{\tau}$ obeys the scaling law:

$$\beta\sigma^2 F(T,\bar{\tau}) = \frac{2}{3}\sqrt{2\alpha B}\,\bar{\tau}^{3/2}. \tag{3.14}$$

The thermodynamic relation $\bar{\mu} = \partial(\beta\sigma^2 F)/\partial\bar{\tau}$ returns Eq. (3.11).

We now examine whether the density oscillations occurring at high $z$-elevations, which are clearly visible in Figs. 3.2(a), (b), can be obtained in the framework of the full LDA, with the logarithmic term included, Eq. (3.9). Though the latter is an implicit equation for $\bar{\rho}(x)$, we do not need to solve it in order to answer the question at hand. The key observation is that Eq. (3.9) delivers an explicit functional form for the *inverse* function:

$$x(\bar{\rho}) = -\alpha^{-1}(\ln\bar{\rho} + B\bar{\rho} - \bar{\mu}). \tag{3.15}$$

If the LDA profile displayed oscillations, then $\bar{\rho}(x)$ would go through various maxima and minima and there should be several points $x_{\rm m}$ where the derivative $\bar{\rho}'(x_{\rm m})$ would vanish, with the implication that the derivative of the inverse function, $x'(\bar{\rho}_{\rm m})$, would *diverge* at the corresponding density values $\bar{\rho}_{\rm m}$. From Eq. (3.15) above, we obtain $x'(\bar{\rho}) = -\alpha^{-1}(\bar{\rho}^{-1}+B) < 0$ for all $0 < \bar{\rho} < \infty$. The only divergence of $x'(\bar{\rho})$ occurs for the trivial limit $\bar{\rho} \to 0$ and corresponds to the exponential decay $\bar{\rho}(x) \propto e^{-\alpha x}$, valid for high elevations. The LDA is incapable to reproduce this effect, a feat that, in fact, could have been anticipated: these oscillations occur at length scales $\sigma$, whereas the LDA is applicable when the spatial inhomogeneity of the profile has a characteristic length much larger than the latter. In Sec. 3.3.3, we resort to a more powerful density functional approximation in order to reproduce this feature of the density profile.

### 3.3.2 Phenomenological Landau Theory

If one focuses close to the reentrant melting transition point, a phenomenological Landau-like approach can be adopted to explore further scaling predictions for the crystallization transition. We study the situation sketched in Fig. 3.4 of a crystalline sheet of width $l$ intervening between two fluid parts of the sedimentation profile. Let us define the excess grand canonical free energy per unit area, $\Sigma_{\rm ex}(l)$, in such a situation with respect to a situation where no crystallization takes place. This quantity is given by:

$$\Sigma_{\rm ex}(l) = \Sigma(l) - \Sigma(l=0), \tag{3.16}$$

with $\Sigma(l)$ being the grand canonical free energy per unit area when a solid of thickness $l$ is present. Evidently, $\Sigma(l=0)$ is the quantity given by Eq. (3.13) above.

The excess grand canonical free energy $\Sigma_{\rm ex}$ per unit area comprises of three parts:

1. The equilibrium surface tensions $\gamma_1$ and $\gamma_2$: These describe the additional free energy cost in creating the two solid-fluid interfaces at $z = z_1$ and $z = z_2$.

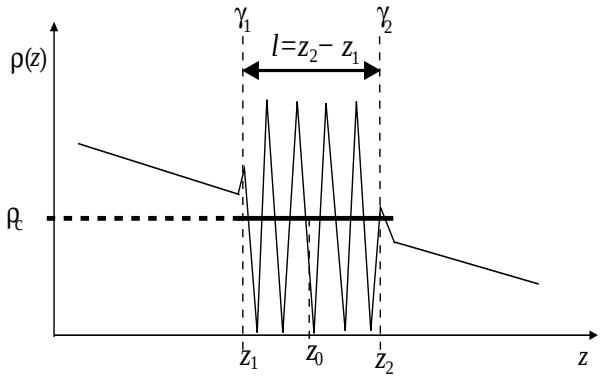


**Figure 3.4:** Sketch of the situation in which an intervening solid of width $l$ is nested between two fluids under the influence of a gravitational field.

2. A thermodynamic contribution which essentially depends on the arm number. If $f > f_c$ this contribution favors a solid sheet.

3. A free energy penalty due to an elastic distortion of the solid in the external field.

Hence:

$$\Sigma_{\rm ex} = \gamma_1 + \gamma_2 + \Sigma_{\rm TD} + \Sigma_{\rm elast}. \tag{3.17}$$

We point out that such a separation into interfacial and bulk terms is only possible when the thickness of the intervening solid sheet is large enough, so that the latter can be treated as a bulk solid. Though this requirement is evidently satisfied for small values of $\alpha$, the validity of our predictions is not limited to $a \ll 1$ values only; indeed, depending on the functionality $f$, $\alpha$ values of order as large as 10 can lead to intercalating solids comprising of as many as 20 crystalline sheets, and hence justifying their treatment as bulk phases. Let us discuss the different contributions in more detail:

The surface tension will mainly control the relative orientation of the solid with respect to the $z$-direction. One expects that a close-packed surface of the bcc-solid (i.e. a (100) orientation) will have smallest surface tension and will hence be the realized orientation. In fact, this is what we found in our simulation data presented in Figures 3.2 and 3.3. For hard-sphere fcc-solids the interfacial fluid-solid free energy has been calculated recently in equilibrium by computer simulation [183]. Its order of magnitude is

$$\gamma_i \approx \frac{k_B T}{\sigma^2}, \quad (i = 1, 2), \tag{3.18}$$

where $\sigma$ is a microscopic length scale.

The thermodynamic contribution could be calculated within the LDA with $f(\rho, T)$ taken from liquid state theories for the fluid and solid cell theory for the crystal. Here, we will simply focus on a Landau-type theory close to the reentrant melting point characterized

by a critical star number density $\rho_c = \frac{6}{\pi\sigma^3}\eta_c$ and the critical arm number $f_c$, see Fig. 3.1. Performing a Landau expansion and dropping the temperature dependence one gets

$$\begin{aligned} f_s(\rho) &= f_s(\rho_c) + A_s(f_c - f) \\ &\quad + f_s'(\rho_c)(\rho - \rho_c) \\ &\quad + \frac{1}{2} f_s''(\rho_c)(\rho - \rho_c)^2 + \dots \,. \end{aligned} \tag{3.19}$$

Here, $f_s(\rho)$ is the free energy per unit volume of the solid phase and $A_s$ is a constant governing the first leading term in an expansion around $f = f_c$. Likewise in the fluid phase one has

$$\begin{aligned} f_f(\rho) &= f_f(\rho_c) + A_f(f_c - f) \\ &\quad + f_f'(\rho_c)(\rho - \rho_c) \\ &\quad + \frac{1}{2} f_f''(\rho_c)(\rho - \rho_c)^2 + \dots \,, \end{aligned} \tag{3.20}$$

with $f_s(\rho_c) = f_f(\rho_c)$, $f_s'(\rho_c) = f_f'(\rho_c)$, but $f_s''(\rho_c) > f_f''(\rho_c)$ in general. Performing the inversion of $f(\rho)$ in order to get the density profile leads to a piecewise linear profile for the averaged density with two density jumps at $z = z_1$ and $z = z_2$, as determined by the Maxwell construction, see Fig. 3.4.

$$\rho(z) = \begin{cases} \frac{\mu - f_s'(\rho_c) - mgz}{f_s''(\rho_c)} + \rho_c & \text{for } z_1 < z < z_2 \\ \frac{\mu - f_f'(\rho_c) - mgz}{f_f''(\rho_c)} + \rho_c & \text{else.} \end{cases} \tag{3.21}$$

Consequently, by inserting this into the free energy function one gets

$$\Sigma_{TD} = -a(f - f_c)l + \left( \frac{1}{f_f''(\rho_c)} - \frac{1}{f_s''(\rho_c)} \right) \frac{m^2 g^2 l^3}{12}. \tag{3.22}$$

Note that $a > 0$ in order to stabilize the solid for $f > f_c$.

Third, the elastic part can be calculated by continuum elastic distortion theory of the solid. For a different situation of a solid in an external field this has been formulated by Gittes and Schick [184]. Following these ideas, we assume a $z$-independent lateral strain $\epsilon_\parallel$ but consider a $z$-dependent vertical strain $\epsilon_\perp$. By symmetry, $\epsilon_\parallel$ has to be zero for the crystal being stable at $z = z_0$, i.e., for the crystal at the reentrant melting point. Elasticity theory predicts for $\Sigma_{elast}$

$$\Sigma_{elast} \simeq \frac{1}{2} \int_{-\frac{l}{2}}^{\frac{l}{2}} \mathrm{d}z \, C \epsilon_\perp^2(z), \tag{3.23}$$

where $C > 0$ is related to the elastic constants of the solid. As

$$\epsilon_\perp \propto \rho - \rho_c \propto mgz, \tag{3.24}$$

we obtain

$$\Sigma_{elast} = C' l^3 m^2 g^2, \tag{3.25}$$

with another constant $C'$. Eq. (3.25) has a similar form as the second term of Eq. (3.22).

In summary, the total grand canonical excess free energy is

$$\Sigma_{\rm ex}(l) = -a(f - f_{\rm c})l + b\alpha^2 l^3 + \gamma_1 + \gamma_2, \tag{3.26}$$

where $a, b > 0$. Moreover we will use $\gamma = \gamma_1 + \gamma_2$ from now on. A first order phase transition takes place if the minimum of $\Sigma_{\rm ex}$ with respect to $l$ yields $\Sigma_{\rm ex} = 0$.

This determines the following resulting scaling relations:

1. The realized crystalline thickness $l$ as obtained by minimizing $\Sigma_{\rm ex}$ with respect to $l$ for fixed $\alpha$ and $f$ scales as
$$l \propto \frac{\sqrt{f - f_{\rm c}}}{\alpha}. \tag{3.27}$$

2. The phase transition to a crystalline sheet is first order. It happens beyond a critical $\alpha$-dependent arm number $f_{\rm crit}$ where
$$f_{\rm crit} - f_{\rm c} \propto \gamma^{2/3}\alpha^{2/3}, \tag{3.28}$$
with a scaling exponent of $\frac{2}{3}$.

3. The width $l_0$ corresponding to the transition scales as
$$l_0 \propto \gamma^{1/3}\alpha^{-2/3} \propto \frac{\gamma}{f - f_{\rm c}}. \tag{3.29}$$

The analysis presented here is general, the scaling predictions derived are valid for any reentrant melting behavior in equilibrium (e.g., laser-induced freezing [185, 186] or polydisperse systems [187]). Furthermore all these relations can, in principle, be checked by simulation. Relations (3.28) and (3.29), however, require high computational efforts. In order to check on scaling relation (3.27), we measured the crystal length $l$ in MC simulations varying $\alpha$ or $f$, while keeping the density $\tau$ fixed. The crystal length is determined by the range $\Delta z$, where the order parameter $\Psi_4(z)$ has values larger than 0.8. The results are plotted in Fig. 3.5, showing excellent agreement with the scaling predictions.

### 3.3.3 Weighted Density Approximation of the Density Functional

In order to verify the density oscillations close to the fluid-gas interface of the sedimentation profiles for large values of $\alpha$, we apply a simplified form of the HWDA (hybrid weighted density approximation). The full HWDA was constructed by Leidl and Wagner in [188]. Given an external field $\Phi_{\rm ext}(z)$ the free energy is a unique functional of the density profile $\rho(z)$. Thus, the excess free energy per unit surface in the HWDA framework is given by

$$\mathcal{F}_{\rm exc}[\rho] = \int_0^\infty \rho(z) f_0(\overline{\rho}(z)) {\rm d}z, \tag{3.30}$$

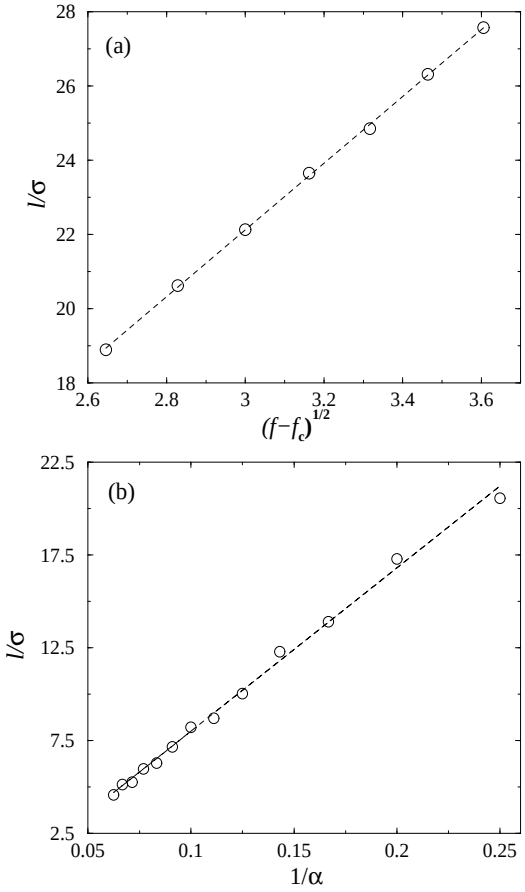


**Figure 3.5:** Verification of the scaling behavior theoretically predicted in Sec. 3.3.2 in Eq. (3.27), calculated by MC simulations. In (a) the crystal length $l$ is plotted versus $\sqrt{f - f_c}$, keeping $\alpha = 6.0$ fixed. In (b), $l$ is plotted versus $1/\alpha$ for a fixed arm number $f = 39$. The dashed lines are linear fits to the simulation results (circles).

where $f_0(\rho)$ denotes the excess free energy per particle of a homogeneous liquid of density $\rho$. The weighted density $\overline{\rho}(z)$ follows from a convolution with the weighting function $\omega(r;\rho)$

$$\overline{\rho}(z) = \int \rho(z')\omega(|\mathbf{r} - \mathbf{r}'|;\hat{\rho})\mathrm{d}\mathbf{r}' \tag{3.31}$$

with a global density $\hat{\rho}$. The weighting function $\omega(r;\rho)$ is fixed by a simple quadratic equation in Fourier space [188]:

$$\begin{aligned} 2f_0'(\rho_0)\tilde{\omega}(k;\rho_0) &+ \rho_0 f_0''(\rho_0)\tilde{\omega}^2(k;\rho_0) \\ &= -\beta^{-1}\tilde{c}^{(2)}(k;\rho_0) \end{aligned} \tag{3.32}$$

The primes denote differentiations with respect to the density $\rho$ and $\tilde{c}^{(2)}(k;\rho_0)$ is the Fourier transform of the direct correlation function of the homogeneous fluid. A unique solution of

$\tilde{\omega}(k;\rho_0)$ is determined by the normalization $\tilde{\omega}(k=0;\rho_0)=1$, also ensuring the compressibility rule to be satisfied. We have solved the homogeneous problem with Ornstein-Zernike fluid integral equations using the Rogers-Young closure [189]. Resulting correlation functions and structure factors are in very good agreement with MC simulations of the bulk system [178]. In difference to the complete HWDA, where the global density $\hat{\rho}$ is chosen to be a functional of $\rho(z)$, we keep $\hat{\rho}$ fixed. This simplification is sufficient to verify the observed oscillations, accompanied by the advantage that the numerical effort is enormously reduced. Best agreement with simulation results could be achieved when choosing the global density $\hat{\rho}$ to be of the order of the averaged density near the bottom wall $z=0$. The tails of the density profiles are nearly unaffected by the choice of $\hat{\rho}$. A similar approach is used in the SWDA [190] for an inhomogeneous fluid in contact with a bulk fluid of density $\rho_b$; there $\hat{\rho}$ was chosen to be $\rho_b$.

Applying the usual Euler-Lagrange minimization for the Helmholtz free energy per unit area $\mathcal{F}[\rho]$ with chemical potential $\mu$

$$\frac{\delta\mathcal{F}}{\delta\rho(z)} = \mu - \Phi_{\rm ext}(z), \tag{3.33}$$

and using $\Phi_{\rm ext}(z) = V_{\rm sw}(z) + \alpha z/\beta\sigma$, we obtain for the density profile $\rho(z)$

$$\rho(z) = \begin{cases} \xi \exp\{c^{(1)}(z;[\rho]) - \alpha z/\sigma - \beta V_{\rm sw}(z)\} & z > 0 \\ \\ 0 & \text{else.} \end{cases} \tag{3.34}$$

The fugacity $\xi$ is determined by the normalization condition $\xi = \tau / \int_0^\infty {\rm d}z \exp\{c^{(1)}(z;[\rho]) - \alpha z/\sigma - \beta V_{\rm sw}(z)\}$. $c^{(1)}(z;[\rho])$ is the one-particle correlation function:

$$\begin{aligned} -\beta^{-1} c^{(1)}(z;[\rho]) &= \frac{\delta\mathcal{F}_{\rm ex}[\rho]}{\delta\rho(z)} \\ &= f_0(\overline{\rho}(z)) \\ &\quad + \int {\rm d}z' \rho(z') f_0'(\overline{\rho}(z')) \omega(|z-z'|;\hat{\rho}). \end{aligned} \tag{3.35}$$

Equation (3.34) was solved for the profile by standard iterative techniques, see, e.g., Ref. [191]. The results for an arm number $f=32$, $\tau\sigma^2 = 21.8$ and three different values of $\alpha$ are shown in Fig. 3.6 together with MC simulation data. The global density $\hat{\rho}$ for all three profiles is fixed at $\hat{\rho}\sigma^3 = 1.8$. The DFT results are in very good agreement with the simulation profiles. In particular, the interface oscillations with wavelength $\sigma$ also occur in the DFT. For $\alpha = 10.0$, the lowest $\alpha$ that is shown, the profile is nearly indistinguishable from MC data far from the wall, while for increased $\alpha$, $\alpha = 20.0$ and $\alpha = 30.0$ the interface oscillations are underestimated in our DFT approach.

These oscillations are not a specific feature of the star polymers; we have also performed MC simulations using a repulsive Yukawa interaction of the form

$$V(r) \propto \exp(-\kappa r)/r, \tag{3.36}$$

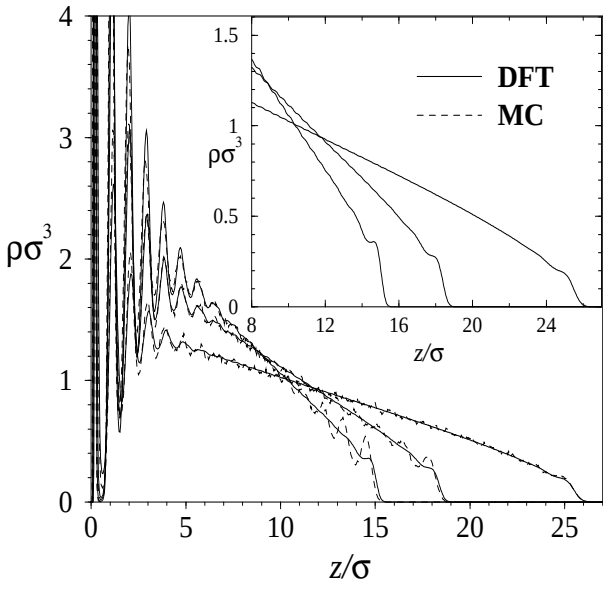


**Figure 3.6:** Density profiles $\rho(z)\sigma^3$ for three different values of $\alpha = 10.0, 20.0, 30.0$ and fixed arm number $f = 32$ and fixed density $\tau\sigma^2 = 21.8$ calculated with DFT (solid curves) compared to MC simulation results (dashed curves). The slope of the curves increases with increasing $\alpha$. The inset shows the bare DFT results for a better identification of the interface oscillations.

corresponding to the part of the star polymer pair potential (3.2) valid for distances $r \geq \sigma$. Here exactly the same behavior could be found at the tails of the density profiles. For hard sphere systems, on the other hand, no such density oscillations are present. This surprising fact might be attributed to the long ranged tail in the interaction potential.

## 3.4 Conclusions

Concluding, we have presented results for systems exhibiting reentrant melting in the bulk phase diagram, under gravitational influence. It was shown that a phase transition occurs when the gravitational strength $\alpha$ is varied: Below a critical $\alpha^*(f, \tau)$, intercalated crystallization occurs in the sedimentation profiles of the observed star-polymer solutions, whereas for $\alpha > \alpha^*(f, \tau)$ we find monotonic sedimentation profiles $\rho(z)$. In MC computer simulations scaling relations for the crystallization, predicted in the framework of a phenomenological theory, valid for all systems exhibiting reentrant melting in the bulk phase diagram, could be verified. Using density functional theory, density oscillations at the fluid-gas boundary, observed in the MC simulations, could be reproduced.

In principle, our results can be verified in surface-sensitive scattering experiments or real-space imaging methods for colloidal suspensions. Unlike non-monotonicities on the liquid

side of the gas-liquid equilibrium interface (see e.g. [192]), the density oscillations on top of the sedimentation profile are not affected by capillary wave fluctuations and may thus be verified in real samples. The intervening solid sheet should be signaled by a Bragg-like peak in surface reflection measurements. The strength of the gravitational parameter $\alpha$ can be tuned either by centrifugation or by grafting long polymer chains on massive colloidal particles, thus creating star-like micelles, whose phase diagram is identical to that of star polymers but which possess a much larger mass than the latter.

*In the following chapter we will employ the same method, Monte-Carlo simulations, to calculate the properties characterizing the structure of a single fourth generation dendrimer. We will thus not be dealing with the properties of an ensemble of mesoscopic particles any more, but rather step down one scale to elucidate the internal structure of one mesoscopic particle, which will lay the foundations for future work on the interactions and eventually the macroscopic ensemble properties of dendrimers.*

# Chapter 4

# Can dendrimers be viewed as compact colloids? A simulation study of the fluctuations of a dendrimer of fourth generation

*Dendrimers are polymeric macromolecules with a special, tree-like architecture. Another class of polymeric systems, star polymers, which are build up in a star-like architecture with $f$ polymer chains attached to a common core, are known to have the interesting feature that by tuning their arm number $f$, they interpolate between* hard *colloidal and* soft *polymeric behavior. Two observables characterize this change of behavior: The intrinsic fluctuations decrease and the pair interaction gets 'steeper'. Dendrimers too are known as hybrid model systems between soft polymer systems and hard colloids. Intuitively it is clear that the colloidal behavior can be amplified by increasing the generation number or by decreasing the length of the spacers within the dendrons. For dendrimers of a given generation number, however, the question is where the hybrid is to be found, towards which side of the colloid-polymer balance it is pending. To answer this question, we report in this chapter on work in which we resorted to Monte Carlo simulations of an isolated dendrimer, recording observables such as the radius of gyration, the radial density profile, the form factor and the monomer-monomer pair distribution function, as well as the fluctuations of the last two quantities. We start out with general considerations on the theory of form factors of colloidal macromolecular aggregates and then turn our attention to the analysis of the Monte Carlo simulation results in the light of the theoretical statements.*

## 4.1 Introduction

Dendrimers are synthetic macromolecules with a tree-like architecture [193, 194, 195, 196, 197]. The recent advances in developing well-controlled chemical techniques allow for the

synthesis of well-characterized branched macromolecules with a prescribed number of *branching bonds* $b$ at every connection point and *generation number* $g$. In Fig. 4.1 we show a scheme of a dendrimer with $b = 3$ and $g = 4$, which is conventionally termed G4-dendrimer. Dendrimers have attracted a lot of attention in the last few years, for a variety of reasons. First, their peculiar architecture establishes them as hybrid model systems between polymer chains and hard colloids, in terms of both the sphericity and compactness of their conformations and of the softness of their effective interactions. [198, 199, 200] This property, together with the possibility of tuning their conformations by changing $b$ and $g$ render them into macromolecules of fundamental interest for the soft matter scientists. Second, on the practical level, the possibility to influence the equilibrium monomer density distributions of dendrimers by controlling the pH or salinity of the aqueous solvent and to 'switch' thereby from 'dense shell' to 'dense core' configurations [201, 202] has established them as candidate carrier molecules for drug delivery. [203] The complexation of dendrimers with DNA macromolecules and the possibility of using them in order to engineer gene transfer is another exciting aspect that has attracted quite some attention recently. [204] Associated with the theoretical and simulational studies of dendrimers are small-angle experiments (employing either x-rays or neutrons) that provide information on the shape of isolated dendrimers in dilute solutions and the correlations between the same in concentrated ones.

In this work, we focus our attention on G4-dendrimers without charged groups, corresponding either to non-polar solvents or to aqueous ones in high pH-conditions. Despite original claims that these macromolecules assume typical configurations with a density profile that grows from the origin to their periphery [205] (the so-called 'dense-shell model'), a number of experimental, [206, 207, 208] simulational, [209, 210, 211, 212, 213, 214, 215, 216, 217] and theoretical studies [218] have demonstrated that the opposite is true: due to thermal fluctuations of the monomer groups, which are quite familiar from polymer science, a considerable degree of back-folding results and the density of the macromolecule is higher in the center than at the end (the 'dense-core model'). Hence, the apparent dense-shell picture seen in Fig. 4.1 is misleading if one interprets it literally: the chemical unities are *not* located at the positions shown in that drawing but they fluctuate and are allowed to explore the inner parts of the molecule as well.

Strong experimental evidence for this fact rests on small-angle neutron scattering (SANS) data that show a density profile that has a Gaussian shape in $q$-space. [200, 219] Treating then the dendrimers as *compact* objects, in which the monomer degrees of freedom are only very weakly fluctuating around their equilibrium positions in an uncorrelated manner, one obtains the density distribution as the inverse Fourier transform of the square root of the scattering intensity $I(q)$ (form factor), as we explain in detail below. The latter being given by a Gaussian function, it follows that the density distribution also has a Gaussian form. Though intuitively appealing, this procedure suffers from an inconsistency, in that the fluctuations of the monomers, which are responsible for the back-folding of the arms in the first place, are left out of the picture in the inversion of the SANS-data.

In this chapter, we report on monomer-resolved Monte Carlo (MC) simulations of a G4-dendrimer. Our work serves a double purpose: on the one hand, we propose a specific microscopic model of a dendrimer and we demonstrate by direct comparison with experimental data that, with the suitable choice of a single length scale, the measured scattering factor of the molecules can be very accurately reproduced. Thus, it represents a step in the microscopic modeling of these highly interesting macromolecules. On the other hand, based on the fact of this accurate description, we then put into test the validity of the inversion procedure mentioned in the preceding paragraph by examining in detail the correlations of the fluctuations of the monomers of a G4-dendrimer. A wealth of relevant quantities pertinent to the molecules have been calculated and compared to experimental data. The main finding of our analysis is that the monomer fluctuations are correlated at length scales that are typically not reachable by SANS-techniques, i.e., of the order of the monomer (or Kuhn) length. For the $q$-ranges accessible to SANS-experiments, excellent agreement between simulation and experiment is obtained and it is explicitly shown that the dense-core model maintains its validity.

The rest of the chapter is organized as follows: In Section 4.2 we present some basic facts about scattering from colloidal particles, implications of the possible internal fluctuations of the latter on the connection between form factors and density profiles, and the relation to experimental results. In Section 4.3, we describe our employed model for the dendrimer and the simulation method, and we present our results. In Section 4.4 we discuss these results in connection with previously employed mean-field-like approximations for dendrimers and with obtained experimental results. Finally, in Section 4.5 we summarize and conclude.

## 4.2 The form factor of colloidal macromolecular aggregates

The so-called scattering factor $\mathcal{S}(\mathbf{q})$ provides information about the spatial correlations of a system of interacting particles. [220] It comprises an extremely useful quantity for investigations of the spatial correlations in fluids, simple and complex, and also in inhomogeneous phases, such as crystalline solids. One of the great advantages of $\mathcal{S}(\mathbf{q})$ is that it can be on the one hand calculated theoretically, once the interparticle interactions are known, and on the other it is precisely the quantity measured in performing elastic scattering experiments using various probes, such as x-rays, neutrons or light. In this context, $\mathbf{q}$ is the scattering wavevector, equal to the difference between the wavevector of the outgoing radiation, $\mathbf{q}_{\text{out}}$, and that of the incoming radiation, $\mathbf{q}_{\text{in}}$, i.e., $\mathbf{q} = \mathbf{q}_{\text{out}} - \mathbf{q}_{\text{in}}$.

Let us consider, then, a collection of $N$ atoms with spatial coordinates $\{\mathbf{r}_1(t), \mathbf{r}_2(t), \ldots, \mathbf{r}_N(t)\}$, where we explicitly denote the time-dependence of the, generally fluctuating, particle coordinates. At this point, we make no differentiation as to whether these are the $N$ monomers of a polymer, the $N$ scattering units of a rigid colloid, or simply $N$ atoms of a simple fluid or solid: the discussion is quite general. The one-particle density operator $\hat{\rho}(\mathbf{x})$ of the system

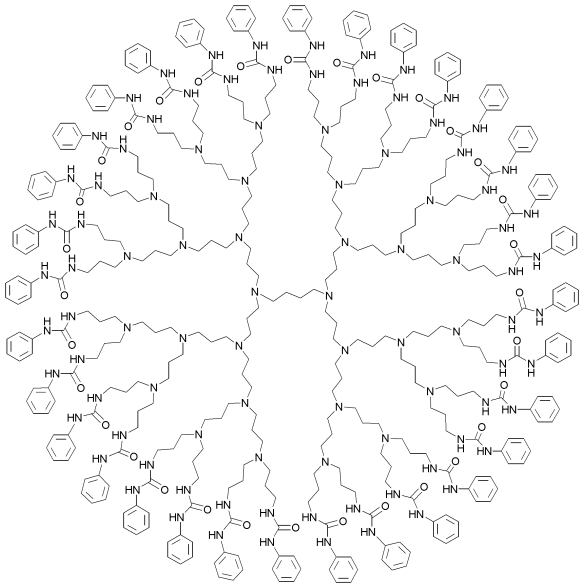

**Figure 4.1:** Scheme of the chemical structure of a dendrimer of fourth generation. This picture provides a demonstration of the chemistry and architecture of the dendrimer only and does not represent a true typical configuration of the monomer groups of the molecule in solution.

is defined as usual through the relation:

$$\hat{\rho}(\mathbf{x}) = \sum_{i=1}^{N} \delta(\mathbf{x} - \mathbf{r}_i(t)), \tag{4.1}$$

and the one-particle density $\rho(\mathbf{x})$ as the ensemble average of $\hat{\rho}(\mathbf{x})$ in equilibrium:

$$\rho(\mathbf{x}) = \langle \hat{\rho}(\mathbf{x}) \rangle. \tag{4.2}$$

A further useful quantity is the partially integrated density-density autocorrelation function $G(\mathbf{r})$ of the assembly, defined as [221]

$$\begin{aligned} G(\mathbf{r}) &= \frac{1}{N} \int \mathrm{d}^3 r' \langle \hat{\rho}(\mathbf{r} + \mathbf{r}') \hat{\rho}(\mathbf{r}') \rangle \\ &= \frac{1}{N} \left\langle \sum_{i=1}^{N} \sum_{j=1}^{N} \int \mathrm{d}^3 r' \delta(\mathbf{r} + \mathbf{r}' - \mathbf{r}_i) \delta(\mathbf{r}' - \mathbf{r}_j) \right\rangle \\ &= \frac{1}{N} \left\langle \sum_{i=1}^{N} \sum_{j=1}^{N} \delta(\mathbf{r} - \mathbf{r}_{ij}) \right\rangle, \end{aligned} \tag{4.3}$$

where $\mathbf{r}_{ij} = \mathbf{r}_i - \mathbf{r}_j$ and we have used Eq. (4.1). Thus, $G(\mathbf{r})$ is proportional to the probability of finding a pair of particles with their coordinates separated by the vector $\mathbf{r}$. Note that $\mathbf{r}$ is

a free vector, i.e., it is not associated with any particular coordinate system. It is also usual to separate the contributions in the double sum of Eq. (4.3) above from the terms with $i = j$ and to write

$$G(\mathbf{r}) = \delta(\mathbf{r}) + \frac{1}{N}\left\langle \sum_{i=1}^{N}\sum_{j\neq i}^{N} \delta(\mathbf{r} - \mathbf{r}_{ij}) \right\rangle . \tag{4.4}$$

When applied to an isotropic fluid, for example, the second term in the rhs above turns into $\rho g(r)$, with the average density $\rho$ of the fluid and the well-known radial distribution function $g(r)$. The whole function depends then only on the magnitude $r \equiv |\mathbf{r}|$ of the separation vector. [221]

Let us now introduce the Fourier transform (FT) of the one-particle density operator of Eq. (4.1), $\hat{\rho}_{\mathbf{q}}$, given by

$$\hat{\rho}_{\mathbf{q}} = \int \mathrm{d}^3\mathbf{x}\, \hat{\rho}(\mathbf{x}) \exp(-\mathrm{i}\mathbf{q}\cdot\mathbf{x}) = \sum_{i=1}^{N} \exp(-\mathrm{i}\mathbf{q}\cdot\mathbf{r}_i), \tag{4.5}$$

and its expectation value $\tilde{\rho}(\mathbf{q})$ through

$$\tilde{\rho}(\mathbf{q}) = \langle \hat{\rho}_{\mathbf{q}} \rangle. \tag{4.6}$$

The scattering factor $\mathcal{S}(\mathbf{q})$ can be defined as the FT of the correlation function $G(\mathbf{r})$:

$$\mathcal{S}(\mathbf{q}) = \int \mathrm{d}^3\mathbf{r}\, G(\mathbf{r}) \exp(-\mathrm{i}\mathbf{q}\cdot\mathbf{r}), \tag{4.7}$$

and use of Eqs. (4.3) and (4.5) leads to the equivalent expression: [222]

$$\mathcal{S}(\mathbf{q}) = \frac{1}{N}\langle \hat{\rho}_{\mathbf{q}}\hat{\rho}_{-\mathbf{q}} \rangle = \frac{1}{N}\left\langle \hat{\rho}_{\mathbf{q}}\hat{\rho}^{*}_{\mathbf{q}} \right\rangle , \tag{4.8}$$

with the asterisk denoting the complex conjugate. Alternatively, using Eq. (4.4), we obtain

$$\mathcal{S}(\mathbf{q}) = 1 + \frac{1}{N}\left\langle \sum_{i=1}^{N}\sum_{j\neq i}^{N} \exp[-\mathrm{i}\mathbf{q}\cdot(\mathbf{r}_i - \mathbf{r}_j)] \right\rangle . \tag{4.9}$$

Two well-known examples are provided by scattering from simple, isotropic fluids and perfect crystalline solids. In the former case, the scattering factor $\mathcal{S}(\mathbf{q})$ as defined above depends only on $q \equiv |\mathbf{q}|$ and is related to the well-known *structure factor* $S(q)$ of the fluid through

$$\mathcal{S}(q) = (2\pi)^3\rho\delta(\mathbf{q}) + S(q). \tag{4.10}$$

In the latter case, the result follows that $\mathcal{S}(\mathbf{q})$ is a sum of delta spikes at the vectors of the reciprocal lattice (Bragg scattering).

We now turn our attention to solutions of *complex* molecules, i.e., macromolecular aggregates of mesoscopic dimensions, such as colloids or polymers. When scattering from a dilute

solution of the same, the contribution to the scattering factor arising from interactions between the whole macromolecules can be ignored. Thus, the scattering experiment provides information about the spatial correlations between the constituent atoms (scattering centers) of the macromolecule, i.e., about the *internal* correlations in the colloidal aggregate. It is common to call the scattering factor $\mathcal{S}(\mathbf{q})$ associated with a single macromolecular object *form factor* [222, 223] and in what follows we denote it as $F(\mathbf{q})$.

We consider, then, a *single* mesoscopic particle consisting of $N$ atoms that scatter as point particles. Since only the differences $\mathbf{r}_{ij}$ of the position vectors appear in Eqs. (4.3) and (4.7), it is immaterial where the origin of the coordinates is positioned. Therefore, as we let the molecule diffuse into the solution (as it happens in real experiments) we can measure for every position and conformation the distances $\mathbf{r}_i$, $\mathbf{r}_j$ from the instantaneous center of mass of the dendrimer. This is convenient since it allows us immediately also to measure the density distribution around the center of mass, so this is the technique adopted in our simulations. Moreover, since in calculating $G(\mathbf{r})$ or $F(\mathbf{q})$ thermodynamic averages over all conformations are involved, (including averaging over all rotations), these two functions become dependent solely on $r$ and $q$, respectively: even if the instantaneous conformations of the macromolecule strongly depart from sphericity, the process of averaging restores spherical symmetry. This holds also in particular for the density distribution around the center of mass of the particle, Eq. (4.2), when all distances are measured with respect to this point.

As is clear from Eq. (4.7), the form factor $F(\mathbf{q})$ delivers information about *pair correlations* between the atoms. In some special cases, though, this information can be directly linked to the density distributions $\rho(r)$ around some 'pinning center' (emerging through a pinning potential that depends only on the distance of the particles to this central point) or the density around the center of mass, as we demonstrate below.

The first example is the case in which all particles are connected to a common center but they are otherwise independent from each other, i.e., there is no coupling between $\mathbf{r}_i$ and $\mathbf{r}_j$ for $i \neq j$ in the Hamiltonian of the system. Then, the expectation value in Eq. (4.9) factorizes into (setting now $\mathcal{S}(q) \to F(q)$):

$$\begin{aligned} F(q) &= 1 + \frac{1}{N}\left\langle \sum_{i=1}^{N} \exp(-\mathrm{i}\mathbf{q}\cdot\mathbf{r}_i) \right\rangle \left\langle \sum_{j\neq i}^{N} \exp(\mathrm{i}\mathbf{q}\cdot\mathbf{r}_j) \right\rangle \\ &\cong 1 + \frac{1}{N}\tilde{\rho}(q)\tilde{\rho}(-q) \\ &= 1 + \frac{1}{N}\tilde{\rho}^2(q), \end{aligned} \tag{4.11}$$

where, in the second line, we assumed that $N \gg 1$ so that the exclusion $j \neq i$ has minimal effects on calculating the function $\tilde{\rho}(-q)$ and in the third line we used the spherical symmetry of $\rho(r)$ around the pinning center in order to obtain $\tilde{\rho}(-q) = \tilde{\rho}(q)$.

The second example pertains to 'rigid mesoscopic particles'. [223] With this term, we mean that the position vectors $\{\mathbf{r}_1(t), \mathbf{r}_2(t), \ldots, \mathbf{r}_N(t)\}$ of the individual atoms fluctuate very weakly around their average positions and the latter can be taken as frozen degrees of freedom

in an excellent approximation. In this case, performing the averages $\langle \ldots \rangle$ in the various equations above is practically equivalent to calculating the sums or the integrals for this one, frozen configuration. Typical such particles are colloidal silica or PMMA hard spheres, or core-shell particles that can be treated as compact, rigid objects. To simplify things, we assume that the atoms are positioned in a configuration that possesses inversion symmetry around the particle's center of mass. By taking into consideration the weak fluctuations and/or by performing a coarse-graining procedure on length scales of a few Angstrom, we can thereby describe the object by a spherically symmetric one-particle density $\rho(r)$ around its center of mass. The suitable starting point is relation (4.8) together with Eq. (4.5). The coordinates of the scattering centers, $\mathbf{r}_i$, can now be considered as discrete sampling points that have been selected in order to approximate an integral by the sum given on the right-hand side of Eq. (4.5). Calling this integral $J(\mathbf{q})$, we have thus

$$J(\mathbf{q}) \approx \sum_{i=1}^{N} \exp(-\mathrm{i}\mathbf{q} \cdot \mathbf{r}_i). \tag{4.12}$$

Approximating the integral by the sum above is justified as long as the integrand varies slowly on the scale of $\Delta\mathbf{r}$, where $\Delta\mathbf{r}$ is the typical spacing between two neighboring points on the discrete grid $\{\mathbf{r}_k\}$, $k = 1, 2, \ldots, N$. In this dense-point limit, the centrosymmetric distribution of the set $\{\mathbf{r}_k\}$ implies that the sum will approximately depend only on the magnitude $q$ of the wavevector. Dropping then the ensemble averages, as discussed above, and using Eq. (4.8), we obtain for the form factor the expression

$$F(q) = \frac{1}{N} J^2(q), \tag{4.13}$$

under the condition $\mathbf{q} \cdot \Delta\mathbf{r} \ll 1$.

We examine now the connection of $J(q)$ with $\rho(r)$. If the coarse-grained density $\rho(r)$ is uniform within a sphere of radius $R$, then the points $\{\mathbf{r}_k\}$, $k = 1, 2, \ldots, N$ are uniformly distributed within this domain and the integral that the sum approximates is simply

$$\begin{aligned} J(q) &= \frac{3N}{4\pi R^3} \int \mathrm{d}^3 r \, \Theta(R - r) \exp(-\mathrm{i}\mathbf{q} \cdot \mathbf{r}) \\ &= \tilde{\rho}(q), \end{aligned} \tag{4.14}$$

with the Heaviside step function $\Theta(x)$. Eqs. (4.13) and (4.14) give then rise to the well-known form factor of hard spheres in the Rayleigh-Gans-Debye limit. [224] If now the density $\rho(r)$ has a smooth $r$-dependence, then the set of coordinates $\{\mathbf{r}_k\}$, $k = 1, 2, \ldots, N$ will be nonuniformly distributed and they can be thought of as random variables drawn from a probability density $p_{\mathbf{r}}(r) \propto \rho(r)$. Then, it is straightforward to show, by performing a change of variables and their distributions, that [11]

$$\begin{aligned} J(q) &= \int \mathrm{d}^3 r \, \rho(r) \exp(-\mathrm{i}\mathbf{q} \cdot \mathbf{r}) \\ &= \frac{4\pi}{q} \int_0^\infty \mathrm{d}r \, r\rho(r) \sin(qr) = \tilde{\rho}(q). \end{aligned} \tag{4.15}$$

Thus, for arbitrary density distributions $\rho(r)$ of spherosymmetric rigid objects, the result is obtained

$$F(q) = \frac{1}{N}\tilde{\rho}^2(q), \tag{4.16}$$

allowing us to relate the form factor to the square of the Fourier transform of the density distribution around the center of mass of the colloid. Associated with this equation is a relation between $G(r)$ and $\rho(r)$ that reads as

$$G(r) = \frac{1}{N}[\rho \otimes \rho](r), \tag{4.17}$$

with $[\rho \otimes \rho](r)$ denoting the autoconvolution of the density $\rho(r)$. We emphasize, however, that relation (4.16) holds as long as $\mathbf{q} \cdot \Delta\mathbf{r} \ll 1$ is satisfied, so that approximating a sum by an integral is justified. For high enough values of $q$, the form factor must tend to unity, as is clear from Eq. (4.9), whereas $F(q)$ given by Eq. (4.16) above tends to zero as $q \to \infty$.

## 4.3 Monte Carlo Simulations of an Isolated Dendrimer

From Eqs. (4.11) and (4.16), it is clear that the form factor can be utilized to obtain directly information about the density distributions only at two specific limiting cases: either when the correlations between the fluctuations of the particles vanish [Eq. (4.11)] or when the fluctuations themselves are very weak in the first place [Eq. (4.16)]. Though the second case is quite common when dealing with compact, 'hard' particles, things change in the case of 'polymeric colloids' that consist of polymer chains synthesized carefully in order to produce various architectures.

Polymer chains are a relevant example: the form factor of ideal (Gaussian) polymers is known to be given by the form [225] $F(q) = N f_{\mathrm{D}}(q^2 R_g^2)$, with the Debye function $f_{\mathrm{D}}(z) = 2\left(z - 1 + e^{-z}\right)/z^2$. In this case of strongly fluctuating monomers, relation (4.17) does not hold and hence a back transformation of $F(q)$ in real space only yields $G(r)$; it does not deliver information about $\rho(r)$. Increasing the 'stiffness' of the polymeric colloid can be achieved by constructing a star polymer [198, 220] through anchoring of $f$ chains on a common center. Star polymers are indeed hybrids between polymers and colloids. There, one distinguishes two mesoscopic length scales, the diameter of the outermost blob $\xi_{\max}$ and the radius of gyration $R_g$. For separations $\xi_{\max} \lesssim r \lesssim R_g$, a star polymer with large functionality $f$ appears compact and a relation of the form (4.17) approximately holds. [220] However, for $r < \xi_{\max}$, one encounters the typical pair correlations akin to those of isolated polymer chains, leading to the linear chain-like scaling $G(r) \sim r^{1/\nu - 3}$, with the Flory exponent $\nu \cong 0.6$ that characterizes self-avoiding random walks. Similar considerations have been put forward for the case of block copolymer micelles. [226] Therefore, the deviation of the pair correlation function from the 'rigid particle form', Eq. (4.17) can be used as a diagnostic tool for measuring the strength of the correlated fluctuations. Alternatively, the deviations of $F(q)$ from the form (4.16) provide an indication for the length scales at which these fluctuations are correlated.

Dendrimers represent a novel type of hybrid particles between soft polymers and hard colloids. Their effective interaction can be tuned by controlling the generation number and the length of the spacers within the dendrons. It is at the same time directly influenced by the monomer density distribution around the dendrimer's center. Therefore, it is important on the one hand to develop reliable microscopic models describing the isolated dendrimer's conformations and on the other hand to establish quantitative measures for the degree in which these conformations differ from those of rigid objects. This point is of central importance for a clear understanding of the information to be gained from scattering experiments. [206, 207] We investigated these questions by means of Monte Carlo simulations and we present our model below.

### 4.3.1 The Model and Simulation Details

To mimic the dendrimer whose chemical structure is schematically depicted in Fig. 4.1, our model-molecule has the same topology as the one shown there, whereby, however, the atomic groups are replaced by spherical beads that build up the dendrimers' dendrons. The beads represent thereby 'effective monomers' consisting of all units within one Kuhn segment grouped together. As we do not introduce any intrinsic stiffness in the model in the form of orientational bias of the interaction, the identification of the bead with the Kuhn segment is justified. To model the steric, excluded-volume interactions between Kuhn segments in good solvent conditions, we introduce a purely repulsive Lennard-Jones like potential, $V_0(r)$, acting between all beads, where $r$ denotes the separation between the bead centers. The interaction $V_0(r)$ is obtained by truncating the Lennard-Jones potential $V_{\mathrm{LJ}}(r)$ at the minimum position $r_{\min} = 2^{1/6}\sigma_{\mathrm{LJ}}$ and shifting it by the constant $V_{\mathrm{LJ}}(r_{\min})$ to get $V_0(r_{\min}) = 0$:

$$V_0(r) = \begin{cases} 4\epsilon\left[(\frac{\sigma_{\mathrm{LJ}}}{r})^{12} - (\frac{\sigma_{\mathrm{LJ}}}{r})^{6} + 0.25\right]; & r \leq 2^{1/6}\sigma_{\mathrm{LJ}} \\ 0; & r > 2^{1/6}\sigma_{\mathrm{LJ}}. \end{cases} \tag{4.18}$$

The energy scale is set by $\epsilon$, the length scale by the Lennard-Jones diameter $\sigma_{\mathrm{LJ}}$ of the beads. In addition to the repulsion present for all monomers, *neighboring* (connected) monomers along one dendron interact via the attractive finite-nonlinear-extensible-elastic (FENE) potential, [227] $V_{\mathrm{ch}}(r)$, which reads as

$$V_{\mathrm{ch}}(r) = \begin{cases} -15\epsilon(\frac{R_0}{\sigma_{\mathrm{LJ}}})^2 \ln\left[1 - (\frac{r}{R_0})^2\right]; & r \leq R_0 \\ \infty; & r > R_0. \end{cases} \tag{4.19}$$

The location of divergence in the FENE potential, $R_0$, determines the maximum bond length between two monomers and was fixed to the standard literature value of $R_0 = 1.5\sigma_{\mathrm{LJ}}$. The total potential, $V(r) = V_0(r) + V_{\mathrm{ch}}(r)$ then has a minimum at $r_* = 0.97\sigma_{\mathrm{LJ}}$, see Fig. 4.2. This way, it is guaranteed that occurrence of 'ghost chains' in the Monte Carlo moves is avoided. Finally, the temperature of the system is fixed at $T = 1.2\epsilon/k_B$. The microscopic identification of $\sigma_{\mathrm{LJ}}$ will then follow from comparison with experimental data.

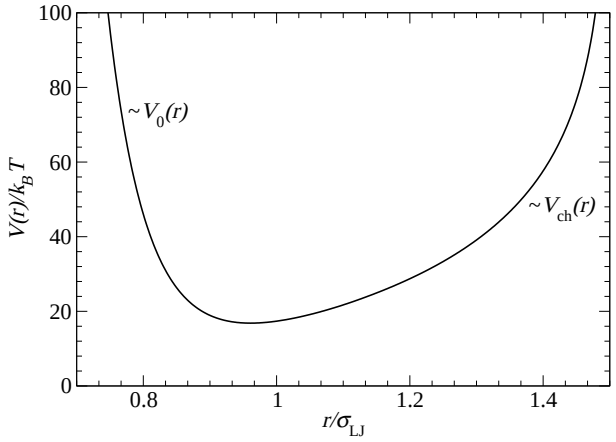


**Figure 4.2:** The total potential $V(r) = V_0(r) + V_{\rm ch}(r)$ acting between two adjacent beads of the dendrimer.

Canonical Monte-Carlo (MC) simulation techniques, making use of the Metropolis algorithm were employed in the present work. Typically, $N_{\rm MC} = 1 \times 10^7$ MC cycles were simulated, with one MC cycle being comprised of one trial move for each of the $N$ particles. Of the $N_{\rm MC}$ steps, 20% were used for equilibration. In the remaining MC cycles, $4 \times 10^5$ configurations were used to calculate statistical averages of the radial density distribution $\rho(r)$ of the dendrimer around its center of mass, the pair distribution function $G(r)$, the form factor $F(q)$, as well as its radius of gyration $R_g$.

### 4.3.2 Results

In order to assess the isolated dendrimer's equilibrium properties, we first record the radial density distribution function of the dendrimer's monomers with respect to the dendrimer's center of mass, $\mathbf{r}_{\rm CM}$, being defined as

$$\rho(r) = \left\langle \sum_{i=1}^{N} \delta(\mathbf{r} - \mathbf{r}_i) \right\rangle , \tag{4.20}$$

with $N$ being the number of monomers. Here, $\mathbf{r}$ and $\mathbf{r}_i$ are measured with respect to the dendrimer center of mass, $(\mathbf{r}, \mathbf{r}_i) = (\mathbf{r}' - \mathbf{r}_{\rm CM}, \mathbf{r}'_i - \mathbf{r}_{\rm CM})$, where $(\mathbf{r}', \mathbf{r}'_i)$ are the position vectors with respect to a fixed coordinate system and $\mathbf{r}_{\rm CM} = (1/N) \sum_{i=1}^{N} \mathbf{r}'_i$. As we expect the dendrimer to be spherically symmetric on average, it is justified to work with the spherosymmetric density distribution as introduced above. Moreover, in order to make a further connection with recently obtained, accurate SANS-results on end-monomer distributions, we also measured the quantities $\rho_{\rm g4}(r)$, $G_{\rm g4}(r)$ and $F_{\rm g4}(q)$ pertaining to particles of the last generation *only*, employing obvious notation. This result can therefore be directly compared to recent experimental data pertaining to the distribution of endgroups in a dendrimer. [208]

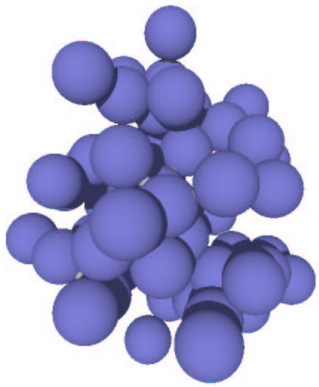

**Figure 4.3:** Simulation snapshot of a fourth generation dendrimer. The monomer beads are rendered as spheres of diameter $\sigma_{\mathrm{LJ}}$.

In Fig. 4.3 we show a snapshot of a fourth generation dendrimer from the MC simulation. It can be seen that there the deviations from sphericity are small and, in any case, much less pronounced than those seen in linear polymer chains with the same degree of polymerization $N$. Due to the choice of the interparticle potentials causing a stiff minimum at separations $r_* = 0.97\sigma_{\mathrm{LJ}}$ between adjacent beads, the latter attain configurations that are practically indistinguishable from those of tangent hard spheres of diameter $\sigma = r_*$. It can be seen that the connectivity of the monomers produces a compact object with a dense core; there is no sign of a dense shell configuration of the dendrimer in any of the typical snapshots we looked at.

The simulation results for the density $\rho(r)$ are shown in Fig. 4.4 and corroborate the dense core picture: the general trend is that the profile is decreasing as one moves away from the center. There is a pronounced peak at about $r/\sigma_{\mathrm{LJ}} = 0.4$, originating from the two beads comprising the zeroth generation of the dendrimer. Since the beads are practically indistinguishable in their behavior from tangent hard spheres of diameter $r_* \cong \sigma_{\mathrm{LJ}}$, the ideal position of the center of mass would be in the midpoint between the zeroth-generation bond and this would produce a peak in $\rho(r)$ at $r/\sigma_{\mathrm{LJ}} = 0.5$. The fact that this peak is located at the smaller value 0.4 is a clear indication that the center of mass of the dendrimer wanders around significantly, and that it often comes closer to the center of one the two beads of the zeroth generation. There is an alternative explanation regarding the position of this peak, namely: the zeroth generation bond length is shrunk due to the osmotic pressure exercised by the higher-generation monomers surrounding the zeroth-generation. However, this was ruled out by performing Monte Carlo simulations employing a different microscopic model: the beads were modeled as true hard spheres of diameter $\sigma$, connected by threads of maximum extension $\varepsilon\sigma$, with $\varepsilon = 0.05,\ 0.1$. Very similar results were obtained for the density profile and thus the shrinking scenario can be ruled out since hard spheres cannot be

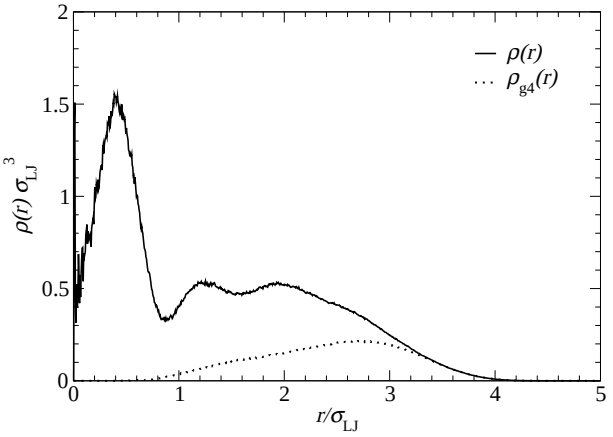


**Figure 4.4:** The radial density distribution with respect to the center of mass, $\rho(r)$, shown as a function of $r/\sigma_{\rm LJ}$, measured by including all monomers (full line), and by solely taking the last generation's monomers into account (dotted line).

found in separations smaller than their diameter. On the other hand, the strong similarity of the results obtained using the two different microscopic models leads to the conclusion that the details of the short-range steric repulsions do not matter: as in the case of linear polymer chains, the excluded volume effect dictates the main physics of the conformations of the macromolecules. A detailed account of the results from the bead-thread model for various generation numbers will be presented elsewhere. [228]

At larger distances, the second and third shell of the dendrimer are resolved as well, their peaks being, however, much less pronounced and indicating that the fluctuations of higher generations become broader. As a matter of fact, one can roughly discern a 'plateau' at the density profile, located between $\sigma_{\rm LJ}$ and $2\sigma_{\rm LJ}$. The extent of this 'flat' region grows as one increases the maximum generation number. Dendrimers represent a model polymeric system that features constant density profiles, $\rho_{\rm r} \sim r^0$, within a certain region, and this characteristic can be compared to the $\sim r^{-4/3}$-behavior of the density that one obtains for star polymers, for example. [220] It can be nicely seen how the architecture of the macromolecule that combines star-like elements but supplemented by a high degree of branching, affects the monomer distribution around the center. Finally, we note that the shape of our measured density profile is in agreement with the results of previous simulational studies employing a variety of microscopic models. [201, 202, 214, 215, 216, 217] The strength of the ordering oscillations close to the molecule's center depends, however, on the specific model used and in particular on the length of the spacer connecting adjacent monomers in relation to the diameter of the latter.

At distances $r/\sigma_{\rm LJ} \gtrsim 2$, the structure is lost and a smooth decay of $\rho(r)$ to zero is observed. The whole behavior of $\rho(r)$ is indicative of increasing fluctuations for monomers with higher generation number, which is further sustained by the broad density distribution

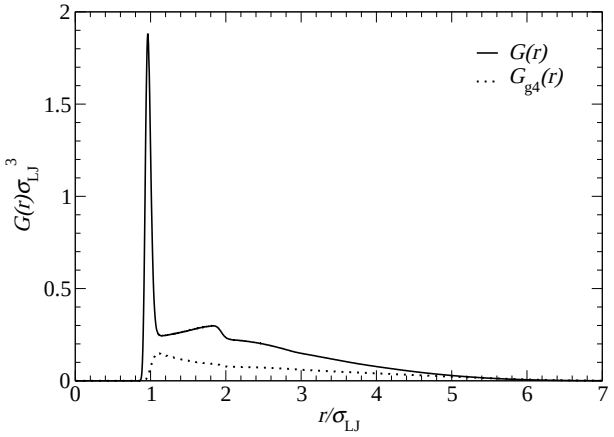


**Figure 4.5:** The pair distribution function of the monomers, calculated for all monomers (full line) and for the monomers of the last generation only (dotted line).

of the outermost generation, shown in Fig. 4.4 as the dotted line. The $\rho_{g4}(r)$-profile is in agreement with recent SANS-results on the endpoint distribution of fourth-generation dendrimers, obtained by using suitably labeled macromolecules. [208]

We now have a tool at hand to bridge the gap to experimental length scales and to give a microscopic meaning to the model parameter $\sigma_{\mathrm{LJ}}$. This is provided via the dendrimer's radius of gyration, that can be measured both in the simulation and in SANS. Its definition reads as

$$R_g = \sqrt{\frac{1}{N}\left\langle \sum_{i=1}^{N} \left(\mathbf{r}_i - \mathbf{r}_{\mathrm{CM}}\right)^2 \right\rangle}. \tag{4.21}$$

In the simulation, we obtain the value $R_g = \bar{R}_g \sigma_{\mathrm{LJ}}$, with $\bar{R}_g = 2.518$. Experimentally, this corresponds to the so-called 'radius of gyration at infinite contrast', $R_{g,\infty}$, which has been obtained for the molecules at hand by performing a series of careful experiments at different contrasts; [200, 219] the so-determined gyration radius is $R_{g,\infty} = 1.489\,\mathrm{nm}$. The simulation model reproduces, then, the real molecule's radius of gyration with the choice $\sigma_{\mathrm{LJ}} = R_{g,\infty}/\bar{R}_g = 0.591\,\mathrm{nm}$. This result compares favorably to the bond lengths calculated based on the chemical structure of the molecule under experimental observation. For a typical bond length $a \approx 1.5\,\text{Å}$ and a Kuhn length $\ell_{\mathrm{K}}$ of three to four monomer lengths, $\ell_{\mathrm{K}} \cong 6$ Å is obtained that agrees very well with the above-determined value of $\sigma_{\mathrm{LJ}}$ and thus further supports the interpretation of the latter as the length of a Kuhn segment of the polymer.

Additional information about the internal structure of the dendrimer can be obtained from the pair distribution function $G(\mathbf{r})$, defined in Eq. (4.4) and depending only on $r$ due to the restoring of spherical symmetry after averaging over all conformers. To this end, we measured the average number of pairs being separated by $r$ and normalized the histograms appropriately [10] in order to obtain $G(r)$. We omit in what follows the trivial $\delta$-function

contribution and display in Fig. 4.5 only the second term in the rhs of Eq. (4.4). The results further illustrate the statements made above based on the knowledge of the radial density distribution. The highly pronounced peak at $r \cong 0.97\sigma_{\rm LJ}$, the equilibrium distance of the Lennard-Jones–FENE potential, arises mainly from the strong correlations between directly connected beads. A considerably less pronounced structure is also seen at $r \lesssim 2\,\sigma_{\rm LJ}$, stemming from the second neighbors, which are however much more weakly correlated than the first ones. For higher $r$-values, these correlations are washed out and result in a smoothly decaying curve. As can be expected, the pair distribution function which is restricted to the monomers being members of the outermost (fourth) generation, is also peaked at the typical nearest neighbor distance. The relative height of the peak is much smaller, pointing at the fact that on average the monomers this far out fluctuate the strongest, resulting from the facts that (i) their movement is less restricted due to a reduced number of neighbors and (ii) beads of the last generation lack any direct connections among them.

We further measured the form factor $F(q)$ of the molecule by performing the averages given in its definition, Eq. (4.9), 'on the fly' during the simulation. A comparison with the Fourier transformed $G(r)$ yielded identical results, thus providing an independent check of the validity of the procedure. The simulation yields $F(q)$ as a function of the dimensionless variable $q\sigma_{\rm LJ}$ and the identification $\sigma_{\rm LJ} = 0.591\,{\rm nm}$ obtained above through the radius of gyration, allows us to express $F(q)$ in physical units and permits a comparison with experimental data. In the experiment, the total scattering intensity $I_S(q)$ is obtained, which is normalized at $q = 0$ as $I_S(0) = V_p^2$, with $V_p = 9.818\,{\rm nm}^3$ being the volume of the dendrimer molecule. [200] Thus, we furthermore rescale the ordinate to satisfy this condition for the simulation data as well. The result is shown in Fig. 4.6. Clearly, there is excellent agreement between the MC-simulation results and the SANS-data. Only in the range $1.5\,{\rm nm}^{-1} \lesssim q \lesssim 2\,{\rm nm}^{-1}$ do small deviations exist, but they are within the error bars. We can thus be confident that the model at hand does indeed capture the characteristics of the real dendrimers.

## 4.4 Discussion

We now wish to put into test the degree in which the form factor of the fourth-generation dendrimer can be approximated by Eqs. (4.11) or (4.16). Apart from the constant term of unity that corresponds to incoherent scattering, these are both expressions pertaining to molecules with uncorrelated fluctuations between the monomers or to very weak fluctuations in the first place. Adopting these expressions also for molecules in which correlations are present amounts to a Mean-Field Approximation (MFA) of their conformations: here one replaces $G(r)$ by the autoconvolution of $\rho(r)$.

In Fig. 4.7, we show the comparison of the form factor $F(q)$ with the MFA-expression $(1/N)\tilde{\rho}^2(q)$. It can be seen that in the small $q$-range the MFA is very good, with deviations only showing up for $q\sigma_{\rm LJ} \gtrsim 1$. It has to be kept in mind, however, that the limiting behavior of the two functions is different, since $F(q) \to 1$ for $q \to \infty$, whereas $(1/N)\tilde{\rho}^2(q) \to 0$

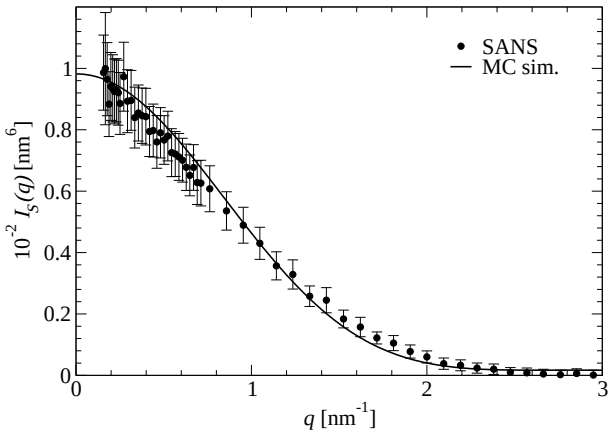


**Figure 4.6:** Form factor $F(q)$, as determined in the simulation (full line), displayed together with the form factor as determined in SANS experiments (circles). The rescaling procedure for the simulation data is explained in detail in the text.

for $q \to \infty$. Nonetheless on this level we can, from this data, conclude that the inherent approximation as discussed above, is very good and thus surmise that the dendrimer does not exhibit exceedingly large correlated fluctuations. On the other hand, it is clear that the question at hand should be further pursued, in particular with respect to first where the fluctuations are the most pronounced in the molecule and second what their absolute value, irrespective of the degree of correlation is.

In Fig. 4.8 we show the form factor in comparison to the MFA in more detail for high values of the scattering wavevector. To make the comparison easier, we have now subtracted the value 1 from the simulation data and we show thus only the coherent part, $F_{\mathrm{coh}}(q) = F(q) - 1$. Here, significant deviations can be seen, in the sense that $F(q)$ displays oscillations stemming from the short-range correlations between the particles, whereas the quantity $(1/N)\tilde{\rho}^2(q)$ is devoid of any structure. There is, however, no reason to expect that the MFA should be valid in this $q$-domain since here $q\sigma_{\mathrm{LJ}}$ exceeds unity and the condition $\mathbf{q} \cdot \Delta\mathbf{r}$ is not satisfied any more. Moreover, the typical wavelength of the oscillations of $F(q)$ seen in Fig. 4.8 demonstrates that the fluctuations are correlated on the scale of the Kuhn length. We are thus dealing with oscillatory structure in $q$-space that becomes visible at scattering wavevectors above, roughly, $q = 2.5 - 3.0\,\mathrm{nm}^{-1}$, and which cannot be easily resolved in the small-angle scattering experiments.

As an additional diagnostic tool for the deviations of the dendrimer from a rigid configuration, we measured the variance of the Fourier-transform of the density operator, $\Delta\tilde{\rho}(q)$, defined as

$$\Delta\tilde{\rho}(q) = \sqrt{\left\langle \hat{\rho}_{\mathbf{q}}^2 \right\rangle - \left\langle \hat{\rho}_{\mathbf{q}} \right\rangle^2} = \sqrt{\tilde{\rho}_2(q) - \tilde{\rho}^2(q)}, \tag{4.22}$$

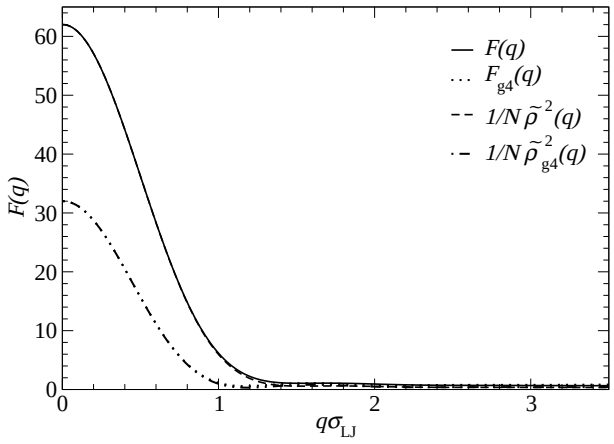


**Figure 4.7:** Form factor, $F(q)$, for the whole dendrimer (full line), as well as for the fourth generation only (dotted line), shown in comparison to $(1/N)\tilde{\rho}^2(q)$, for the whole dendrimer (dashed line) and the fourth generation (dash-dotted line), respectively.

where

$$\tilde{\rho}_2(q) \equiv \left\langle \hat{\rho}^2_{\mathbf{q}} \right\rangle = \left\langle \sum_{i=1}^{N} \sum_{j=1}^{N} \exp[-\mathrm{i}\mathbf{q} \cdot (\mathbf{r}_i + \mathbf{r}_j)] \right\rangle . \tag{4.23}$$

If marked, correlated fluctuations occur in the molecule, we expect significant differences in these two observables to show up. The result is shown in Fig. 4.9. As can be seen, $\tilde{\rho}_2(q)$ and $\tilde{\rho}^2(q)$ are practically indistinguishable. We may thus put forward the notion that the dendrimer does not, in its behavior regarding fluctuations, differ significantly from that of a spherically symmetric object whose constituents show uncorrelated fluctuations. Although this might sound counter-intuitive at first sight, there is good grounds for such a notion, since the density profile indicates that the dendrimer is very dense in its inner part. Here, only small fluctuations, showing up for very high $q$, should occur. As we could already further surmise from the density profile, the fluctuations are the strongest in the outer shell. Here, however, they are the least correlated, since the monomers in the outermost generation are the least connected, with only one bond per particle, inducing only weak correlations.

Recently, a mean-field type theory for the effective interactions between G4-dendrimers has been proposed. [199, 200] It is based on the inversion of SANS-scattering profiles in the spirit of Eq. (4.16), in which the form factor $F(q)$ is used to obtain directly the density profile $\rho(r)$. This is akin to self-consistent field theories of dendrimers in which each monomer finds itself in the mean-field caused by all other monomers. [218] Self-consistent field approaches also result into smooth density profiles and into a loss of correlations in the shape of the scattering profiles. [218, 229] Since the measured form factor of G4-dendrimers is excellently fitted by a Gaussian function in the measured regime, Eq. (4.16) leads also to a Gaussian density profile. A second ingredient of the theory is the introduction of a Flory-type monomer-monomer interaction $v_{\mathrm{mm}}(\mathbf{r}_1 - \mathbf{r}_1) = k_B T v_0 \delta(\mathbf{r}_1 - \mathbf{r}_2)$, with the excluded-volume

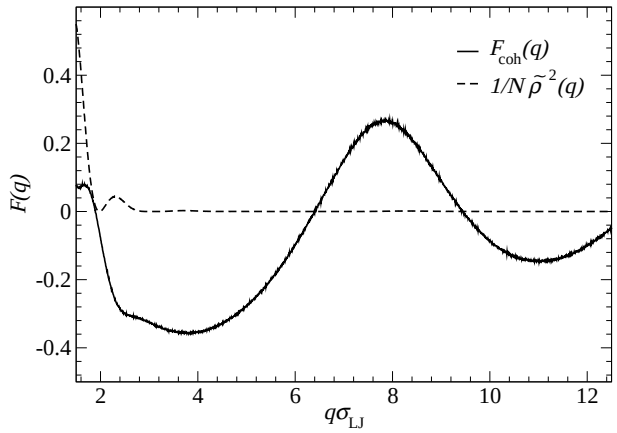


**Figure 4.8:** The coherent form factor $F_{\rm coh}(q) = F(q) - 1$, compared with its mean-field approximation, Eq. (4.16) at high values of the scattering wavevector.

parameter $v_0$. Under the assumption that the dendrimers maintain their undisturbed shape even in interacting situations, the above procedure leads then to a Gaussian effective interaction between G4-dendrimers that has been shown to provide an excellent theoretical description of the scattering profiles from dendrimer solutions below the overlap concentration, [200] with the choice $v_0 = 0.076\,\mathrm{nm}^{-1}$. In comparing the measured density profile shown in Fig. 4.4 with the mean-field prediction of a Gaussian shape, it appears that the latter is not particularly accurate; all ordering effects in the inner region of the molecule are lost. Nevertheless, the remarkable success of the Gaussian effective interaction in conjunction with the present accurate data calls for an explanation.

To this end, we have to remember that in the Flory-view of polymers, every monomer is 'chopped down' to a continuous distribution of matter that interacts by means of the $\delta$-interaction mentioned above, pretty much as discrete charge matter is replaced by a continuous charge distribution in some circumstances. Thus, we proceed by considering every bead in our model as a uniform distribution of monomeric matter and introduce thereby the density of 'effective monomers' inside the bead:

$$\rho_{\rm b}(r) = \frac{3}{4\pi R^3}\Theta(R-r), \tag{4.24}$$

where $R = \sigma_{\rm LJ}/2$ is the radius of the bead and $r$ is the distance from its center. Accordingly, the distribution of effective monomers around the dendrimer's center of mass, $\rho_{\rm m}(r)$ is given by the convolution

$$\rho_{\rm m}(r) = [\rho \otimes \rho_{\rm b}](r). \tag{4.25}$$

In Fig. 4.10, we compare the density $\rho_{\rm m}(r)$ with the Gaussian distribution obtained by the inversion of the scattering data in the mean-field approach of Ref. [200]; the two are still considerably different from one another. However, the effective interaction $V_{\rm eff}(R)$ between the dendrimers is proportional to a second convolution, namely the autoconvolution of the

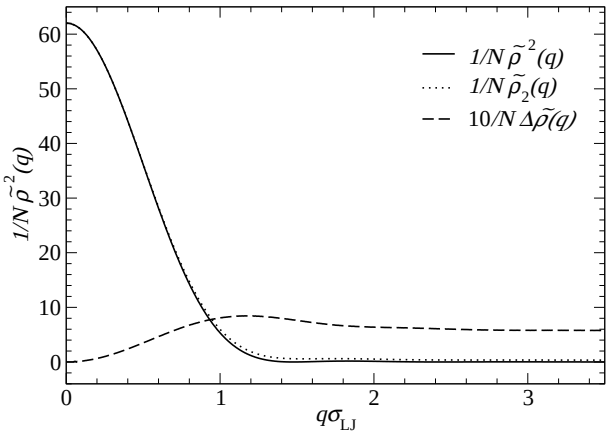


**Figure 4.9:** The quantities $\tilde{\rho}^2(q)$ and $\tilde{\rho}_2(q)$ defined in the text, as obtained in the simulation of the fourth-generation dendrimer. Also shown is the quantity $\Delta\tilde{\rho}(q)$ which, for reasons of clarity, has been multiplied by a factor 10.

effective monomer density, i.e.,

$$V_{\text{eff}}(R) = k_B T v_0 [\rho_{\text{m}} \otimes \rho_{\text{m}}](R). \tag{4.26}$$

In Fig. 4.11, we show the final comparison between the effective interaction obtained by the mean-field theory of Ref. [200] and the one obtained by employing the coarse-grained monomer density $\rho_{\text{m}}(r)$ of Eq. (4.25) above. It can be seen that the two are very similar to one another and practically identical at separations between 3 and 4 nm. Since the theory of Ref. [200] was put forward for dendrimers below their overlap concentration, such that the macromolecules slightly overlap only on their periphery, it is clear that the two effective interactions will yield identical results for the structure factor there. Thus, the mean-field approach is once more justified, not only for the conformations of dendrimers but for the effective interactions between the same as well.

## 4.5 Conclusions and Outlook

In conclusion, we have investigated the structural properties of an isolated fourth generation dendrimer. We calculated the density profile, which could confirm that the dendrimer is a dense object in its inner regions. By measuring the form factor $F(q)$ of the single dendrimer and a comparison to experimental data, an excellent agreement of simulation and experiment was found. By comparing $F(q)$ to the squared Fourier transform of the density distribution $\tilde{\rho}^2(q)$, it was shown that the dendrimer is, on average, a spherically symmetric object whose constituents do not show large correlated fluctuations. This was further underlined by comparing $\langle\hat{\rho}_{\mathbf{q}}\rangle^2$ with $\langle\hat{\rho}^2_{\mathbf{q}}\rangle$. The fluctuations present in a dendritic molecule as investigated in the present study occur for $q \gtrsim 2.5 - 3.0\,\text{nm}^{-1}$. With the structural properties of a single

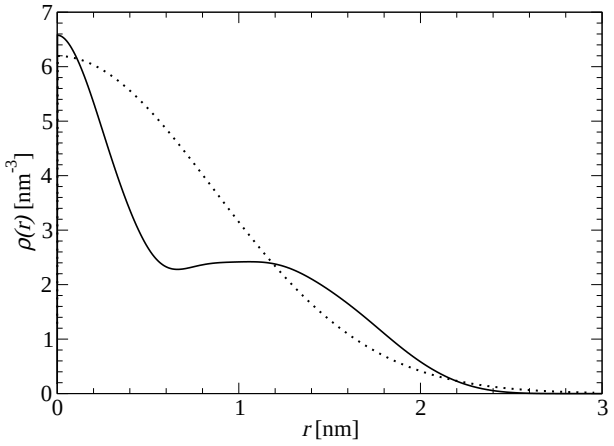


**Figure 4.10:** The coarse-grained monomer density $\rho_{\mathrm{m}}(r)$ defined by Eq. (4.25) (solid line) compared with the mean-field Gaussian density (dotted line). The latter is obtained by the inversion of the Gaussian form factor measured from dilute solutions of G4-dendrimers.

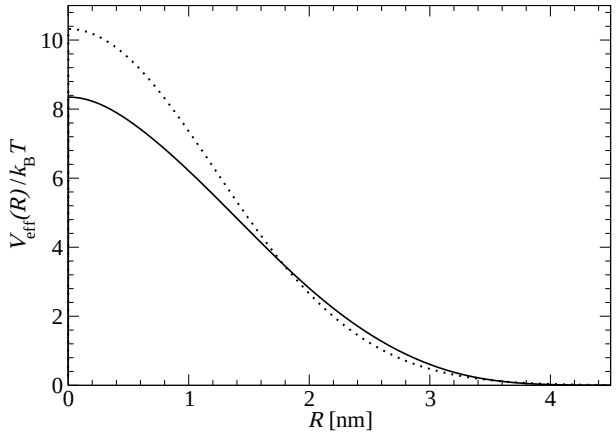


**Figure 4.11:** Comparison of the effective interaction obtained by Eq. (4.26) of the text by employing the density profile $\rho_{\mathrm{m}}(r)$ of Eq. (4.25) (solid line) with the mean-field result based on a Gaussian profile (dotted line). For completeness, we note that the dotted line is obtained from Eq. (18) of Ref. [200], with $N = 62$ monomers and $v_0 = 0.076\,\mathrm{nm}^{-1}$. This value of $v_0$ has also been used to produce the solid curve, according to Eq. (4.26) of the text.

dendrimer of the fourth generation having been investigated, we can now turn our attention to two related questions: first, the systematic dependence of the quantities characterizing dendrimer conformations on the maximum generation number $g$ and the further evolution of the dendrimers towards the compact colloid limit. [228] Second, the question of dendrimer-dendrimer interaction: it will be of major interest whether for small overlaps the Gaussian

interaction picture will be confirmed and to which extent it will be modified for more significant overlaps between the two dendritic architectures. To answer these questions, we will resort to Molecular Dynamics simulations of dendrimers of the same kind as presented here. A careful check with theoretical predictions for the dendrimer-dendrimer interaction will then become possible.

*In the following, last chapter we will summarize the results presented in the preceding chapters and we will discuss possible future extensions of the present work.*

# Chapter 5

# Summary and Outlook

Summarizing, we have investigated aspects of four different soft matter systems, using methods of statistical physics. In chapter 1 we treated DNA molecules in a columnar assembly. We were able to calculate the pair interaction potential of two DNA molecules in a parallel state as found in columnar assemblies. To achieve this, we adopted the Debye-Hückel (DH) linear screening picture, inducing a Yukawa- or DLVO-type potential for the interaction of all infinitesimal charge elements. The so-obtained DNA pair potential $U(R, \phi)$, depending on the interaxial separation $R$ as well as the mutual azimuthal orientation angle $\phi$ was compared to an analytical solution [14] of the DNA pair potential problem, obtained by solving the linearized Poisson-Boltzmann (PB) equation under explicit incorporation of the helical charge patterns. Good qualitative agreement between the two potentials was found. Building on the two pair potentials we calculated the lattice-structural as well as the orientational phase behavior of a DNA columnar assembly, making use of lattice sums together with the entropic contributions of the mixture's constituents. In the case of counterion condensation *on strands* a purely repulsive interaction was found to give rise to a *HEX* lattice, on which, due to frustrations of the angular part of the interaction, orientational phase transitions by variation of the relevant parameters, DNA packing fraction $\pi\rho a^2$ and salt concentration $n_s$ were detected. Switching to a different type of counterions which do not exhibit specific interactions with the phospates located on the DNA backbone induces counterion condensation to occur to a major part *in the major groove*. This, as a consequence, leads to strong attractions between the DNA molecules, giving rise to DNA bundling in the assembly. We thus find broad coexistence regions between DNA-free salt solutions and high density DNA phases. This behavior is qualitatively robust with respect to a change in the charge compensation. The phase diagrams agree well on a qualitative level for the YS and the KL model case. There is a number of simplifications included in the present theory. Although there is conclusive evidence that the level of complexity thereby attained suffices to yield the essential features and predictions for columnar DNA assemblies, put in other words, that we have devised a *minimal model*, it poses nonetheless a great challenge to extend the model's complexity further and to then compare the results to the one presented in this

thesis. We will briefly discuss a few possible extensions in the following, in increasing order of importance. Neglected in this work are effects of hydration forces, steric interactions, hydrogen bonds and ordered water molecules around the DNA cores as well as, on the level of the aggregate, many body effects. These would presumably change the current picture the least, so that it would probably be sensible to rather consider a type of modeling which goes further in the description of the counterions than the present one. There is good grounds, however, to believe that this would not have a dramatic effect, since Molecular Dynamics (MD) simulations in the framework of the primitive model (PM) yielded similar pair interaction potential curves as the present work if appropriate charge renormalizations were carried out. In a second step one might try to investigate possible edge effects, since here, the DNA molecules were assumed to be infinitely long. In experiments, however, because of the short length of *real* DNA fragments, edge effects could have an influence, possibly diminishing the importance of the helical structure of DNA which is essential in the analysis presented here. Finite molecules would also have to be used in the model if, in a subsequent and the most interesting step, which most probably brings in *qualitatively new* features, tilts of the DNA molecules with respect to one another were to be included. Although only relevant for interaxial separations $R > 34$Å, the occurrence of the *cholesteric phase* (CP) is a very interesting issue, which is of importance in experiments [45, 55, 43, 69].

In chapter 2 we calculated the ground state adsorption patterns colloids form on surfaces which exhibit a stripe-structure. We resorted to ground state calculations, whereby the colloid-colloid interaction was hard-sphere like and the attractive colloid-substrate interaction was modeled by a square-well interaction with the well-depth as free parameter. The other parameter entering the phase behavior was the stripe-width and the inter-stripe separation. We found that depending on these two variables, various complex decoration lattices form on the patterned substrate. Interesting extensions are possible in several directions: One might first perform the same calculations for other substrate patterns. Subsequently the potentials involved could be rendered more complex and finite temperature effects might be incorporated. Finally non-equilibrium effects in the adsorption process and pattern formation would present a notable challenge.

Finally, chapter 3 was devoted to a study of star polymers in a gravitational field. Star polymers where chosen as representative of the class of systems exhibiting reentrant melting behavior in the bulk phase diagram. We could confirm the surmise, namely that the reentrant melting behavior which is present as a function of the density gets mapped onto the height $z$ in the gravitational field, giving rise to a crystal sheet intercalated in a low density fluid at high and a high density fluid at lower elevations. Furthermore it was found that this effect only appears below a critical gravitational strength. Above this critical value, monotonic density profiles are obtained.

In the investigation of the properties of an isolated dendrimer, presented in chapter 4 it was found that the dendrimer is, in its inner regions, a dense object. It can, to a certain extent, be regarded as a compact colloid. This is due to the fact that the correlated

fluctuations of its constituent monomers are remarkably small. The calculated form factor was in very good agreement with experimental results. In a subsequent step, we will turn our attention to the dendrimer-dendrimer interaction in the framework of the same model. Furthermore, the systematic dependence of the averaged properties being characteristic of the dendrimer conformations will be calculated as a function of the dendrimer generation $g$, whereby a further evolution towards the compact colloid behavior with increasing dendrimer generation number is conjectured.

For every theoretical work a high distinction is a favorable agreement with experiments in the best case or at least a comparison with experiment at all. For the dendrimers, an experimental verification of the theoretical results was already possible in parts. As for the other projects, the current state of comparison is less satisfactory: The pair potential of star polymers has experimentally been, in good parts, confirmed by structure factor measurements, the bulk phase diagram is, however, not easily accessible. Also sedimentation profiles are not yet available but can in principle be obtained by employing strong centrifugation or by creating star-like micelles (by grafting long polymer chains on big colloidal particles) with an identical phase behavior to the one of star polymers, their advantage, however being their much larger mass. Colloidal adsorption on patterned substrates is a very active area of experimental research, which has become a major interest since the uprise of viable real-space analysis tools. From these experiments there is good grounds to believe that the theoretical predictions are at least in the ballpark of what can be expected experimentally.

The least degree of comparison to experiments exists in the case of the phase behavior of columnar DNA assemblies: Although some characteristics derived on the basis of the KL pair potential agree very well with the corresponding ones calculated on the basis of experimental evidence, the only possibility to compare the predictions of the theory and real-life columnar DNA assemblies is the fact that in both cases hexagonal *HEX* lattices are observed. Verification of the different lattice structures, least to say of the imprinted orientational structures is beyond the scope of present experimental techniques. It can be hoped however, that with the advent of higher resolution X-ray diffraction techniques a comparison of the predicted phase behavior to experimental data would become possible to maybe accomplish every researcher's dream: to see theory and experiment in agreement.

# List of Abbreviations

| | |
|---|---|
| *AFH* | Antiferromagnetic Heisenberg |
| *AFI* | Antiferromagnetic Ising |
| *AFP* | Antiferromagnetic Potts |
| CP | Cholesteric Phase |
| DFT | Density Functional Theory |
| DH | Debye-Hückel |
| DNA | Deoxyribonucleic Acid |
| DLVO | Derjaguin-Landau-Verwey-Overbeek |
| FENE | Finite Extensible Nonlinear Elastic |
| *FM* | Ferromagnetic |
| HS | Hard Sphere |
| *HEX* | Hexagonal |
| KL | Kornyshev-Leikin |
| LJ | Lennard-Jones |
| MC | Monte-Carlo |
| MD | Molecular Dynamics |
| MFA | Meanfield Approximation |
| *OBL* | Oblique |
| PE | Polyelectrolyte |
| PB | Poisson-Boltzmann |
| PM | Primitive Model |
| PMMA | Polymethylmethacrylate |
| *REC* | Rectangular |
| *RHO* | Rhombic |
| RY | Rogers-Young |
| SANS | Small Angle Neutron Scattering |
| SAXS | Small Angle X-ray Scattering |
| *SQ* | Square |
| YS | Yukawa-Segment |

# Appendix

*This appendix gives information on technical issues concerning this work. Appendix A deals with the problem of finding phase coexistence regions in two-component mixtures, applied to the issue of a DNA-salt solution.*

# Appendix A

# ON DETERMINING PHASE COEXISTENCE REGIONS

The problem to be solved is the phase behavior of a two component system, with, in our case, one component being DNA, the other being salt with numbers $N_1$ and $N_2$ respectively. The number of counterions is directly coupled to $N_2$ (as the salt co- and counterions are to each other) via the condition of global charge neutrality. Assume the Helmholtz free energy $F(N_1, N_2, V, T)$ to be known. Statistical Mechanics and thermodynamics state that the free energy shall be convex for the system to be stable. The route to achieve this in simple one component systems is the so-called double tangent construction whereby the non-convex parts are 'bridged' by a tangent onto the two points $N^A$ and $N^B$ where the concave parts of the free-energy curve start. These two points are the delimiting loci of phase coexistence between phase $A$ at $N^A$ and phase $B$ present at $N^B$. The conditions to be fulfilled for stability and which are, by construction properly incorporated in the double tangent construction are first: equality of pressure, $P^A = P^B$ and equality of chemical potentials, $\mu^A = \mu^B$ in the two phases. Generalizing this for a two-component system, a corresponding 'two-component' double tangent construction has to satisfy the following conditions: $\mu_1^A = \mu_1^B$, $\mu_2^A = \mu_2^B$ and $P^A = P^B$. The second of these three conditions can automatically be fulfilled by operating on $\mu_2 = const$ curves only.

It is thereby convenient to carry out a Legendre transformation to the semigrand potential $Y(N_1, \mu_2, V, T) = F(N_1, N_2, V, T) - \mu_2 N_2$ [230]. It is understood that by keeping $\mu_2$ fixed $N_2$ becomes a function of $N_1$. We will henceforth omit the arguments $V$ and $T$ for simplicity. Consider now

$$\begin{aligned} \mu_1 &\equiv \left.\frac{\partial F}{\partial N_1}\right|_{N_2} \\ &= \left.\frac{\partial Y}{\partial N_1}\right|_{\mu_2} + \left.\frac{\partial Y}{\partial \mu_2}\right|_{N_1} \left.\frac{\partial \mu_2}{\partial N_1}\right|_{N_2} + \left.\frac{\partial \mu_2}{\partial N_1}\right|_{N_2} N_2. \end{aligned} \tag{A.1}$$

Since $\partial Y/\partial \mu_2|_{N_1} = -N_2$ according to the definition of $Y$ as Legendre transform of $F$ above,

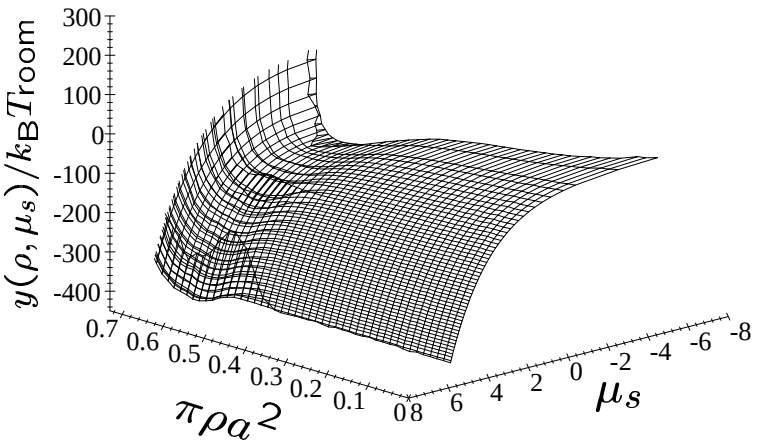


**Figure A.1:** Semigrand potential per unit volume $y(\rho, \mu_s)$ as a function of reduced DNA density and salt chemical potential, for the KL model and parameters $\theta = 0.9$, $f_1 = 0.3$, $f_2 = 0.7$, $f_3 = 0$.

the last two terms cancel and we obtain:

$$\mu_1 = \left.\frac{\partial Y}{\partial N_1}\right|_{\mu_2} . \tag{A.2}$$

In an analogous way we obtain

$$P = -\left.\frac{\partial Y}{\partial V}\right|_{N_1,\mu_2} . \tag{A.3}$$

Introducing now the semigrand potential density $y(n_1, \mu_2) = V^{-1}Y(N_1, \mu_2, V)$ with $n_1 = V^{-1}N_1$ it is straightforward to show that

$$\mu_1 = \frac{\partial y}{\partial n_1} \tag{A.4}$$

$$P = n_1\frac{\partial y}{\partial n_1} - y, \tag{A.5}$$

demonstrating that $\mu_1^A = \mu_1^B$ and $P^A = P^B$ is guaranteed by performing a common tangent construction on the $y$–versus–$n_1$ curves. In applying the above considerations to the present case, we have the salt chemical potential $\mu_s \equiv \mu_2$ and the DNA density $\rho \equiv n_1$. In Fig. A.1 the semigrand potential surface $y(\rho, \mu_s)$ for the KL model is shown as a function of DNA density $\rho$ and salt chemical potential $\mu_s$, for a charge compensation of $\theta = 0.9$. The counterion parameters are $f_1 = 0.3$, $f_2 = 0.7$, $f_3 = 0$. One can clearly discern the non-convex parts which lead to phase coexistence. The double tangent construction is performed on the curve displayed in Fig. A.2, as indicated by the dashed line. It shows the semigrand potential $y(\rho, \mu_s = const)$ as a function of DNA density $\rho$ at constant salt chemical potential, $\mu_s = const$. Due to the broad non-convex part, the broad phase coexistence region emerges in

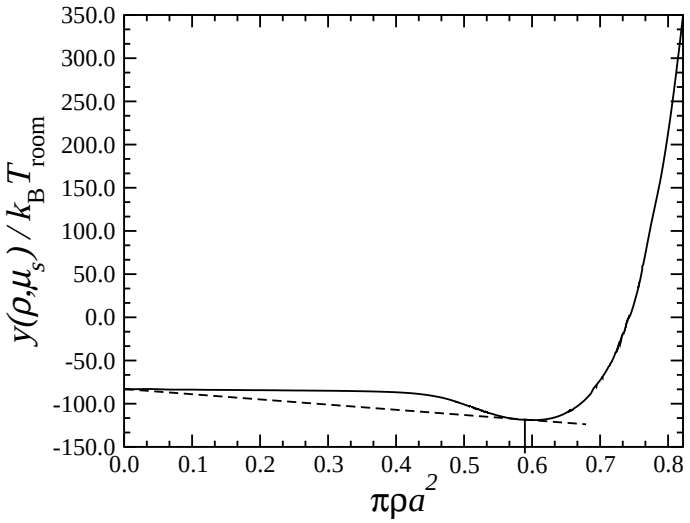


**Figure A.2:** Semigrand potential per unit volume $y(\rho, \mu_s)$ on a line of constant DNA chemical potential for the KL model as a function of the reduced DNA density and for parameters $\theta = 0.9$, $f_1 = 0.3$, $f_2 = 0.7$, $f_3 = 0$. Also shown (dashed line) is the common tangent connecting the coexisting phase points.

the phase diagrams. The oblique tielines are obtained by calculating the salt concentrations $n_s^A$ and $n_s^B$ at the coexisting DNA densities $\rho^A$ and $\rho^B$.

# Bibliography


[1] R. J. Hunter, *Foundations of Colloid Science*, vol. 1 (Clarendon Press, Oxford, 1986).

[2] S. A. Safran and N. A. Clark, eds., *Physics of Complex and Supermolecular Fluids* (Wiley Interscience, New York, 1987).

[3] W. B. Russel, D. A. Saville, and W. R. Schowalter, *Colloidal Dispersions* (Cambridge University Press, Cambridge, 1989).

[4] H. Löwen, M. Watzlawek, C. N. Likos, M. Schmidt, A. Jusufi, J. Dzubiella, C. von Ferber, E. Allahyarov, A. Thünemann, and I. D'Amico, Advances in Solid State Physics **40**, 809 (2000).

[5] V. A. Bloomfield, Curr. Opin. Struct. Biol. **6**, 334 (1996).

[6] W. M. Gelbart, R. F. Bruinsma, P. A. Pincus, and V. A. Parsegian, Phys. Today **53**, 38 (2000).

[7] C. N. Likos, Physics Reports **348**, 267 (2001).

[8] C. N. Likos, H. Löwen, M. Watzlawek, B. Abbas, O. Jucknischke, J. Allgaier, and D. Richter, Phys. Rev. Lett. **80**, 4450 (1998).

[9] A. Jusufi, M. Watzlawek, and H. Löwen, Macromolecules **32**, 4470 (1999).

[10] M. P. Allen and D. J. Tildesley, *Computer Simulation of Liquids* (Clarendon, Oxford, 1987).

[11] D. Frenkel and B. Smit, *Understanding Molecular Simulation* (Academic, San Diego, 1996).

[12] A. Wolffe, *Chromatin, Structure and Function* (Academic Press, San Diego, 1992).

[13] N. Grønbech Jensen, R. J. Mashl, R. F. Bruinsma, and W. M. Gelbart, Phys. Rev. Lett. **78**, 2477 (1997).

[14] A. A. Kornyshev and S. Leikin, J. Chem. Phys. **107**(9), 3656 (1997), erratum, *ibid.* **108**, 7035 (1998).

[15] B.-Y. Liu and A. J. Liu, Phys. Rev. Lett. **79**, 1289 (1997).

[16] R. Podgornik and V. A. Parsegian, Phys. Rev. Lett. **80**, 1560 (1998).

[17] B. I. Shklovskii, Phys. Rev. Lett. **82**, 3268 (1999).

[18] A. A. Kornyshev and S. Leikin, Phys. Rev. Lett. **82**(20), 4138 (1999).

[19] T. T. Nguyen, I. Rouzina, and B. I. Shklovskii, J. Chem. Phys. **112**, 2562 (2000).

[20] E. Allahyarov and H. Löwen, Phys. Rev. E **62**, 5542 (2000).

[21] B.-Y. Ha and A. J. Liu, Phys. Rev. E **63**, 021503 (2001).

[22] Y. Levin, J. J. Arenzon, and J. F. Stilck, Phys. Rev. Lett. **83**, 2680 (1999).

[23] J. P. Hansen and H. Löwen, Annu. Rev. Phys. Chem. **51**, 209 (2000).

[24] Y. Levin, Rep. Prog. Phys. **65**, 1577 (2002).

[25] H. H. Strey, V. A. Parsegian, and R. Podgornik, Phys. Rev. E **59**(1), 999 (1999).

[26] H. H. Strey, V. A. Parsegian, and R. Podgornik, Phys. Rev. Lett. **78**(5), 895 (1997).

[27] F. Oosawa, *Polyelectrolytes* (Marcel Dekker, New York, 1971).

[28] D. Stigter, Biopolymers **16**, 1435 (1977).

[29] G. S. Manning, Q. Rev. Biophys **11**, 179 (1978).

[30] M. D. Frank-Kamenetskii, V. V. Anshelevich, and A. V. Lukashin, Sov. Phys. Usp. **30**, 317 (1987).

[31] W. Wilson and V. A. Bloomfield, Biochem. **18**, 2192 (1979).

[32] J. Widom and R. L. Baldwin, J. Mol. Biol. **144**, 431 (1980).

[33] P. G. Heath and J. M. Schurr, Macromolecules **25**, 4149 (1992).

[34] J. Pelta, F. Livolant, and J.-L. Sikorav, J. Biol. Chem. **271**, 5656 (1996).

[35] D. C. Rau, B. Lee, and V. A. Parsegian, Proc. Natl. Acad. Sci. USA. **81**, 2621 (1984).

[36] A. H. Tajmir-Riahi, M. Naoui, and R. Ahmad, J. Biomol. Struct. Dyn. **11**, 83 (1993).

[37] I. Fita, J. Campos, L. Puigjaner, and J. Subirana, J. Mol. Biol. **167**, 157 (1983).

[38] N. V. Hud, F. P. Milanovich, and R. Balhorn, Biochem. **33**, 7528 (1994).

[39] X. Q. Shui, L. McFail-Isom, G. G. Hu, *et al.*, Biochem. **37**, 8341 (1998).

[40] R. Podgornik, H. H. Strey, and V. A. Parsegian, Curr. Opin. Colloid Interface Sci. **3**, 534 (1984).

[41] C. Robinson, Tetrahedron **13**, 219 (1961).

[42] R. W. Wilson and V. A. Bloomfield, Biochem. **18**, 2192 (1979).

[43] F. Livolant and Y. Bouligand, J. Physique **47**, 1813 (1986).

[44] R. L. Rill, T. E. Strzelecka, M. W. Davidson, and D. H. van Winkle, Physica A **176**, 87 (1991).

[45] F. Livolant, Physica A **176**, 117 (1991).

[46] D. C. Rau and V. A. Parsegian, Biophys.J. **61**, 246 (1992).

[47] D. C. Rau and V. A. Parsegian, Biophys.J. **61**, 260 (1992).

[48] C. Ma and V. A. Bloomfield, Biophys.J. **67**, 1678 (1994).

[49] A. A. Kornyshev and S. Leikin, Proc. Natl. Acad. Sci. USA. **95**, 13579 (1998).

[50] V. Lorman, R. Podgornik, and B. Žekš, Phys. Rev. Lett. **87**, 218101 (2001).

[51] H. M. Harreis, A. A. Kornyshev, C. N. Likos, H. Löwen, and G. Sutmann, Phys. Rev. Lett. **89**, 018303 (2002).

[52] I. Lee, B. D. Athey, A. W. Wetzel, W. Meixner, and J. James R. Baker, Macromolecules **35**, 4510 (2002).

[53] W. Saenger, *Principles of Nucleic Acid Structure* (Springer Verlag, New York, 1984).

[54] A. A. Kornyshev and S. Leikin, Phys. Rev. Lett. **84**(11), 2537 (2000).

[55] R. Podgornik, H. H. Strey, K. Gawrisch, D. C. Rau, A. Rupprecht, and V. A. Parsegian, Proc. Natl. Acad. Sci. USA. **93**(9), 4261 (1996).

[56] See e.g., F. Lado, E. Lomba, and M. Lombardero, J. Chem. Phys. **108**, 4530 (1998).

[57] R. R. Sinden, *DNA Structure and Function* (Academic Press, New York, 1994).

[58] J. Schneider, W. Hess, and R. Klein, J. Phys. A: Math. Gen. **18**, 1221 (1985).

[59] J. Schneider, W. Hess, and R. Klein **19**, 1729 (1986).

[60] J. Schneider, D. Karrer, J. K. G. Dhont, and R. Klein, J. Chem. Phys. **87**, 3008 (1987).

[61] H. Löwen, Phys. Rev. Lett. **72**, 424 (1994).

[62] H. Löwen, J. Chem. Phys. **100**, 6738 (1994).

[63] T. Kirchhoff, H. Löwen, and R. Klein, Phys. Rev. E **53**, 5011 (1996).

[64] H. Graf and H. Löwen, Phys. Rev. E **59**, 1932 (1999).

[65] A. A. Kornyshev and S. Leikin, Biophys.J. **75**, 2513 (1998).

[66] H. H. Strey, J. Wang, R. Podgornik, A. Rupprecht, L. Yu, V. A. Parsegian, and E. B. Sirota, Phys. Rev. Lett. **84**(14), 3105 (2000).

[67] This persistence length has to be distinguished from a smaller correlation scale which is decreasing due to deflections of the polymer within the tube.

[68] G. J. Vroege and H. N. W. Lekkerkerker, Rep. Prog. Phys. **55**(8), 1241 (1992).

[69] D. Durand, J. Doucet, and F. Livolant, J. Phys. II **2**, 1769 (1992).

[70] J.-P. Hansen and I. R. McDonald, *Theory of Simple Liquids* (Academic Press, London, 1986), 2nd ed.

[71] A. C. Mitus, H. Weber, and D. Marx, Phys. Rev. E **55**, 6885 (1997).

[72] N. W. Ashcroft and D. Stroud, Solid State Phys. **33**, 1 (1978).

[73] J. S. Rowlinson, Mol. Phys. **52**, 567 (1984).

[74] E. Canessa, M. J. Grimson, and M. Silbert, Mol. Phys. **64**, 1195 (1988).

[75] M. J. Grimson and M. Silbert, Mol. Phys. **74**, 397 (1991).

[76] H. Graf and H. Löwen, Phys. Rev. E **57**, 5744 (1998).

[77] R. van Roij, M. Dijkstra, and J.-P. Hansen, Phys. Rev. E **59**(2), 2010 (1999).

[78] A. R. Denton, J. Phys.: Condens. Matter **11**, 10061 (1999).

[79] A. R. Denton, Phys. Rev. E **62**, 3855 (2000).

[80] G. Giannoni, F. J. Padden, and H. D. Keith, Proc. Natl. Acad. Sci. USA. **62**, 964 (1969).

[81] L. S. Lerman, L. S. Wilkerson, J. H. Venable, and B. M. Robinson Jr, J. Mol. Biol. **108**, 271 (1976).

[82] F. Livolant, A. M. Levelut, J. Doucet, and J. P. Benoit, Nature **339**, 724 (1989).

[83] J. M. Yeomans, *Statistical Mechanics of Phase Transitions* (Clarendon, Oxford, 1992).

[84] S. Rice, M. Nasagawa, and H. Morawetz, *Polyelectrolyte Solutions* (Academic Press, New York, 1961).

[85] H. Grimm and A. Ruprecht, Physica B **174**, 291 (1991).

[86] R. Langridge, H. R. Wilson, C. W. Hooper, M. H. F. Wilkins, and L. D. Hamilton, J. Mol. Biol. **2**, 19 (1960).

[87] S. D. Dover, J. Mol. Biol. **110**, 699 (1977).

[88] For a recent review see:, Y. Xia, D. Qin, and Y. Yin, Current Opinion in Colloid and Interface Science **6**, 54 (2001).

[89] See, e.g. , S. Friebel, J. Aizenberg, S. Abad, and P. Wiltzius, Appl. Phys. Lett. **77**(15), 2406 (2000).

[90] P. Lenz and R. Lipowsky, Phys. Rev. Lett. **80**, 1920 (1998).

[91] P. Lenz and R. Lipowsky, Europhys. J. E **1**, 249 (2000).

[92] S. Herminghaus, A. Fery, S. Schlagowski, K. Jacobs, R. Seemann, H. Gau, W. Mönch, and T. Pompe, J. Phys. Condensed Matter **12**, A57 (2000).

[93] C. Bauer and S. Dietrich, Phys. Rev. E **60**, 6919 (1999).

[94] L. J. Frink and A. G. Salingers, J. Chem. Phys. **110**, 5969 (1999).

[95] H. Bock and M. Schoen, Phys. Rev. E **59**, 4122 (1999).

[96] H. Bock and M. Schoen, J. Phys. Condensed Matter **12**, 1569 (2000).

[97] R. Lipowsky, Current Opinion in Colloid and Interface Science **6**, 40 (2001).

[98] J. Aizenberg, P. V. Braun, and P. Wiltzius, Phys. Rev. Lett. **84**, 2997 (2000).

[99] T. R. Weikl and R. Lipowsky, Langmuir **16**, 9338 (2000).

[100] H. Clausen-Schaumann and H. E. Gaub, Langmuir **15**, 8246 (1999).

[101] A. Sanjoh and T. Tsukihara, J. Crystal Growth **196**, 691 (1999).

[102] J. Aizenberg, A. J. Black, and G. M. Whitesides, Nature **398**, 495 (1998).

[103] M. Heni and H. Löwen, Phys. Rev. Lett. **85**, 3668 (2000).

[104] M. Heni and H. Löwen, J. Phys. Condensed Matter **13**, 4675 (2001).

[105] M. Böltau, S. Walheim, J. Mlynek, G. Krausch, and U. Steiner, Nature **391**, 877 (1998).

[106] B. H. Weigl and P. Yager, Science **283**, 346 (1999).

[107] H. Gau, S. Herminghaus, P. Lenz, and R. Lipowsky, Science **283**, 46 (1999).

[108] F. Burmeister, W. Badowsky, T. Braun, S. Wieprich, J. Boneberg, and P. Leiderer, Applied Surface Science **145**, 461 (1999).

[109] F. Burmeister, C. Schäfle, B. Keilhofer, C. Bechinger, J. Boneberg, and P. Leiderer, Chemical Engineering and Technology **21**, 761 (1998).

[110] C. Mio and D. W. M. Marr, Langmuir **15**, 8565 (1999).

[111] K. M. Chen, X. Jiang, L. C. Kimerling, and P. T. Hammond, Langmuir **16**, 7825 (2000).

[112] C. A. Murray, Abstr. Pap. Am. Chem. **220**, 74 (2000).

[113] K. Mangold, R. Bubeck, P. Leiderer, and C. Bechinger, to be published in Progr. Colloid Polym. Sci. (2001).

[114] Z. Adamczyk, B. Siwek, and E. Musial, Langmuir **17**, 4529 (2001).

[115] Q. Guo, C. Arnoux, and R. E. Palmer, Langmuir **17**, 7150 (2001).

[116] Y.-H. Ye, S. Badilescu, V.-V. Truong, P. Rochon, and A. Natansohn, Appl. Phys. Lett. **79**(6), 872 (2001).

[117] A. Chowdhury, B. J. Ackerson, and N. A. Clark, Phys. Rev. Lett. **55**(8), 833 (1985).

[118] A. K. Arora and R. Rajagopalan, Current Opinion in Colloid and Interface Science **2**, 391 (1997).

[119] A. van Blaaderen, R. Ruel, and P. Wiltzius, Nature **385**, 321 (1997).

[120] K. hui Lin, J. C. Crocker, V. Passad, A. Schofield, D. A. Weitz, T. C. Lubensky, and A. G. Yodh, Phys. Rev. Lett. **85**(8), 1770 (2000).

[121] F. Burmeister, C. Schäfle, T. Matthes, M. Bohmisch, J. Boneberg, and P. Leiderer, Langmuir **13**, 2983 (1997).

[122] C. Rotsch and M. Radmacher, Langmuir **13**, 2825 (1997).

[123] S. J. Miklavic, D. Y. C. Chan, L. R. White, and T. W. Healy, J. Phys. Chem. **98**, 9022 (1994).

[124] J. Hu and R. M. Westervelt, Phys. Rev. B **55**(2), 771 (1997).

[125] S. e.g.: P. Meakin and R. Jullien, Physica A **175**, 211 (1991).

[126] P. N. Pusey, in *Liquids, Freezing and the Glass Transition*, edited by J. P. Hansen, D. Levesque, and J. Zinn-Justin (North Holland, Amsterdam, 1991), vol. 51 of *Les Houches Lectures*, p. 763.

[127] P. Bolhuis, M. Hagen, and D. Frenkel, Phys. Rev. E **50**, 4880 (1994).

[128] C. N. Likos, Z. T. Németh, and H. Löwen, J. Phys. Condensed Matter **6**, 10965 (1994).

[129] A. R. Denton and H. Löwen, J. Phys. Condensed Matter **9**, L1 (1997).

[130] P. Bolhuis and D. Frenkel, J. Phys. Condensed Matter **9**, 381 (1997).

[131] A. Patrykiejew, S. Sokolowski, and K. Binder, J. Chem. Phys. **115**, 983 (2001).

[132] A. R. Denton and H. Löwen, Phys. Rev. Lett. **81**, 469 (1998).

[133] L. Levitov, Phys. Rev. Lett. **66**(2), 224 (1991).

[134] S. Neser, C. Bechinger, P. Leiderer, and T. Palberg, Phys. Rev. Lett. **79**, 2348 (1997).

[135] M. Schmidt and H. Löwen, Phys. Rev. Lett. **76**, 4552 (1996).

[136] M. Schmidt and H. Löwen, Phys. Rev. E **55**, 7228 (1997).

[137] M. Leppmeier, *Kugelpackungen: von Kepler bis heute* (Vieweg, Wiesbaden, 1997).

[138] H. Löwen, in *Spatial Statistics and Statistical Physics*, edited by K. Mecke and D. Stoyan (Springer, Berlin, 2000), vol. 554 of *Springer Lecture Notes in Physics*, p. 295.

[139] R. Peikert, El. Math. **49**, 17 (1994).

[140] H. Melissen, El. Math. **49**, 27 (1994).

[141] R. K. Bowles and R. J. Speedy, Physica A **262**(1-2), 76 (1999).

[142] H. Melissen, Am. Math. Monthly **100**, 916 (1993).

[143] H. Melissen, Acta Math. Hungar. **65**, 389 (1994).

[144] H. Melissen, Geometria Dedicata **50**, 15 (1994).

[145] B. D. Lubachevsky and R. L. Graham, Discrete. Comput. Geom. **18**, 179 (1997).

[146] Z. T. Németh and H. Löwen, J. Phys. Condensed Matter **10**, 6189 (1998).

[147] P. M. Chaikin and T. C. Lubensky, *Principles of Condensed Matter Physics* (Cambridge University Press, 2000).

[148] K. J. Falconer, *Fractal Geometry, Mathematical Foundations and Applications* (John Wiley and Sons Ltd., 1990).

[149] C. E. Reese, C. D. Guerrero, J. M. Weissman, K. Lee, and S. A. Asher, J. Coll. Interf. Sc. **232**, 76 (2000).

[150] P. Meakin and R. Jullien, Europhys. Lett. **15**, 667 (1991).

[151] P. Meakin and R. Jullien, Europhys. Lett. **15**, 851 (1991).

[152] B. D. Lubachevsky, F. H. Stillinger, and E. N. Pinton, J. Stat. Phys. **64**, 501 (1991).

[153] J. E. Socolar, Europhys. Lett. **18**, 39 (1992).

[154] J. Perrin, J. Phys. **9**, 5 (1910).

[155] T. Biben, J.-P. Hansen, and J.-L. Barrat, J. Chem. Phys. **98**, 7330 (1993).

[156] H. Löwen, Phys. Rep. **237**, 249 (1994).

[157] R. Piazza, T. Bellini, and V. Degiorgio, Phys. Rev. Lett. **71**, 4267 (1993).

[158] T. Biben, R. Ohnesorge, and H. Löwen, Europhys. Lett. **28**, 665 (1994).

[159] M. Heni and H. Löwen, Phys. Rev. Lett. **85**, 3668 (2000).

[160] A. van Blaaderen, R. Ruel, and P. Wiltzius, Nature **385**, 321 (1997).

[161] A. van Blaaderen, Colloid Polym. Sci. **104**, 59 (1997).

[162] A. van Blaaderen and P. Wiltzius, Adv. Mater. **9**, 833 (1997).

[163] P. G. de Gennes, J. Physique (Paris) **42**, L377 (1981).

[164] H. Löwen and T. Beier, Z. Physik B **79**, 441 (1990).

[165] P. Mills and P. Snabre, Europhys. Lett. **25**, 651 (1994).

[166] L. Bocquet and H. Löwen, Phys. Rev. E **49**, 1883 (1994).

[167] P. N. Segré, E. Herbolzheimer, and P. M. Chaikin, Phys. Rev. Lett. **79**, 2574 (1997).

[168] D. M. Mueth, J. C. Crocker, S. E. Esipov, and D. G. Grier, Phys. Rev. Lett. **77**, 578 (1996).

[169] B. J. Ackerson, S. E. Paulin, B. Johnson, W. van Megen, and S. Underwood, Phys. Rev. E **59**, 6903 (1999).

[170] D. C. Hong, Physica A **271**, 192 (1999).

[171] Y. Levin, Physica A **287**, 100 (2000).

[172] T. Biben and J.-P. Hansen, J. Phys.: Condens. Matter **6**, A345 (1994).

[173] H. Löwen, J. Phys.: Condens. Matter **10**, L479 (1998).

[174] J.-P. Simonin, J. Phys. Chem. **99**, 1577 (1995).

[175] C. N. Likos, Phys. Rep. **348**, 267 (2001).

[176] M. Watzlawek, C. N. Likos, and H. Löwen, Phys. Rev. Lett. **82**, 5289 (1999).

[177] A. Jusufi, J. Dzubiella, C. N. Likos, C. von Ferber, and H. Löwen, cond-mat/0012384 (2000).

[178] M. Watzlawek, H. Löwen, and C. N. Likos, J. Phys.: Condens. Matter **10**, 8189 (1998).

[179] A. Lang, C. N. Likos, M. Watzlawek, and H. Löwen, J. Phys.: Condens. Matter **24**, 5087 (2000).

[180] C. N. Likos, A. Lang, M. Watzlawek, and H. Löwen, Phys. Rev. E **63**, 0312XX (2001).

[181] A. A. Louis, P. G. Bolhuis, and J.-P. Hansen, Phys. Rev. E **62**, 7961 (2000).

[182] A. A. Louis, Philos. Trans. Royal Society (London) **A 359**, 939 (2001).

[183] R. L. Davidchak and B. B. Laird, Phys. Rev. Lett. **85**, 4751 (2000).

[184] F. T. Gittes and M. Schick, Phys. Rev. B **30**, 209 (1984).

[185] J. Chakrabarti, H. R. Krishnamurthy, A. K. Sood, and S. Sengupta, Phys. Rev. Lett. **75**, 2232 (1995).

[186] E. Frey, D. R. Nelson, and L. Radzihovsky, Phys. Rev. Lett. **83**, 2977 (1999).

[187] P. Bartlett and P. B. Warren, Phys. Rev. Lett. **82**, 1979 (1999).

[188] R. Leidl and H. Wagner, J. Chem. Phys. **98**, 4142 (1993).

[189] F. A. Rogers and D. A. Young, Phys. Rev. A **30**, 999 (1984).

[190] S.-C. Kim and S.-H. Suh, J. Chem. Phys. **104**, 7233 (1996).

[191] A. R. Denton and N. W. Ashcroft, Phys. Rev. A **44**, 8242 (1991).

[192] R. Ohnesorge, H. Löwen, and H. Wagner, Phys. Rev. E **50**, 4801 (1994).

[193] G. R. Newcome, C. N. Moorefield, and F. Vögtle, *Dendrimers and Dendrons* (Wiley VCH, Weinheim, 2001).

[194] See, e.g., the articles, in *Dendrimers III: Design, Dimension, Function*, edited by F. Vögtle (2001), vol. 213 of *Top. Curr. Chem.*

[195] M. Fischer and F. Vögtle, Angew. Chem. Intl. Ed. **38**, 884 (1999).

[196] S. M. Grayson and J. M. J. Frechet, Chem. Rev. **101**, 3819 (2001).

[197] F. Vögtle, S. Gestermann, R. Hesse, H. Schwierz, and B. Windisch, Progr. Polym. Sci. **25**, 987 (2000).

[198] C. N. Likos, Phys. Rep. **348**, 267 (2001).

[199] C. N. Likos, M. Schmidt, H. Löwen, M. Ballauff, D. Pötschke, and P. Lindner, Macromolecules **34**, 2914 (2001).

[200] C. N. Likos, S. Rosenfeldt, N. Dingenouts, M. Ballauff, P. Lindner, N. Werner, and F. Vögtle, J. Chem. Phys. **117**, 1869 (2002).

[201] P. Welch and M. Muthukumar, Macromolecules **31**, 5892 (1998).

[202] P. Welch and M. Muthukumar, Macromolecules **33**, 6159 (2000).

[203] I. Lee, B. D. Athey, A. W. Wetzel, W. Meixner, and J. J. R. Baker, Macromolecules **35**, 4510 (2002).

[204] S.-E. Stiriba, H. Frey, and R. Haag, Angew. Chem. Intl. Ed. **41**, 1329 (2002).

[205] P. G. de Gennes and H. Hervet, J. Phys. (Paris) **44**, L351 (1983).

[206] M. Ballauff, in *Dendrimers: Design, Dimension, Function*, edited by F. Vögtle (2002), vol. 212 of *Top. Curr. Chem.*

[207] M. Ballauff, in *Structure and Dynamics of Polymer and Colloidal Systems*, edited by R. Borsali and R. Pecora (Kluwer, 2002), vol. 568 of *NATO-ASI Series*, p. 157.

[208] S. Rosenfeldt, N. Dingenouts, M. Ballauff, N. Werner, F. Vögtle, and P. Lindner, Macromolecules (2002), in press.

[209] R. L. Lescanec and M. Muthukumar, Macromolecules **29**, 2280 (1990).

[210] M. L. Mansfield and L. L. Klushin, Macromolecules **26**, 4262 (1993).

[211] M. L. Mansfield, Polymer **35**, 1827 (1994).

[212] M. Murat and G. S. Grest, Macromolecules **29**, 1278 (1996).

[213] Z. Y. Chen and S.-M. Cui, Macromolecules **29**, 7943 (1996).

[214] L. Lue and J. M. Prausnitz, Macromolecules **30**, 6650 (1997).

[215] L. Lue, Macromolecules **33**, 2266 (2000).

[216] M. L. Mansfield, Macromolecules **33**, 8043 (2000).

[217] K. Karatasos, D. B. Adolf, and G. R. Davies, J. Chem. Phys. **115**, 5310 (2001).

[218] D. Boris and M. Rubinstein, Macromolecules **29**, 7251 (1996).

[219] S. Rosenfeldt, N. Dingenouts, M. Ballauff, P. Lindner, C. N. Likos, N. Werner, and P. Vögtle, Macrom. Chem. Phys. **203**, 1995 (2002).

[220] G. S. Grest, L. J. Fetters, J. S. Huang, and D. Richter, Adv. Chem. Phys. **XCIV**, 67 (1996).

[221] J.-P. Hansen and I. R. McDonald, *Theory of simple liquids* (Academic Press, London, 1991).

[222] J. S. Higgins and H. C. Benoît, *Polymers and Neutron Scattering* (Clarendon, Oxford, 1994).

[223] R. Klein and B. D'Aguanno, *Light Scattering: Principles and Development* (Clarendon, Oxford, 1996).

[224] O. Glatter and O. Kratky, *Small-Angle X-ray Scattering* (Academic, 1982).

[225] M. Doi and S. F. Edwards, *The Theory of Polymer Dynamics* (Clarendon, Oxford, 1986).

[226] J. S. Pedersen and M. C. Gerstenberg, Macromolecules **29**, 1363 (1996).

[227] G. S. Grest, K. Kremer, and T. A. Witten, Macromolecules **20**, 1376 (1987).

[228] I. O. Götze and C. N. Likos (2002), in preparation.

[229] L. Auvray and P.-G. de Gennes, Europhys. Lett. **2**, 647 (1986).

[230] M. Dijkstra, R. van Roij, and R. Evans, Phys. Rev. E **59**(5), 5744 (1999).

# Acknowledgement

Thanks to ...

... Hartmut Löwen and Christos N. Likos and the thpyII-team in Düsseldorf: Ansgar Esztermann, Joachim Dzubiella, Arben Jusufi, Cord Kielhorn, Matthias Schmidt, Alex Schlensog, Martin Heni, Ralf Pierre, Ronald Blaak, Ingo Götze, Christian von Ferber and Godehard Sutmann and Alexei A. Kornyshev and S. Leikin and A. Parsegian and A. Cherstvy and Studienstiftung des deutschen Volkes and famille&amis and M. S. and M. S.♡.